Multistate Metadynamics with Electronic Collective Variables

Dissertation
zur Erlangung des naturwissenschaftlichen Doktorgrades
an der Fakultät für Chemie und Pharmazie der
Julius-Maximilians-Universität Würzburg

vorgelegt von
Joachim Oliver Lindner
aus Ochsenfurt.

Würzburg, 2019

Eingereicht bei der Fakultät für Chemie und Pharmazie am

08.08.2019

Gutachter der schriftlichen Arbeit

1. Gutachter: Prof. Dr. Roland Mitrić
2. Gutachter: Prof. Dr. Ingo Fischer

Prüfer des öffentlichen Promotionskolloquiums

1. Prüfer:	Prof. Dr. Roland Mitrić
2. Prüfer:	Prof. Dr. Ingo Fischer
3. Prüfer:	Prof. Dr. Volker Engel
4. Prüfer:	Prof. Dr. Matthias Lehmann
5. Prüfer:	Prof. Dr. Holger Braunschweig

Datum des öffentlichen Promotionskolloquiums

18.10.2019

Doktorurkunde ausgehändigt am

_____

Contents

1. Introduction

1.1. From the Born-Oppenheimer Approximation to Complex Molecular Simulations

The interpretation of chemical reactions as rearrangements of atomic nuclei in molecules seems completely self-evident in the modern understanding of chemistry. However, the fact that electronic motion does not have to be considered in this picture relies on the concept of a potential energy surface (PES) that defines the energy $U(\mathbf{R})$ as a function of nuclear coordinates $\mathbf{R}$.

Back in the 1920s, the question how optical molecular spectra can be explained employing the rules of quantum mechanics was one of the leading questions in the field of physics. At that time, much progress had already been made in the interpretation of atomic spectra and the Schrödinger equation of the hydrogen atom had been solved exactly,[1] but for molecules larger than H_2^+ the direct analytic solution had proven impossible, thus requiring the introduction of approximations. The idea of separating electronic motion from nuclear vibrations and rotations came up due to the experimentally observed different orders of magnitude of line splittings in optical spectra and the well-known differences between electron mass m and the average nuclear mass M.[2,3] This motivated Born and Oppenheimer[4] to introduce an approximation based on the perturbational expansion of the total energy in powers of $\sqrt[4]{m/M}$. In the obtained series, individual expressions appear for electronic, vibrational and rotational energy, while the coupling between them is found only in higher terms and therefore can be neglected in many cases.

In this regard, the full non-relativistic molecular Hamiltonian can be split into the kinetic energy of the nuclei $\hat{T}_n$ and a second part $\hat{H}_{el}$ containing electronic kinetic energy and the Coulomb interactions between all charged particles, leading to the famous separation of the full molecular Schrödinger equation into an electronic equation

$$\hat{H}_{el}(\mathbf{r};\mathbf{R})\psi_i(\mathbf{r};\mathbf{R}) = U_i(\mathbf{R})\psi_i(\mathbf{r};\mathbf{R}), \tag{1.1}$$

with the electronic wavefunction ψ_i and electron coordinates $\mathbf{r}$, and the respective nuclear counterpart

$$\left[\hat{T}_n(\mathbf{R}) + U_i(\mathbf{R})\right]\chi_i(\mathbf{R}) = E\chi_i(\mathbf{R}) \tag{1.2}$$

with nuclear wavefunctions χ_i.

At this point, it should be noted that the semicolon in Eq. 1.1 means that the electronic Hamiltonian $\hat{H}_{el}$ contains nuclear coordinates $\mathbf{R}$, but not derivatives with respect to $\mathbf{R}$. Thus, $\mathbf{R}$ appears in the electronic wavefunctions only as a parameter. As a consequence, solving the electronic Schrödinger equation for all different nuclear positions yields a so-called adiabatic PES $U_i(\mathbf{R})$ in the electronic state i. The latter in turn serves as an external potential for the nuclear motion according to Eq. 1.2 in which the electronic coordinates do not appear explicitly. Due to the hermiticity of $\hat{H}_{el}$, the set of all electronic wavefunctions $\{\psi_i\}$ forms a complete basis in the system's Hilbert space and allows expanding the total wavefunction into a series with the nuclear wavefunctions χ_i as expansion coefficients.

The actual approximation in this approach consists in neglecting the first and second derivative couplings

$$\mathbf{d}_{ij}(\mathbf{R}) = -\sum_{\mu}^{nuclei} M_{\mu}^{-1} \langle \psi_i(\mathbf{r};\mathbf{R})| \nabla_{R_\mu} |\psi_j(\mathbf{r};\mathbf{R})\rangle \,, \tag{1.3}$$

$$D_{ij}(\mathbf{R}) = -\sum_{\mu}^{nuclei} M_{\mu}^{-1} \langle \psi_i(\mathbf{r};\mathbf{R})| \nabla^2_{R_\mu} |\psi_j(\mathbf{r};\mathbf{R})\rangle \,, \tag{1.4}$$

that arise by the nuclear kinetic energy operator acting on the electronic wavefunctions. These so-called nonadiabatic or vibronic couplings represent the change in the electronic structure upon small changes in the nuclear positions and are usually very small in the electronic ground state. Therefore, in many cases the electronic structure can be described well by considering a single electronic state i and the respective PES minimum can be interpreted as the equilibrium geometry of the nuclei.

The groundbreaking work of Born and Oppenheimer therefore enabled the development of quantum mechanical electronic structure methods without having to deal with nuclear motion at the same time. Only shortly after the publication of their approach,[4] Hartree and Fock came up with the first successful attempt to solve the electronic Schrödinger equation for many-electron systems.[5,6] The transformation of the total electronic Schrödinger equation into a set of effective one-electron Hartree-Fock (HF) equations allows for an iterative solution. The one-electron wavefunctions are referred to as molecular orbitals. In order to fulfill the Pauli principle, an antisymmetrized ansatz of spin orbitals is used for the electronic wavefunction ψ_i in the form of single Slater determinants. However, this is at the cost of neglecting that the electronic motion is actually correlated which requires the consideration of multiple determinants. For this purpose, decades of research have been dedicated to the development of post-HF quantum-chemical methods that meet the right balance between accuracy and computational expense. In particular, configuration interaction,[7] Møller-Plesset perturbation theory[8] and coupled

cluster[9] methods have been applied in many variants, but the problem of all of these methods is the high computional demand, especially in combination with typically needed large basis sets. Density functional theory (DFT) in principle reduces the complexity in a closed-shell system from a $4N$-dimensional problem to a function of 3 variables (N is the number of electrons) by using the unique mapping between electron density and energy, which has been proven to exist.[10] However, as the form of the functional connecting the density with the energy is not known, huge effort has been spent on the development of approximate functionals. In its most popular formulation,[11] DFT uses a similar self-consistent field procedure as HF, but includes some electron correlation effects at the cost of making systematical improvements difficult.

Since electronic transitions in molecules are usually in the order of several electronvolts which is much higher than the thermal energy $k_B T$ at room temperature ($\approx 26\,\mathrm{meV}$), in such cases the electronic ground state is the only thermally populated one. Thus, if $U_0(\mathbf{R})$ is known, structure and reactivity can be calulated to a large extent, while the exact form of the electronic wavefunction is not needed. As an example, the energetics of many chemical reactions can be determined by identifying minima and transition states on $U_0(\mathbf{R})$. Beyond the search for stationary points, thermodynamic sampling of structures is performed in many variants of Monte Carlo (MC) statistics or by simulation of the time evolution of the system with molecular dynamics (MD),[12] where the nuclear motion is treated using classical trajectories while the whole plethora of electronic structure methods is available for the accurate determination of the PES.

Almost half a century passed from the early attempts to simulate the reaction dynamics in small gas phase molecules[13] to the first MD simulation of the conformational flexibility in a complete folded protein,[14] but from then on, the progress advanced rapidly. The development of on-the-fly techniques alongside with high-quality integrators for Newton's equation of motion[15] and increasing computer power facilitated the MD simulation of large systems without the need to precalculate the PES. This was even accelerated by further progress in electronic structure theory which now allows treating the reactive core of a large system with quantum mechanics, while the surroundings are modeled with classical molecular mechanics (QM/MM).[16–18]

Especially for periodic systems, the ab initio MD by Car and Parrinello[19] constitutes a landmark in the efficient and accurate simulation by combining dynamics and DFT. Although this approach goes beyond the BO approximation, the underlying concepts would not have been developed without the successes of highly specialized research in electronic structure theory and nuclear dynamics. Even with excited state dynamics which was growing more and more important from the beginning of the 1990s, the idea of BO approximation was widely preserved and nonadiabatic effects were included by relatively small modifications to the PESs, for ex-

ample employing Tully's surface hopping method[20] which allows classical trajectories to be propagated on different BO PESs according to quantum mechanically determined probabilities.

It was also Tully who stated almost twenty years ago that *"Theoretical chemists of the future will need to be expert in both electronic structure and statistical mechanics/dynamics"*,[21] which is largely reflected in this thesis. In this respect, the automatic sampling of functional landscapes for the understanding of photophysical processes and the development of promising materials is presented. Especially, the description of nuclear configurations where the nonadiabatic coupling between electronic states is strong requires elaborate methods that take into account the breakdown of the BO approximation. Based on the examples of PES crossings and biradicalicity in molecular systems, the concepts in this thesis make use of properties that arise from a challenging electronic structure and combine them with advanced MD techniques.

1.2. Molecular Dynamics

1.2.1. Verlet Integration

The time evolution of a quantum mechanical system is manifested in the time-dependent Schrödinger equation, and as shown in section 1.1, nuclear and electronic motion can be separated and appear on different time scales. Nuclear motion takes place on the femtosecond time scale and according to the BO approximation can be described reasonably well by employing classical mechanics as long as quantum effects such as tunneling are negligible. Therefore, trajectories in the phase space of atomic nuclei can be obtained applying Newton's second law

$$\mathbf{F} = M\ddot{\mathbf{R}}, \tag{1.5}$$

where the forces $\mathbf{F}$ acting on the nuclei can be determined from the negative gradient of the PES at the current position $\mathbf{R}$

$$\mathbf{F} = -\nabla \left(U(\mathbf{R}) \right). \tag{1.6}$$

Numerical integration of the equations of motion is required in order to obtain coordinates and velocities at a certain time in the future. In the Verlet algorithm,[15] a Taylor expansion around the current time step t up to the third order is employed to express the positions after a certain time step Δt as

$$\mathbf{R}(t+\Delta t) = \mathbf{R}(t) + \dot{\mathbf{R}}(t)\Delta t + \frac{\ddot{\mathbf{R}}(t)}{2}\Delta t^2 + \frac{\dddot{\mathbf{R}}(t)}{6}\Delta t^3 + \mathcal{O}(\Delta t^4), \tag{1.7}$$

and analogously for negative time steps $-\Delta t$ as

$$\mathbf{R}(t-\Delta t) = \mathbf{R}(t) - \dot{\mathbf{R}}(t)\Delta t + \frac{\ddot{\mathbf{R}}(t)}{2}\Delta t^2 - \frac{\dddot{\mathbf{R}}(t)}{6}\Delta t^3 + \mathcal{O}(\Delta t^4). \tag{1.8}$$

The sum of Eqs. 1.7 and 1.8 and substitution of $\ddot{\mathbf{R}}$ using Eqs. 1.5 and 1.6 yields the new coordinates up to an accuracy of the order Δt^3 as

$$\mathbf{R}(t+\Delta t) \approx 2\mathbf{R}(t) - \mathbf{R}(t-\Delta t) - \frac{\nabla\left(U(\mathbf{R})\right)}{m}\Delta t^2, \tag{1.9}$$

where the neglect of the higher terms is a good approximation if Δt is small relative to the time scale of nuclear motion. The problem of this algorithm is that velocities are not directly obtained for the current time step but might be needed for the calculation of the instantaneous kinetic energy.

In the velocity Verlet variant,[22] coordinates and velocities in the next time step $t + \Delta t$ are directly evaluated on the basis of their values in the current step:

$$\mathbf{R}(t+\Delta t) \approx \mathbf{R}(t) + \mathbf{v}(t)\Delta t + \frac{1}{2}\ddot{\mathbf{R}}(t)\Delta t^2, \tag{1.10}$$

$$\mathbf{v}(t+\Delta t) = \mathbf{v}(t) + \frac{\ddot{\mathbf{R}}(t) + \ddot{\mathbf{R}}(t+\Delta t)}{2}\Delta t^2, \tag{1.11}$$

where $\ddot{\mathbf{R}}$ are again obtained from the gradient of $U(\mathbf{R})$ in the respective time step according to Eqs. 1.5 and 1.6. The error in this approach is of the same order of magnitude as in the original formulation of Verlet. Thus, for time steps up to about $1\,\mathrm{fs}$, the sum of classically evaluated nuclear kinetic energy and electronic potential energy is conserved. The dynamics performed under these conditions corresponds to the microcanonical NVE ensemble, i.e. with constant number of particles, volume and energy.

If coupled to a thermostat, the energy of an individual trajectory is no longer conserved while the system temperature is kept in a certain distribution around a predefined value. Technically, this can be done by rescaling the velocities at every time step according to the current kinetic energy and a coupling constant which controls the speed of kinetic energy transfer to the surrounding heat bath.[23] However, a real constant-temperature (NVT) ensemble, also referred to as canonical ensemble, is only achieved by the introduction of a stochastic component into the thermostat.[24] For long simulation times, the sampling is ergodic, i.e. the time average equals the ensemble average of a thermodynamic equilibrium at the given temperature and the histogram N of some nuclear variable s refers to the free energy

$$F(s) = -k_B T \lim_{t\to\infty} \ln\left(N(s,t)\right). \tag{1.12}$$

1.2.2. Metadynamics

Since real-time MD simulations require the calculation of energy and gradients at every time step, only simulations of processes on femtosecond to picosecond time scales are feasible with the current computer power, if the electronic potential is determined quantum mechanically. Rare events, i.e. processes exceeding high barriers between the starting and the end structures cannot be sampled even if they occur in real physical systems with significant probability. For example, chemical reactions often take place in the millisecond to second range.

In order to address this problem, several accelerated MD techniques have been developed based on a bias potential V_{bias} which modifies the surface on which the dynamics is performed:

$$\mathbf{F}' = -\nabla \left(U + V_{bias} \right). \tag{1.13}$$

The easiest approach to obtain an artificial force that drives the desired process is steered MD, in which V_{bias} is a static function of the nuclear coordinates. In that way, also slow processes can be observed, but the resulting trajectory does not have a physical meaning. However, it can be used as an initial pathway for further optimization.[25] Based on the idea that the reaction coordinate of the desired process can be expressed with respect to a small number of well-defined slow variables, so-called collective variable (CV) methods enjoy great popularity.[26–30] Umbrella sampling[31] relies on CVs in order to allow the estimation of free energies of the investigated process. Depending only on a small number of parameters, umbrella sampling always yields a converging value of the free energy difference between the states of interest but has the problem of not being rigorously reliable. A particularly attractive approach that represents a robust yet easy to use method is metadynamics, introduced by Laio and Parrinello in 2002.[32] It relies on a repulsive potential V_G built up by the addition of small portions of bias in the form of Gaussian functions in regular time steps:

$$V_G = w \sum_{t'=\tau_G, 2\tau_G, \ldots} \exp\left(-\frac{(s(t) - s(t'))^2}{2\delta s^2} \right). \tag{1.14}$$

For long propagation times, the shape of the free energy surface (FES) is recovered from the negative of V_G (see Fig. 1.1). In its original formulation, metadynamics already enabled the efficient sampling of slow processes but convergence of the free energy was not assured. Therefore, a lot of extensions and improvements to the method have been developed in the following years. Most importantly, the formulation of well-tempered metadynamics marked a breakthrough in 2008, being the first in the family of these methods that has been shown to yield a properly converging free energy surface.[33] This major improvement is achieved by scaling the

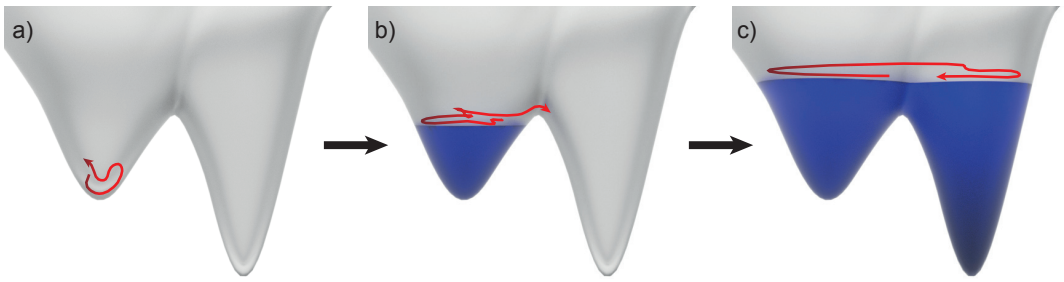

Figure 1.1.: Schematic representation of the metadynamics method with example trajectories (red). a) At the beginning of the simulation, the dynamics is performed in the pure electronic potential (gray). b) As the simulation time proceeds, the current minimum is filled with a bias potential V_G (blue), enabling the transition into neighboring minima. c) After long simulation times, V_G completely compensates the shape of the FES.

height $w(t)$ of the added Gaussians according to the value of the bias potential at the current position in CV space:

$$w(t) = w_0 \exp\left(-\frac{V(s,t)}{k_B \Delta T}\right), \tag{1.15}$$

with the initial height w_0 and Boltzmann constant k_B. A bias factor

$$\gamma = \frac{T + \Delta T}{T} \tag{1.16}$$

is applied to control the accessible range on the FES, where T is the actual temperature of the simulation and ΔT is related to the maximum kinetic energy that is available to explore the FES which is finally obtained as

$$F(s) = -\frac{T + \Delta T}{\Delta T} V_G(s, t \to \infty). \tag{1.17}$$

A bias factor of $\gamma = 1$ ($\Delta T = 0$) means that an unbiased simulation is performed, while the original metadynamics is recovered in the limit of large γ ($\Delta T \to \infty$). A rough estimation of the barrier height prior to the simulation helps to find the ideal ΔT value for most efficient sampling. Transition-tempered metadynamics is an approach to overcome this problem by barrier estimation on-the-fly, but requires that starting and end structures of the slow process are already roughly known prior to the simulation.[34] Flexibility in the Gaussian width δs has also been introduced in the metadynamics with adaptive Gaussians[35] in order to better react on potential energy surfaces on which several minima with different widths are to be explored.

Although metadynamics has been shown to be relatively stable to the choice of the CVs, these are the most critical parameters and hence have been addressed in many studies during the recent years.[36] For the evaluation of the dynamics forces defined in Eq. 1.13 it is necessary to calculate the gradient of the bias potential which requires the derivation of the CV with respect to the nuclear coordinates according to the chain rule

$$\nabla V_G = \frac{\partial V_G}{\partial s}\frac{\partial s}{\partial \mathbf{R}}. \tag{1.18}$$

While simple processes can easily be described by a single geometrical variable like bond lengths, bond angles, dihedral angles or coordination numbers, the appropriate choice of CVs can be quite challenging for more complex systems and pathways involving multiple steps. Usually, the number of CVs is restricted to 2-3, since the computational effort increases exponentially with the number of variables. Apart from that, a non-optimal choice of CVs can lead to hysteresis and convergence failure.

1.2.3. Nonadiabatic Dynamics

The irradiation of molecules by light leads to the population of excited states, which is the initializing step of numerous kinds of processes in nature, e.g. vision or light harvesting for photosynthesis. However, the coupling of electronically excited states prohibits the description of these processes with a single PES. A fast vertical excitation according to the Franck-Condon principle[37–39] leads to a configuration out of the equilibrium of the respective excited state, accompanied by an increased vibrational energy. This induces several dynamical relaxation processes on different time scales that can reach down to the femtosecond regime. Usually, excited state energies are close to each other compared to the energy gap with respect to the ground state, so relaxation into the S_1 state is fast and fluorescence occurs mainly from this state, according to Kasha's rule.[40] In the studies of light-matter interactions, possible deactivation pathways upon photoexcitation are of great interest. In the context of the BO approximation, this means that the total electronic state needs to be expanded into a set of eigenstates

$$|\Psi_{el}\rangle = \sum_j c_j(t)\,|\psi_i\rangle \tag{1.19}$$

with complex-valued amplitudes $c_j(t)$ and nonadiabatic couplings $\mathbf{d}_{ij}$ need to be considered in the time-dependent Schrödinger equation,

$$i\hbar\frac{\partial}{\partial t}c_i(t) = U_i(\mathbf{R})c_i(t) - \sum_j c_j(t)\left[i\hbar\dot{\mathbf{R}}\cdot\mathbf{d}_{ij}\right]. \tag{1.20}$$

Two main approaches are common for nonadiabatic dynamics simulations allowing for the contribution of multiple PESs rather than single adiabatic states. In the mean-field (Ehrenfest) dynamics, the trajectory is propagated on an effective PES obtained as a linear combination of pure adiabatic states, according to the respective quantum mechanical populations $\rho_{ii} = c_i^* c_i$.[41,42]

Tully's surface hopping[20] extends the MD to multiple electronic states using a statistical ansatz. In this quantum-classical approach, the dynamics is started in a certain BO electronic state $|\psi_i\rangle$ and in every time step hopping probabilities to all other considered states are calculated according to[43,44]

$$P_{i\to j} = \Theta(-\dot{\rho}_{ii})\Theta(\dot{\rho}_{jj})\frac{-\dot{\rho}_{ii}\Delta t}{\rho_{ii}}\frac{\dot{\rho}_{jj}}{\sum_k \Theta(\dot{\rho}_{kk})\dot{\rho}_{kk}}, \tag{1.21}$$

where the quantum mechanical populations of the electronic state i are given by the absolute squares of the respective expansion coefficients. The Heaviside Θ-functions in the first part of Eq. 1.21 ensure that a hop can only occur from a state with decreasing population into a state with increasing population. The second term represents the probability to leave state i and the last term is the probability that j is the target state in case of a successful hop. During the hopping procedure, the energy is conserved such that kinetic energy is rescaled according to the energy gap between the two involved states. For an ensemble of multiple trajectories, the total state populations over time resemble the quantum mechanical nuclear wavepacket and can be used to determine lifetimes of excited states.

While this approach requires the initial electronic state to be set manually based on previously calculated electronic spectra or chemical intuition, the interaction with an external electric field is incorporated in the field-induced surface hopping (FISH) method.[45] In this case, the time evolution of the expansion coefficients

$$i\hbar\frac{\partial}{\partial t}c_i(t) = U_i(\mathbf{R})c_i(t) - \sum_j c_j(t)\left[i\hbar\dot{\mathbf{R}}\cdot\mathbf{d}_{ij} + \boldsymbol{\mu}_{ij}\cdot\mathbf{E}(t)\right], \tag{1.22}$$

does not only contain nonadiabatic couplings (first term in brackets with nonadiabatic coupling vector $\mathbf{d}_{ij}$) but also the interaction with an external field $\mathbf{E}(t)$ depending on the transition dipole moment $\boldsymbol{\mu}_{ij}$. This leads to a modification of the hopping probabilites that allows to simulate electronic excitations from the ground state upon interaction with a realistic laser pulse. Extensions to the method range from complex shaped pulse trains[46] to nonlinear excitation processes[47] or fields of circularly polarized light.[48]

1.3. Conical Intersections

1.3.1. Breakdown of the BO-Approximation

The nonadiabatic effects discussed in the previous section originate from the breakdown of the BO approximation, i.e. the nonadiabatic coupling matrix elements between electronic states cannot be neglected. The most remarkable failure of the BO approximation is observed in the vicinity of conical intersections (CIs)[49–51] which represent surface crossings between adiabatic electronic states. First proposed already in 1929,[52] CIs have long been objects of curiosity, mainly due to the fact that their properties are hard to prove experimentally. While in the 1970s the concept of avoided crossings still dominated over CIs and the phenomenon of the latter was seen as "a relatively uncommon occurrence",[53] the development of further theories[54,55] supported the acceptance of real surface touchings. Finally, the start of systematic investigations on the role of CIs in small[56,57] and also larger molecules[58,59] revealed that CIs are ubiquitous in real molecular systems.

The most intuitive reason for the appearence of CIs is symmetry, as is the case with Jahn-Teller intersections.[60] If a molecule is distorted from its equilibrium structure such that it can be classified by a higher symmetry point group and the electronic ground state transforms like a degenerate irreducible representation, a crossing with the first excited state is required to give rise to a degenerate electronic state. Apart from that, accidental intersections between states of different or the same symmetry are possible and much more important than initially thought.[61]

In the case of two-state intersections, the degeneracy is lifted in exactly two dimensions which are given by the energy gradient difference vector $\mathbf{g}$ and the nonadiabatic coupling vector $\mathbf{h}$, leading to the typical shape of a double cone. The subspace of the PES that maintains the degeneracy contains all other dimensions perpendicular to $\mathbf{g}$ and $\mathbf{h}$ and is referred to as CI seam. Although the crossing region itself has no volume, the region close to a CI is still characterized by large nonadiabatic coupling and therefore, nonradiative electronic transitions between the two participating states are very likely. In the intersection point itself, the nonadabatic coupling is infinite. Besides the energetic degeneracy, the most notable effect of CIs is the geometric phase (or Berry phase) effect.[62–64] After a complete circular path around a CI, one would expect that the wavefunction is the same as in the beginning, but instead, it has been modified by an additional phase factor.

The two branching space vectors are useful to characterize the CI and with that its potential influence on photochemical reactions. In this regard, the pitch, i.e. steepness of the two cones, as well as asymmetry and tilt are parameters of interest. Two CI models with different topographies and exemplary wavepacket propagations are depicted in Fig. 1.2. While a perfect double cone shape like in Fig. 1.2a promotes the efficient transfer of a wavepacket to the lower electronic state, the latter is likely to

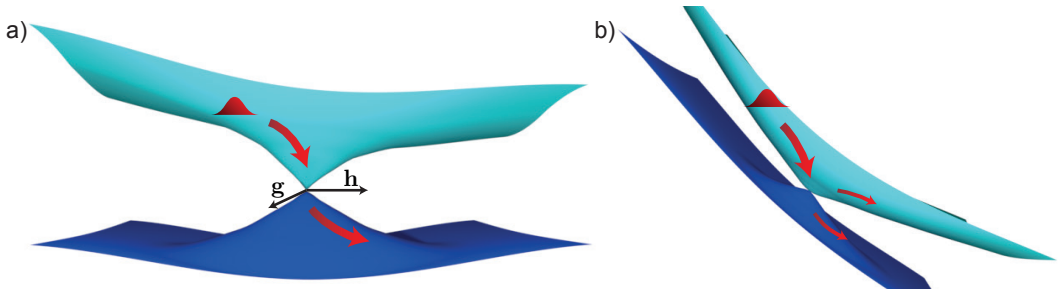

Figure 1.2.: Visualization of the electronic states energies in the branching space of a S_0(dark blue) - S_1(cyan) conical intersection. Example wavepackets and their population transfer at the CI are shown for a) an untilted and b) a tilted CI.

split when approaching a CI with tilted topography like the one in Fig. 1.2b, while a significant part remains in the higher electronic state. Furthermore, the directions in the **g**-**h** space represent atomic displacements that are likely to occur right after a change from the upper to the lower state, because of the attempt of every system to minimize its internal energy. In this regard, CIs can be considered as transition states of photochemical reactions[65] and therefore affect their outcome in a significant manner.

1.3.2. Role of CIs in Photophysics and Photochemistry

Many different radiative and non-radiative deactivation processes are known to happen upon photoexcitation into a higher electronic state. The time scales of these processes are very different, ranging from the femtosecond scale to several seconds. Fluorescence is the most common process of radiative decay, but phosphorescence and stimulated emission also play significant roles in some systems. In competition to that, radiationless transitions need to be considered. If the populated electronic state is well-separated from the others, the most important process upon excitation is usually vibrational relaxation, i.e. nuclear kinetic energy is transferred from internal degrees of freedom to the surrounding environment until the vibrational ground state on the current electronic PES is reached. When other electronic states are accessible, electronic transitions between states of the same (internal conversion, IC) or different spin state (intersystem crossing, ISC) can occur. Among these, ISC is a forbidden process and therefore very slow, except if heavy atoms are involved and spin-orbit coupling is of relevance. IC, on the other hand, is even faster than vibrational relaxation, because the nonadiabatic coupling between two electronic states of the same spin multiplicity leads to the efficient transition into the energetically lower state. Especially if a CI lies within the accessible range on the excited

PES, ultrafast deactivation on the femtosecond scale is likely to occur.

If the decay is slow, the excited state has a long lifetime which can lead to irreversible damage of the molecule if dissociation channels are accessible from the Franck-Condon region. This is likely for excitations in the ultraviolet (UV) electromagnetic range and therefore has to be avoided in biological systems by fast and efficient deexcitation. The ultrafast deactivation of DNA and RNA nucleobases is one of the most relevant examples where the presence of CIs prevents photo-induced damage[66] in contrast to similar molecules without accessible CIs.[67]

Apart from that, the photoisomerization of the rhodopsin cofactor retinal from its 11-*cis* to the all-*trans* form which is long known to be the initial step in the vision process[68] has been the subject of many investigations because of an incredibly large quantum yield and fast reaction kinetics. Computational models proposed that a CI between the lowest two electronic states is involved in the process[69–71] and with the help of femtosecond-resolved optical spectroscopy, the closing and subsequent reopening of the energy gap could even be observed experimentally.[72]

In general, the presence of a CI can be both helpful or unfavorable, depending on the respective system and application, which is particularly reflected in materials engineering. Fluorescence quenching due to the presence of CIs is often an unwanted process, because it decreases the quantum yield. This is important for example in the development of highly efficient organic light emitting diodes (OLEDs). But, on the other hand, CI-mediated singlet fission[73] is a promising concept to create more usable charge carriers in photovoltaic devices. Furthermore, excimer formation in organic dyes, i.e. the stabilization of weakly bound complexes in the electronic excited state, has been discussed to reduce the ability for exciton diffusion in electronic devices.[74] In a model system of pyrene dimers, it has been shown that intermolecular CIs are involved in the mechanism of excimer formation due to the interplay between short-range and long-range coupling of two monomeric subunits.[75]

1.3.3. Localization of Conical Intersections

Although a lot of experimental effort has been put into the observation of CIs and their effects, for example based on femtosecond pump-probe spectroscopy,[76] attosecond stimulated X-ray Raman signals[77] or time-resolved photoelectron spectroscopy,[78] the majority of studies has been performed based on theoretical approaches.

For the understanding of photophysical and photochemical processes, it is crucial to gain knowledge on the structures at which CIs between electronic states can occur. Of particular interest are minimum energy crossing points (MECPs), i.e. local minima on the CI seam, because they are usually easier to access than higher lying intersection points. Therefore, a couple of methods have been introduced for

the characterization and local optimization of MECPs. A lot of progress was made during the early 1990s by the development of a Lagrange-Newton algorithm[79] and shortly afterwards a gradient-projection method.[80] Both of them are now widely used for the efficient optimization of MECPs and have been shown to be similarly efficient in many examples.[81] Apart from that, a generally applicable but more slowly converging method based on a penalty function has been introduced[82] almost ten years later, which stands out because it does not require calculation of the nonadiabatic coupling vector.

Only recently, much progress has been reported in the field of the automated localization of CIs in the groups of Maeda and Morokuma. Firstly, the automatic downward distortion following (ADDF) method combined with a penalty function detects the direction with the strongest anharmonic behavior to localize accessible MECPs close to an initial guess.[83,84] The downside of the vibrational analysis needed for this is that it repeatedly requires the calculation of the Hessian, which is hard to realize for large systems. Apart from that, the conventional artificial force-induced reaction (AFIR) method allows the study of CIs in photoaddition reactions by introducing a force that drives two fragments close to each other.[85] Later, the generalization of AFIR for single-component reactions and combination with the gradient projection algorithm allowed the automated CI search much more efficiently than based on ADDF.[86,87] These methods have performed well in finding literature-known MECPs, but are limited in their ability to obtain a complete, systematical view on the CI seam.

1.4. Molecular Biradicals

1.4.1. Definition, Appearance and Applications

In the model of two electrons in two localized orbitals, the lowest two singlet state energies can be easily described by configuration interaction. As a consequence of Brillouin's theorem, the matrix elements between the HF ground state and singly excited determinants vanish and the doubly excited configuration is the only one mixing with the ground state. For two well-separated electronic states, this means that the use of a single determinant for each of them is a good approximation, but in case of degenerate electronic states, linear combinations of the two determinants are required which corresponds to the picture that the two electrons are equally distributed over both orbitals. Although this model is only an approximation for large molecular systems, many CIs between the S_0 and S_1 states have biradical character.[54] Therefore, biradical conformations are transiently populated in photoinduced processes and reactions involving dynamics through a CI such as cycloadditions. Tuning the steric and electronic properties of these species via the introduction of

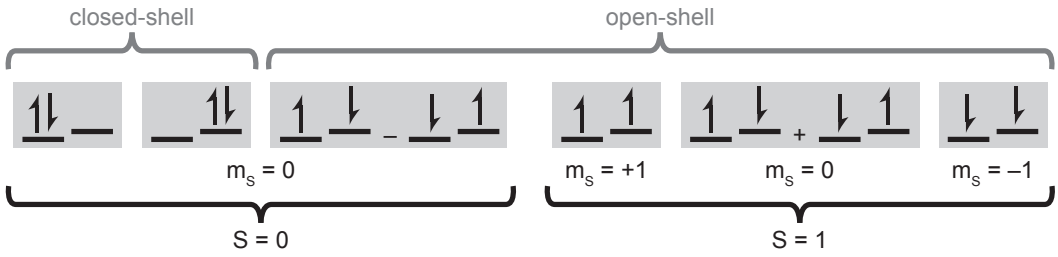

Figure 1.3.: Possible spin states in a two-electron two-orbital model. Two closed-shell singlets are possible aside from an open-shell singlet ($S = 0$) and three triplet ($S = 1$) states.

suitable substituents enables the synthesis of stable biradicals. These molecules exhibit interesting characteristics and are therefore further described in this section.

A molecule with an even number of electrons and an electronic ground state that is well separated from the other states usually is of closed-shell singlet character. If the lowest unoccupied molecular orbital (LUMO) is close to the highest occupied molecular orbital (HOMO), however, several possible spin state configurations arise for the two electrons with highest energy (see Fig. 1.3). Besides the closed-shell singlet states, an open-shell singlet as well as three different triplet configurations are potentially important. When one of these is lower in energy than the closed-shell singlet, there are two unpaired electrons, leading to a paramagnetic species termed biradical. According to a stricter definition, "biradical" is only used for molecules with non-interacting, localized electrons (i.e. observed as two separate doublets under the influence of a magnetic field), while "diradical" denotes the larger class of two interacting unpaired electrons in singlet or triplet state,[88] but for the sake of simplicity, the term "biradical" is used throughout this thesis. One of the model biradical molecules is dioxygen. Due to its symmetric linear shape it has two degenerate π orbitals that are populated by only two electrons. The attractive exchange interaction between electrons with the same spin is larger than the repulsive spin pairing energy and stabilizes the triplet compared to the singlet state.

In case of a closed-shell ground state and nearly degenerate frontier orbitals, the biradical properties can mix into the ground state wavefunction and therefore play a significant role in the chemistry of the molecule. Such systems are termed biradicaloids because of their partly open-shell character. The *p*-xylylene molecule is an example for which the ground state has been shown to be closed-shell singlet,[89] but the biradical character is partly expressed and therefore typical biradical properties are observed like the tendency to polymerize in solution.

Similar to monoradicals, biradicals are usually very reactive and therefore occur as intermediate species in high temperature processes like soot formation dur-

ing combustion. The combustion of benzene, for example, leads to the formation of *o*-benzyne as an intermediate to smaller hydrocarbon fragments.[90] Similarly, sunlight-driven radical chemistry in the earth atmosphere can be compared to a low temperature flame.[91] On the other hand, biradicals are likely to be present in cold, low-density media like interstellar space, since the lifetimes in this environment are generally higher owing to limited collision rates.

For materials science, biradicals and biradicaloids represent promising candidates for the development of new optoelectronic devices. One of the big challenges of efficient OLED design is that excitations are either created in singlet or triplet state, with the latter being three times more probable. The electronic ground state is usually singlet, so the desired fluorescence process is only dipole-allowed in 25% of the excitations. To overcome this problem, much effort has been spent on the development of fast triplet (phosphorescence) and thermally activated delayed fluorescence (TADF) emitters.[92] Especially the latter are promising because of their ability for thermally initiated reverse ISC from the triplet state to an excited singlet state which in turn enables spin-allowed emission. Only recently, a class of radical and biradical emitters gained more attention, e.g. a radical doublet emitter was presented with promising properties[93] and stable isoindigo biradicaloids were synthesized with a remarkably low singlet-triplet gap of only $0.065\,\mathrm{eV}$ and potential application in future OLED designs.[94] The radiative deexcitation from higher singlet or triplet into one of the almost degenerate states should therefore be equally possible.

1.4.2. Theoretical Description

Different measures have been developed for the determination of the biradical character y justified by experimental or theoretical results, where $y = 0$ means no biradicaloid character and $y = 1$ describes a perfect biradical. If experimental values of the lowest two excitation energies $\Delta E_{S_1,S_0}$, $\Delta E_{S_2,S_0}$ and the singlet triplet gap $\Delta E_{T_0,S_0}$ are available, the biradical character can be quantified[95] as

$$y = 1 - \sqrt{1 - \left(\frac{\Delta E_{S_1,S_0} - \Delta E_{T_0,S_0}}{\Delta E_{S_2,S_0}} \right)^2}. \tag{1.23}$$

For a large singlet-triplet gap close to $\Delta E_{S_1,S_0}$, the second term under the root vanishes, resulting in $y = 0$. For a small singlet-triplet gap and similar state energies of the S_1 and S_2 states, on the other hand, Eq. 1.23 yields a value close to one. However, some of the excitation energies might be difficult to obtain due to dipole-forbidden transitions and in this case two-photon excitations are needed. Apart from that, experimental work is not available for every molecule, so in general, the common theoretical approaches are more easily accessible.

One possibility for the theoretical determination of the biradical character is the calculation of the electronic structure using a multireference configuration interaction (MRCI) approach. In this case, the energetic relations between the closed-shell singlet and the open-shell singlet states are analyzed. Since open-shell singlet states can only be described using a linear combination of multiple slater determinants, the contributions of double excitations in the MRCI vector can be accounted for according to

$$y = \frac{2c_2^2}{c_1^2 + c_2^2}, \tag{1.24}$$

where c_1 and c_2 are the coeffiecients of the closed-shell and doubly excited electronic states.

A different approach is based on the definition of natural orbitals which are obtained by a unitary transformation of canonical orbitals so that they diagonalize the density matrix. The eigenvalues that result from the diagonalization procedure represent natural orbital occupation numbers (NOONs). They have shown to be particularly helpful in the characterization of the amount of open-shell singlet character in the wavefunction. NOONs close to one correspond to single unpaired electrons, so from this viewpoint a biradical is a molecule where both the highest occupied natural orbital (HONO) occupation number n_H as well as the lowest unoccupied natural orbital (LUNO) occupation number n_L are close to one.[96] The gap between HONO and LUNO therefore serves as a measure for the biradicalicity either directly or referencing to numbers between 0 and 1 by[97]

$$y = 1 - \frac{2T}{1 + T^2}, \tag{1.25}$$

with

$$T = \frac{n_H - n_L}{2}. \tag{1.26}$$

The main challenge in the theoretical modeling of both CIs as well as biradicals and biradicaloids is the necessity of a highly correlated multireference description of the electronic wavefunction, e.g. with MRCI or CASSCF methods which are computationally demanding. However, although standard DFT is based on a single Slater determinant and therefore fails with the proper description of biradicaloids, a convenient workaround is available through spin-flip DFT.[98]

1.5. Aim and Structure of the Thesis

It has been shown that CIs are inevitable for the description of relaxation dynamics upon photoexcitation in molecular systems. Detailed knowledge of the underlying

photophysical processes enables the microscopic understanding of biological systems and electronic devices, for example. However, the theoretical assessment of CIs has been mainly focused on local MECP optimization and the toolbox is lacking techniques that enable a global view on the intersection seam. The development of such methods is hence one of the goals of this thesis. Besides mechanistic understanding, the design of new materials is required in order to address today's issues in organic electronics. Especially the use of stable biradicals or biradicaloids is promising but also challenging because of their open-shell electronic structure. The second goal is therefore to provide a strategy for the theory-assisted tailored design of biradical organic molecules based on small building blocks. For both topics, the established advances in the field of metadynamics are employed and extended in order to provide automatic sampling methods that are widely applicable to complex molecular systems.

Due to the absence of a chromophoric unit that absorbs light in the visible or near UV range, photodynamics of carbohydrates have barely been studied. Chapter 2 of this thesis therefore deals with the role of ultrafast decay upon photoexcitation in glucose as a model for this class of biomolecules.[99] With the use of surface-hopping nonadiabatic dynamics[20] and the FISH method,[45] relevant conical intersections for this typical example of carbohydrates are studied and their role in the deactivation processes upon photoexcitation is discussed. Interestingly, the number of different CIs found to contribute to the photodynamics is huge in relation to the small size of the molecule, which motivates for a general exploration of the CI seam prior to computationally demanding multi-trajectory approaches.

In chapter 3, a new method for the automatic localization of CIs in molecular systems is introduced.[100] It is based on a multistate formulation of the metadynamics method[32] and allows for the efficient sampling of CI structures with minimal knowledge of the crossing seam structures prior to the simulation. Localization and characterization of CIs has been a vivid research field over the last decades, but contrary to the methods usually employed for this purpose,[79,80,82] the multistate metadynamics does not require an initial guess close to the expected CI. Instead, it can be initialized from any arbitrary ground state structure, which is illustrated by application on the furan molecule.

The following chapter 4 deals with the implementation of multistate metadynamics into the metaFALCON program package which has been made available free of charge as a python package.[101] Moreover, a comprehensive analysis of the applied CVs and parameters of the history-dependent bias potential performed on the 1,3-butadiene and benzene molecules reveals a general strategy for the study of new complex molecules. Finally, the employed bias potential is used to obtain a complete global picture of the energetic CI seam landscape by the utilization of Cremer-Pople ring puckering parameters[102] in 9H-adenine.

As a generalization of the multistate metadynamics, an approach for the auto-

matic sampling of quantum-property manifolds (ASQPM) is introduced in chapter 5 of the thesis.[103] It makes use of the metadynamics combined with electronic CVs in order to allow the exploration of functional landscapes in molecular systems. In this objective, a biradicalicity landscape for the rotation of methylene groups in the biradicaloid *p*-xylylene is provided. Furthermore, the tailored design of potentially stable biradicals based on the implementation of small building blocks into larger molecular systems is demonstrated using the [8]annulene molecule as an example. By forcing the 8-membered π-conjugated antiaromatic ring system into a biradical conformation, a promising scaffold is obtained which is further stabilized by the manipulation of steric and electronic properties through the introduction of substituents.

A general discussion of the obtained results is given together with an outlook in chapter 6, followed by a short summary of the thesis. Finally, supporting information to chapters 2, 4 and 5 is provided in the appendix.

2. Ultrafast Photodynamics of Glucose

Reprinted with permission from

J. Petersen, J. O. Lindner, R. Mitrić,
J. Phys. Chem. B **2018**, *122*, 19–27.

Abstract

We have investigated the photodynamics of β-D-glucose employing our field-induced surface hopping method (FISH), which allows us to simulate the coupled electron-nuclear dynamics, including explicitly nonadiabatic effects and light-induced excitation. Our results reveal that from the initially populated S_1 and S_2 states, glucose returns nonradiatively to the ground state within about 200 fs. This takes place mainly via conical intersections (CIs) whose geometries in most cases involve the elongation of a single O-H bond, while in some instances ring-opening due to dissociation of a C-O bond is observed. Experimentally, excitation to a distinct excited electronic state is improbable due to the presence of a dense manifold of states bearing similar oscillator strengths. Our FISH simulations explicitly including a UV laser pulse of 6.43 eV photon energy reveals that after initial excitation the population is almost equally spread over several close-lying electronic states. This is followed by a fast nonradiative decay on the time scale of 100-200 fs, with the final return to the ground state proceeding via the S_1 state through the same types of CIs as observed in the field-free simulations.

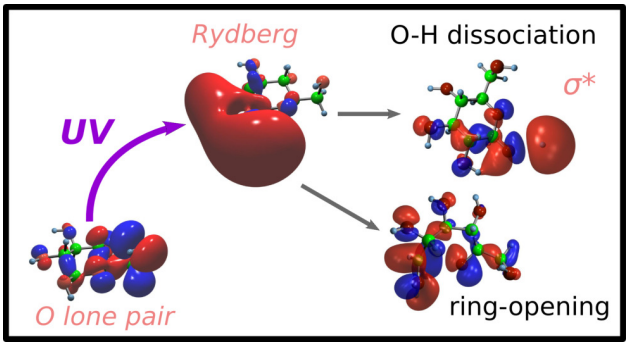

2.1. Introduction

Carbohydrates represent one of the most abundant classes of molecules present in biological systems. Owing to their extraordinarily rich structural variability, they are capable of numerous biological functions, e.g. as parts of nucleic acids for encoding genetic information or of membrane glycoproteins for molecular recognition and thus for signalling processes in living cells. Moreover, they are utilized by Nature as an energy storage, e.g. in polymers like starch, as well as for building cellular structures, most prominently in the form of cellulose, which is a crucial constituent of the cell walls of all green plants.

While there has been a large and long-standing effort in determining structural and chemical properties of carbohydrates both experimentally and theoretically (cf. [104–106] and references therein), only little is known about their photochemistry and photophysics. This is mainly due to the lack of chromophoric units in these molecules, for which reason instead of sharp, energetically low-lying absorption features only a broad absorption in the vacuum UV region is observed. Therefore, in natural terrestric environment, photodynamical processes in carbohydrates play a minor role, and direct spectroscopical investigations are, due to the large excitation energies, impeded as well. However, the situation is strongly different under extraterrestrial conditions, where high-energetic radiation is abundant. Indeed, a recent study showed that under conditions mimicking interstellar ice grains bioorganic molecules, amongst them carbohydrates up to ribose, are formed from simple precursors such as water, methanol and ammonia.[107] In this environment, photochemical reactions are likely to take place, and especially the question of photostability of the formed organic molecules is highly relevant in the context of chemical evolution and the origins of life.

What is experimentally known since quite a long time is that UV irradiation of aqueous carbohydrate solutions applying wavelengths down to 200 nm invokes photochemical reactions resulting in the formation of products which exhibit intense absorption between 240 and 270 nm.[108,109] In studies of the glucose molecule as a prototype example, it has been found that this is due to photodegradation processes in which molecules containing chromophoric subunits are formed, with the degradation process starting at the anomeric C^1 atom of the carbon chain.[110] This has lead to the suggestion that the electron lone pairs of the neighbouring oxygen atom in the pyranose ring may be involved in the photoexcited electronic states, giving rise to their $n\sigma^*$ character.[110] Such type of electronic states, alongside with those of $\pi\sigma^*$ character, have been intensively investigated theoretically in the recent years in a variety of organic molecules, and their general dissociative nature has been established.[111–116] However, detailed theoretical studies of the photophysical and photochemical properties of carbohydrates have been lacking until very recently.[117,118]

On the experimental side, the fact that continuous UV irradiation of carbohydrates leads to strongly UV-absorbing photoproducts has been exploited in the last years in the context of analytical techniques, such as the quantification of carbohydrate contents in beverages by spectrophotometric detection,[119] or as an alternative detection approach in capillary electrophoresis.[120–122] Usually, the detection process within the latter method involves UV absorption of the separated analytes. If the analyte molecule lacks a chromophoric subunit, as in the case of carbohydrates, then, frequently, chemical modification is performed, e.g. a chromophoric moiety is inserted, thus allowing for facile UV detection. An alternative approach, however, is based on irradiating the analytes with UV light of wavelengths down to 180 nm. This leads to photodegradation and the subsequent formation of reaction products that exhibit UV absorption above 260 nm, which is easily accessible to the standard detection techniques.[120,121] Investigation of the reaction products formed from glucose samples in this way has also confirmed that the degradation process is initiated by a ring opening reaction in which the bond between the C^1 carbon and the ring oxygen is broken.[121,122]

A detailed theoretical insight into the optical absorption and possible photochemical relaxation pathways of the glucose molecule has been gained by investigations of Tuna et al.[117] Glucose represents a building block found in various naturally occuring polymeric carbohydrates and thus can be considered as a basic representative of this class of molecules. Performing quantum chemical calculations of electronically excited states as well as determining the locations of conical intersections between ground and first excited electronic state, Tuna et al. identified possible channels by which electronically excited glucose may relax back to the ground state. Specifically, two main classes of conical intersections were found, in which either an O-H bond is elongated or the ring system of glucose is opened at the anomeric carbon atom. By assuming such deformed structures, the molecules may efficiently relax to the ground state, followed either by additional dissociative processes or by restoring the original molecules - however, with increased internal vibrational energy. Very similar findings have meanwhile also been obtained for the ribose molecule.[118]

In the present contribution, we aim to complement the aforementioned static calculations by an investigation of the dynamical processes occurring in photoexcited glucose. We will address both the specific relaxation mechanism following the population of particular excited states, as well as the photophysics induced by interaction of the molecule with a laser pulse of nonzero spectral width. For this purpose, nonadiabatic molecular dynamics simulations in the framework of our field-induced surface hopping method (FISH)[45] have been carried out, and the time scales of nonradiative relaxation as well as the nature of the corresponding nuclear rearrangements have been analysed.

2.2. Computational Methods

The structure of β-D-glucose was optimized and the harmonic frequencies were determined using the Turbomole program package[123] in the frame of three different approaches: density functional theory (DFT) employing the B3LYP functional[124] and (i) the 6-31++G basis set[125,126] as well as (ii) the 6-31++G** basis set[125–127] and (iii) second order Møller-Plesset perturbation theory (MP2) employing the aug-cc-pVDZ basis set.[128,129] Subsequently, the normal modes were used to sample a Wigner distribution corresponding to a temperature of 250 K for each method, from which initial coordinates and momenta for use in the dynamics simulations were generated. The nonradiative relaxation dynamics of electronically excited glucose was simulated in the frame of Tully's surface hopping method.[20] For this purpose, the electronic energies and gradients were obtained "on the fly" using Turbomole with the same DFT functional and basis set as stated above along classically propagated nuclear trajectories. The excited state energies and gradients were calculated using linear-response time-dependent density functional theory (LR-TDDFT).[130] The nonadiabatic coupling elements were calculated from the LR-TDDFT eigenvectors according to the procedure of Mitrić et al.[131] Using these quantities, the electronic population dynamics was simulated along each trajectory by solving the time-dependent Schrödinger equation, and the resulting populations were employed to compute hopping probabilities according to Ref.[43,44] In order to ensure conservation of the total energy of each trajectory, the velocities were uniformly rescaled after a successful surface hop. The propagated classical ensemble consisted of 30 trajectories which were initiated in the S_1 and S_2 state, respectively. The propagation starting from the S_1 state was performed using both the 6-31++G basis set and its counterpart containing polarization functions, 6-31++G**. The results using these two basis sets provide essentially identical excited state lifetimes and reaction channels (cf. Supporting Information, Fig. A.1-A.3). In particular, the process of O-H bond stretching, which is important in the excited state dynamics of glucose (cf. Results and Discussion) is equally well described by the two approaches, as can be also inferred from the very similar behaviour of the S_0 and S_1 electronic state energies along the O-H bond stretching coordinate, which is presented in Fig. A.4 of the Supporting Information. Therefore, the further simulations were performed using the computationally more efficient basis set 6-31++G. For the propagation of the nuclei, the classical Newton's equations were solved numerically using the velocity Verlet algorithm with a time step of 0.25 fs. The total propagation time was 200 fs. When reaching regions near S_0-S_1 conical intersections, which could not be accurately described by TD-DFT,[132] those trajectories which were previously situated in the S_1 state were continued in the ground state, while those residing in higher electronic states were aborted. Trajectories were subsequently classified according to their structure at the conical intersections.

In order to provide a comparison of the LR-TDDFT approach for the nonadiabatic dynamics to an ab initio-based methodology, we performed additional surface-hopping simulations using an ensemble of 30 trajectories starting from the S_1 state and employing the algebraic diagrammatic construction through second order (ADC(2)) method[133] together with the aug-cc-pVDZ basis set.[128,129] The implementation of the nonadiabatic couplings straightforwardly follows our approach for LR-TDDFT,[131] which has been also previously employed by Plasser et al.[134]

For a more realistic description of the laser excitation into a manifold of close-lying states with comparable oscillator strengths, in addition to the field-free nonadiabatic dynamics simulations also the field-induced surface hopping method (FISH)[45] was applied, again employing the TDDFT (B3LYP/6-31++G) approach. For this purpose, 100 trajectories sampled from the Wigner function described above were propagated over 300 fs within a manifold of 10 electronic states. The excitation field was taken to be of Gaussian shape, with a field intensity of $7.9{\cdot}10^{12}\,\frac{\mathrm{W}}{\mathrm{cm}^2}$, a central frequency corresponding to 6.43 eV and a full width at half maximum (FWHM) of 30 fs. Unlike the field-free simulations, the total energy of a given trajectory is not conserved while the laser pulse is present. Therefore, velocity rescaling after a surface hopping event was only enabled for the time period after 50 fs, when the pulse had ceased.

2.3. Results and Discussion

2.3.1. UV Absorption Spectrum

The calculated absorption spectrum of β-glucose, obtained from the 20 lowest excited electronic states in the frame of TDDFT (B3LYP/6-31++G) for each of the 100 initial conditions sampled from a harmonic Wigner distribution at 250 K, is presented in Fig. 2.1. It is characterized by a weak onset around 5.2 eV, with appreciable oscillator strengths above 5.5 eV. Up to 7 eV, the oscillator strength steadily increases. Its subsequent drop is due to the limited number of states included in the calculation. Compared to experimental data obtained in aqueous solution,[110] the absorption onset is red-shifted by about 0.5 eV. As has been shown by Tuna et al.,[117] the energetic position of the excited states is slightly underestimated by TDDFT, and using correlated ab initio methods such as CC2 leads to a blue shift of $\sim$0.3 eV. The electronic state character was shown to be essentially the same in both methods. This gave us confidence to proceed with employing the computationally less demanding TDDFT approach for dynamics simulations.

The electronic absorption of glucose is characterized by the absence of distinct intense excited states. Instead, the energy range up to 7 eV contains already about 10 excited states with relatively low oscillator strengths. For the optimized ground

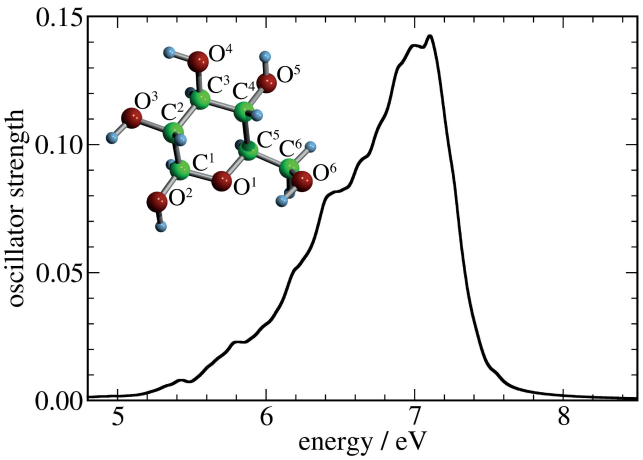

Figure 2.1.: Electronic absorption spectrum of the ensemble of 100 initial conditions. For each structure, the lowest-lying 20 excited states have been calculated using TD-DFT (B3LYP/6-31++G). The individual transitions have been convolved by a Lorentzian width of 0.1 eV. The optimized structure of β-D-glucose is shown as an inset.

state structure, which is also shown in Fig. 2.1, the analysis of the lowest 10 excited states is summarized in Table 2.1, and the relevant molecular orbitals are depicted in Fig. 2.2. The excited states under investigation all share similar electronic character, with the leading excitations occuring from orbitals representing linear combinations of oxygen lone pairs to Rydberg-type virtual orbitals. It has been shown previously that these Rydberg orbitals change their nature upon elongation of C-O or O-H bonds, ultimately assuming σ^* character.[117] Therefore, the typical dissociative behaviour of nσ^* states is expected to show up in the photodynamics.

2.3.2. Field-Free Surface-Hopping Dynamics

For the investigation of dynamical processes occurring in glucose after photoexcitation, in a first step, the nonradiative relaxation of the molecule has been simulated starting from the first or second excited electronic state, respectively. The electronic state population dynamics for an ensemble of 30 trajectories initiated in the S_1 state is shown in Fig. 2.3. It is evident that, besides transient population of the S_2 state, fast internal conversion to the ground state takes place, which is completed after 200 fs. The mechanism of this ultrafast process can be unravelled by analysing some typical trajectories. In Fig. 2.4, a short trajectory is presented in which the dynamics in the S_1 state straightforwardly leads to a conical intersection (CI) with the ground state which is reached already after 15 fs. This is accompanied by elongation of the

State	Transition energy (eV)	Oscillator strength	Composition (%)
S_1	6.284	0.0033	H→L (48)
			H−1→L (39)
S_2	6.410	0.0042	H−1→L (37)
			H→L (31)
			H→L+1 (12)
S_3	6.543	0.0004	H−1→L+1 (59)
			H→L+1 (19)
S_4	6.602	0.0155	H→L+1 (34)
			H−1→L+1 (25)
S_5	6.680	0.0003	H−2→L+1 (35)
			H−2→L (16)
			H→L+3 (14)
S_6	6.713	0.0051	H−2→L (42)
			H→L+3 (14)
S_7	6.757	0.0074	H−2→L (22)
			H−3→L+1 (20)
			H−3→L (17)
			H→L+3 (10)
S_8	6.816	0.0015	H→L+2 (25)
			H→L+1 (19)
			H−2→L+1 (12)
S_9	6.886	0.0027	H→L+2 (51)
			H→L+3 (25)
S_{10}	6.954	0.0075	H−1→L+2 (65)
			H−3→L (17)

Table 2.1.: Excited electronic states for the optimized structure of β-D-glucose obtained by TDDFT (B3LYP, 6-31++G).

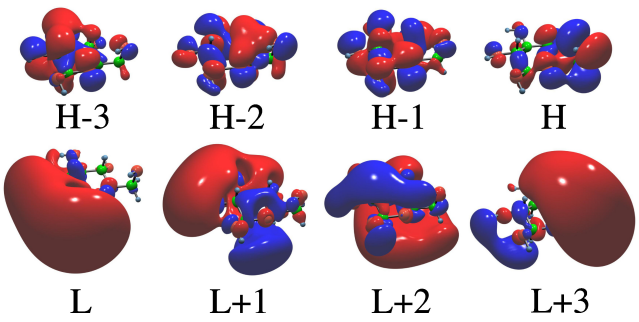

Figure 2.2.: Molecular Kohn-Sham orbitals for the optimized structure of β-D-glucose. H denotes the highest occupied, L the lowest unoccupied molecular orbital.

O^2-H bond (cf. structure shown in Fig. 2.1). During the dynamics, the excited S_1 state is of $n\sigma^*$ character, which is consistent with previous findings of the dissociative nature of such states.[117]

Besides O-H bond elongation, opening of the pyranose ring has been observed as a second photochemical channel, as illustrated in Fig. 2.5. In this case, the initial stage of the dynamics is similar to the one shown in Fig. 2.4, leading first to elongation of an O-H bond and closing of the S_1-S_0 energy gap. However, before reaching the conical intersection, a hop to the ground state occurs. This leads to energy transfer from the electronic degrees of freedom to the nuclear vibrations, especially invoking large-amplitude vibrations of the O-H bond. Nonetheless, bond breaking does not take place in the ground state here. Rather, the large vibrational energy together with the fact that the electronic system resides in a superposition of the S_0 and S_1 states enables the trajectory to hop back to the S_1 state at 80 fs. Subsequently, the motion is directed towards a conical intersection characterized by a ring-opening motion (cf. the increased C^1-O^1 distance shown in the lower part of Fig. 2.5).

These examples illustrate the two general possibilities found for nonradiative decay in the glucose molecule: Either the return to the ground state proceeds via a CI connected to O-H bond elongation, or via another one which invokes opening of the pyranose ring. Which path a given trajectory actually follows depends sensitively on the initial conditions. As a general trend, the CIs connected to O-H bond elongation are reached much more rapidly, as can be inferred from Fig. 2.6, in which the energies and arrival times of all conical intersections traversed by the propagated trajectories are presented. These O-H-dissociative CIs are mostly reached within 30 fs of propagation time, whereas to arrive at the CIs connected to ring opening, usually a time between 100 and 200 fs is needed. It is interesting to note that the OH-dissociative CIs tend to lie energetically above the ring-opening

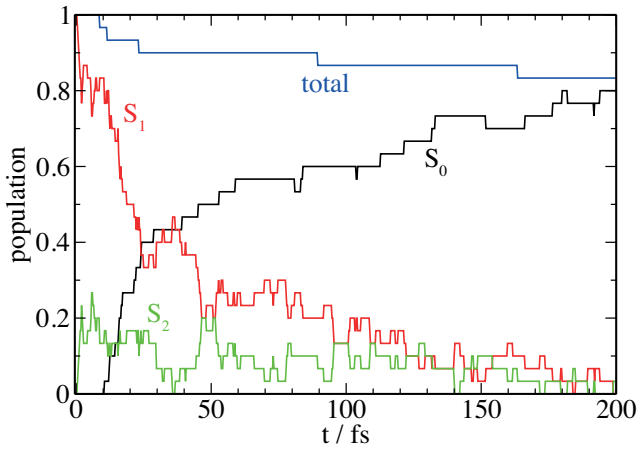

Figure 2.3.: Time-dependent electronic state populations for nonadiabatic dynamics starting in the S_1 state. The decrease of the total population is due to such trajectories that resided in the S_2 state when reaching the vicinity of an S_0-S_1 CI, where the propagation was stopped.

ones, but are still reached faster and by the majority of trajectories (about 67 % vs. 23 %). This confirms previous suggestions of Tuna et al. who investigated static reaction paths connecting the Franck-Condon region with the two types of conical intersections discussed above and predicted the O-H dissociative CIs to be dominantly involved in the dynamical relaxation processes.[117] A possible explanation for this finding can be based on the actual distances along the pathways the trajectories have to cover in the 3N dimensional configuration space from the initial points of the dynamics to the vicinity of the respective CI. For the two subsets of trajectories reaching either the O-H dissociative CIs or the C-O ring opening ones, these distances amount to 7.8 vs. 24.4 Å in average, clearly indicating that the O-H CIs are reached along a shorter path. Although for most of the trajectories the return to the ground state involves the passage through CIs in which specific bonds are elongated, the actual breaking of bonds in the ensuing ground state dynamics is only observed as a minor channel, about 80 % of the trajectories finally returning to the original cyclic form of the molecule. In the remaining cases, reactions such as abstraction of H or H_2O or forming of open-chain molecules are observed.

In order to provide a comparison between our TDDFT-based approach for the nonadiabatic dynamics and a fully ab-initio-based methodology, we have performed additional surface-hopping simulations starting in the S_1 state in the frame of the ADC(2) method as described in the Computational Section. The resulting population dynamics, presented in Fig. 2.7, shows that the general time scale of the nonadiabatic return to the ground state is about 100 fs, slightly faster than in

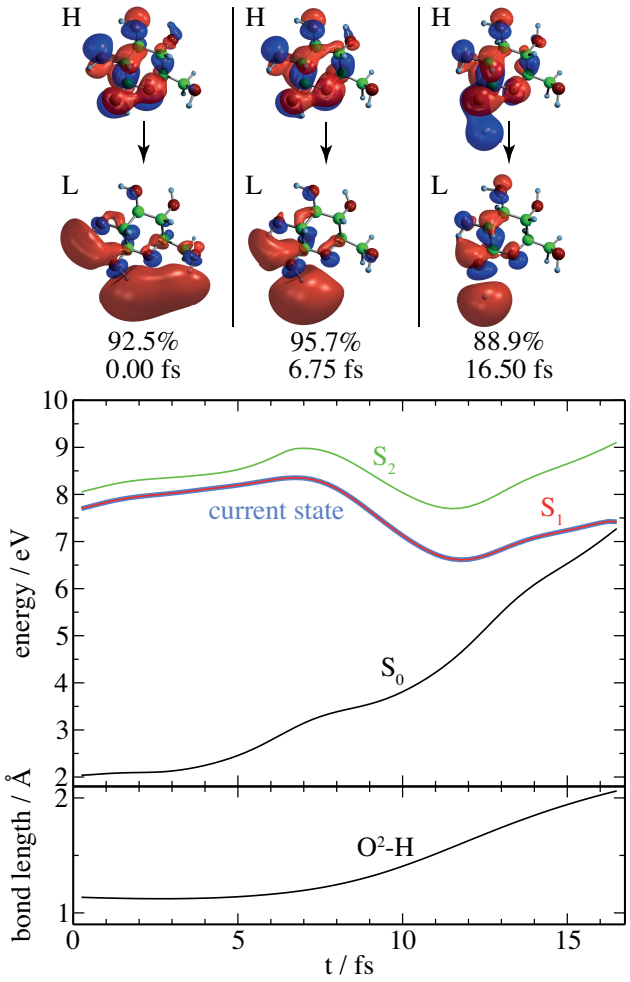

Figure 2.4.: (Middle) Energies of the lowest 3 electronic states along a selected trajectory initiated in the S_1 state, where the O^2-H-elongation leads to a conical intersection. Energies are given relative to the optimized geometry of the ground state. (Top) Molecular orbitals showing the main excitation at distinct points in time. (Bottom) O^2-H bond length along the trajectory.

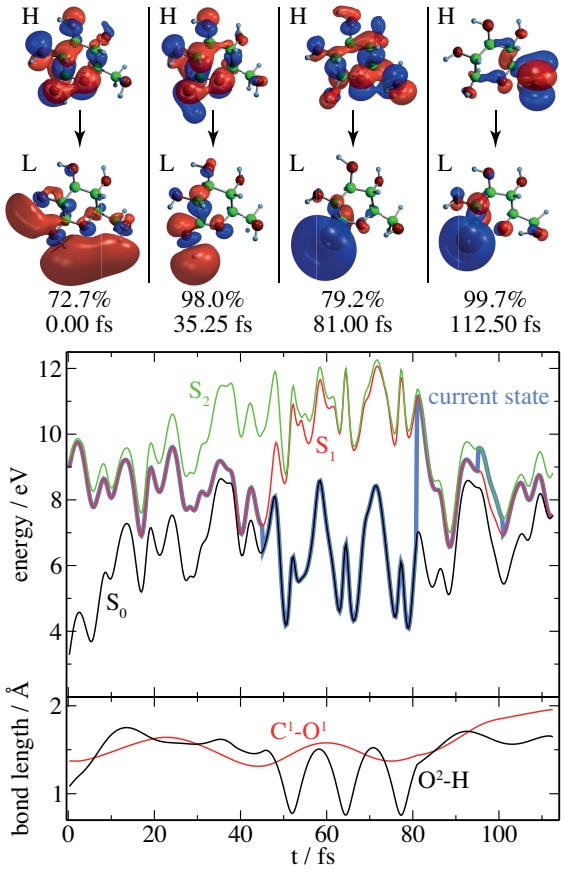

Figure 2.5.: (Middle) Energies of the lowest 3 electronic states along a selected trajectory initiated in the S_1 state, where the C^1-O^1 ring-opening leads to a conical intersection. Energies are given relative to the optimized geometry of the ground state. (Top) Molecular orbitals showing the main excitation at distinct points in time. (Bottom) O^2-H and C^1-O^1 bond lengths along the trajectory.

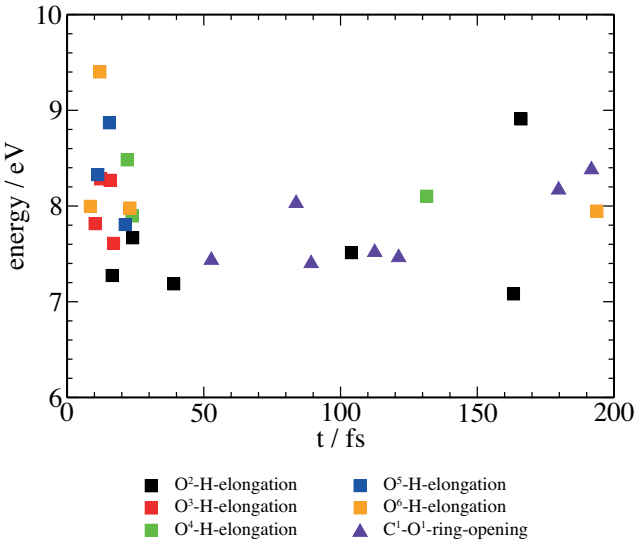

Figure 2.6.: Ground state energies of the trajectories initiated in the S_1 state at the final time steps when the TDDFT energy gap between the S_0 and S_1 states closes. Energies are given relative to the optimized geometry of the ground state. The different types of conical intersections (CIs) reached are classified according to the respective geometry changes as O-H elongation (squares) and as ring-opening (triangles). The CIs characterized by O-H elongation are further colour-coded according to which specific bond is affected.

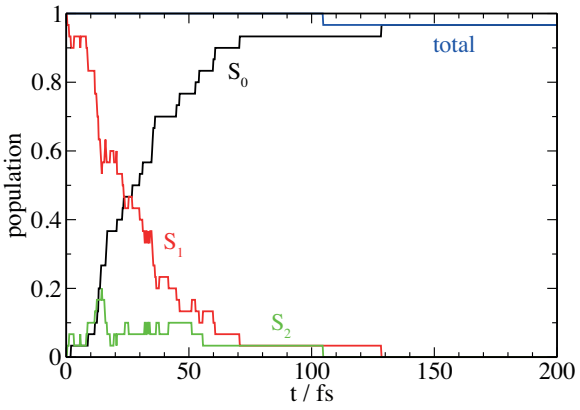

Figure 2.7.: Time-dependent electronic state populations for nonadiabatic ADC(2) dynamics starting in the S_1 state.

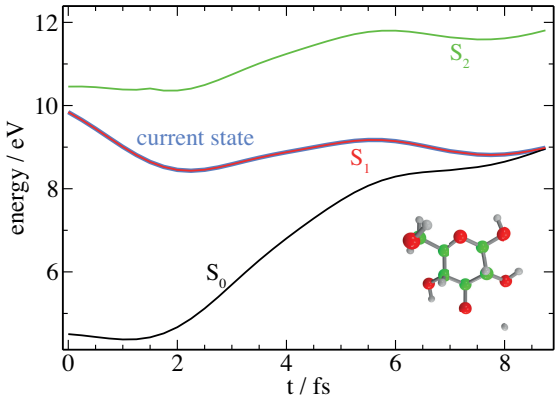

Figure 2.8.: Energies of the lowest 3 electronic states along a selected ADC(2) trajectory initiated in the S_1 state, where the O-H-elongation leads to a conical intersection. Energies are given relative to the optimized geometry of the ground state.

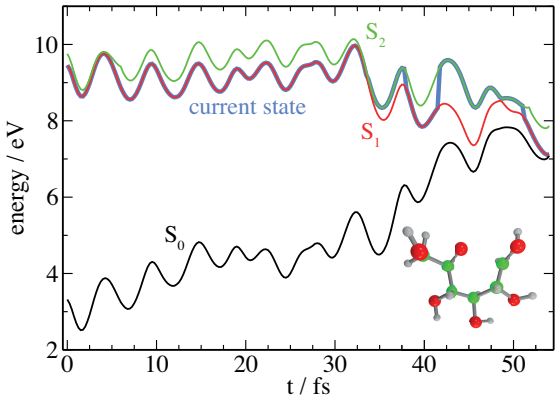

Figure 2.9.: Energies of the lowest 3 electronic states along a selected ADC(2) trajectory initiated in the S_1 state, where the C^1-O^1 ring-opening leads to a conical intersection. Energies are given relative to the optimized geometry of the ground state.

the case of TDDFT, but of the same order of magnitude. Similarly, also the pathways taken towards the conical intersections clearly correspond to those seen in the TDDFT simulations. The majority of trajectories approaches the S_0/S_1 degeneracy via O-H bond stretching in a sub-50 fs time scale. An illustrative trajectory for this process is presented in Fig. 2.8, where the CI is reached already after 9 fs. A much smaller part of the trajectories follows a path where the pyranose ring of the molecule opens when the CI is approached, as is exemplified by the trajectory shown in Fig. 2.9. Also in agreement with the TDDFT simulations, this process takes longer time, more than 50 fs in the present case. Regarding the fate of the trajectories after return to the ground state, the ADC(2) dynamics, which reduces to MP2 in the ground state, shows a high amount of completed O-H bond dissociations, which have only rarely been observed in the TDDFT simulations. Closer inspection of the electronic energies along an O-H bond stretching coordinate, as shown in Fig. A.4 of the Supporting Information, reveals that this is due to a continuous decrease of the electronic energies for increasing bond lengths, while in the case of TDDFT an asymptotically constant value is adopted. Due to a well-known deficiency of MP2 in describing situations where degenerate occupied and virtual orbitals occur, such as homolytic bond breaking,[135] this behaviour of the trajectories can be clearly qualified as incorrect, and the MP2 ground state dynamics following the passage through the CI is not further taken into consideration.

Since the electronic absorption spectrum of glucose is characterized by many excited states of similar oscillator strength, the investigation of nonadiabatic relaxation cannot be restricted to simulations starting in the lowest excited state only. Therefore, we studied the influence of the initial state selection on the course of the dynamics by performing additional simulations started in the S_2 state. The resulting population dynamics is presented in Fig. 2.10 and shows that from the initial S_2 state the population transfer takes place rapidly (within less than 20 fs) to the S_1 state, which reaches a peak population of 60 % after 10 fs. Subsequently, the population of both states decays on a time scale of 100 - 150 fs. After the simulation time of 200 fs, the population has essentially completely returned to the ground state.

The decay mechanisms found in this simulation are very similar to those occurring for trajectories started in the S_1 state. In particular, this is the case for trajectories that approach an O-H-dissociative CI via an $n\sigma^*$ excited state, as shown in Fig. 2.11. Although started in the S_2 state, hopping to the S_1 state takes place very fast and the approach to the CI again occurs on a short time scale of about 20 fs.

Besides O-H dissociation, deactivation via ring opening is observed as well. In the case of trajectories initiated in the S_1 state, it has already become evident that in order to reach a ring-opening CI, the molecule has to bypass the O-H dissociative CIs which lie much closer to the starting geometry of the dynamics. In the example presented in Fig. 2.5 above, this was possible since the trajectory intermediately changed to the ground state, and only after some time, its large vibrational energy

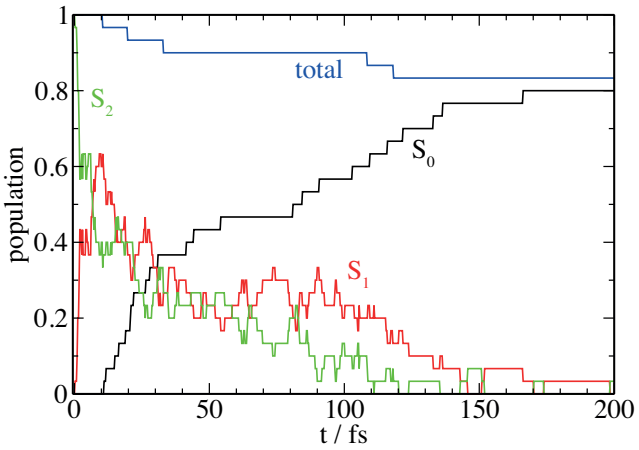

Figure 2.10.: Time-dependent electronic state populations for nonadiabatic dynamics starting in the S_2 state. The decrease of the total population is due to such trajectories that resided in the S_2 state when reaching the vicinity of an S_0-S_1 CI, where the propagation was stopped.

allowed it to populate the excited state again. The illustrative trajectory shown in Fig. 2.12 behaves differently. Here, the regions of the potential energy surface which are close to the O-H dissociative CI, characterized by elongation of the O-H bond (cf. lower part of Fig. 2.12), are avoided by the fact that the molecule still resides in the S_2 state when approaching geometries of elongated O-H bonds. Therefore, no direct transition to the ground state is possible. Instead, the dynamics proceeds for some time on the S_2 state before switching to the S_1 state after 45 fs. Now the molecule is situated in a region of the S_1 potential energy surface from where access to a ring-opening CI is possible, which is reached after a propagation time of about 100 fs.

The increased possibilities to avoid the direct approach to O-H dissociative CIs are also reflected by the fact that a higher number of trajectories undergoes ring-opening after a propagation time of more than 70 fs, as can be inferred from Fig. 2.13. However, the main deactivation channel remains O-H dissociation on a sub-50-fs time scale. As for the trajectories initiated in the S_1 state, the lengths of the pathways between the initial geometry and the vicinity of the CI have been calculated, resulting in similar average values of 8.0 and 19.8 Å for the O-H dissociative and C-O ring-opening CIs, respectively. Therefore, also in this case the pathways towards the O-H dissociative CIs are distinctly shorter. After return to the ground state, the majority of the molecules re-assumes the cyclic form of glucose without undergoing a chemical reaction, also similar to the dynamics initiated in the S_1 state.

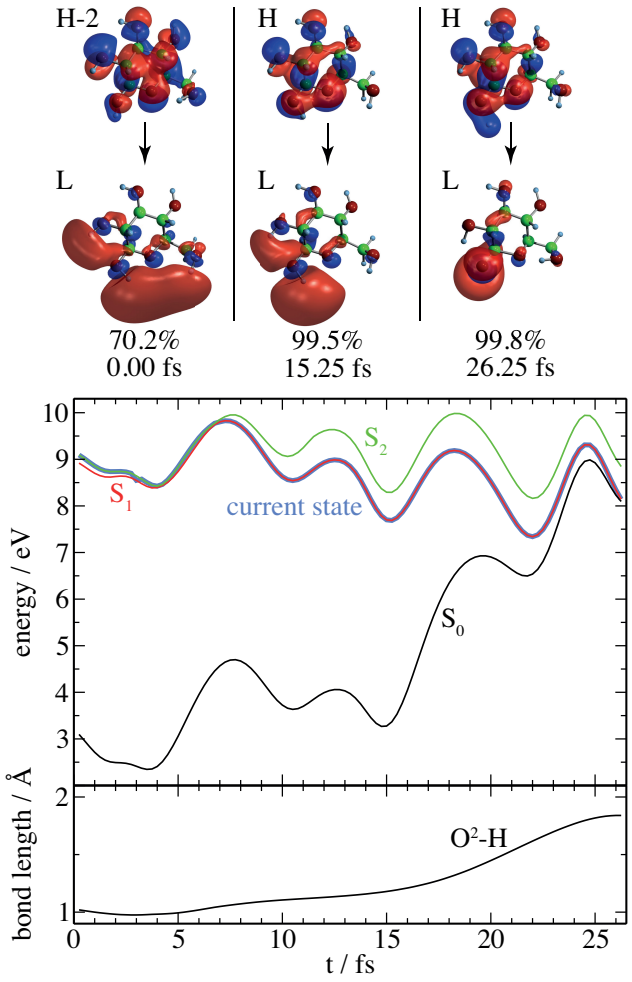

Figure 2.11.: (Middle) Energies of the lowest 3 electronic states along a selected trajectory initiated in the S_2 state, where the O^2-H-elongation leads to a conical intersection. Energies are given relative to the optimized geometry of the ground state. (Top) Molecular orbitals showing the main excitation at distinct points in time. (Bottom) O^2-H bond length along the trajectory.

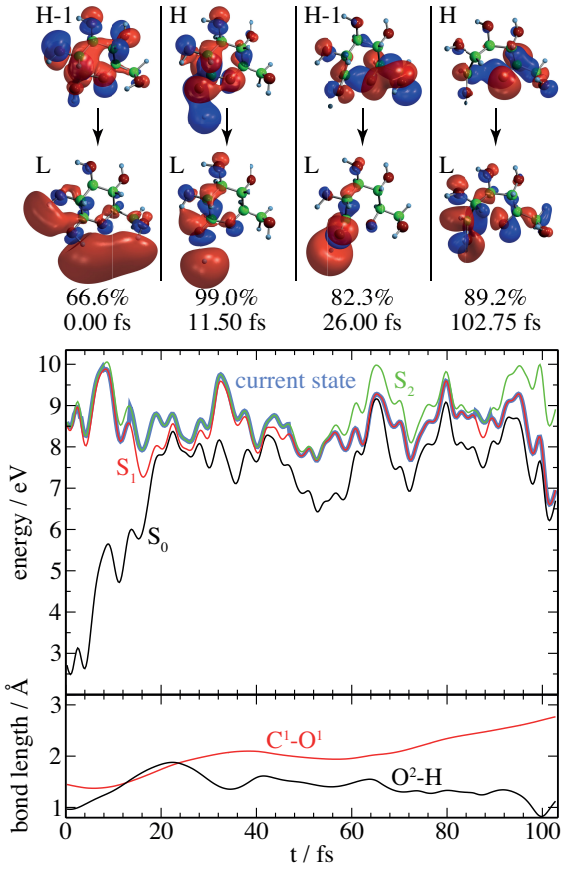

Figure 2.12.: (Middle) Energies of the lowest 3 electronic states along a selected trajectory initiated in the S_2 state, where the C^1-O^1 ring-opening leads to a conical intersection. Energies are given relative to the optimized geometry of the ground state. (Top) Molecular orbitals showing the main excitation at distinct points in time. (Bottom) O^2-H and C^1-O^1 bond lengths along the trajectory.

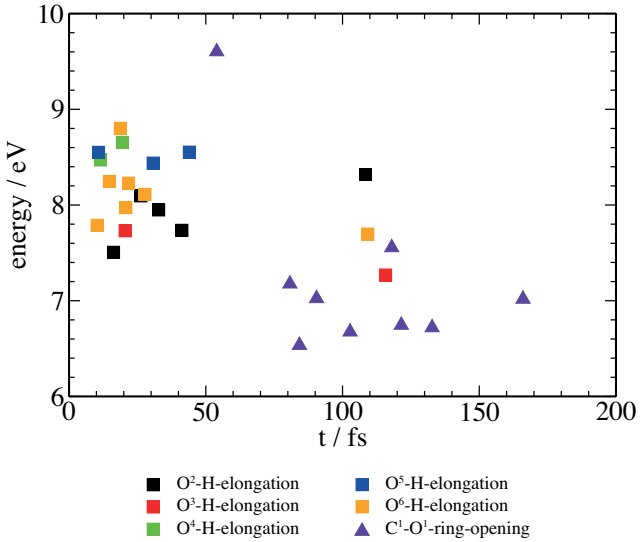

Figure 2.13.: Ground state energies of the trajectories initiated in the S_2 state at the final time steps when the TDDFT energy gap between the S_0 and S_1 states closes. Energies are given relative to the optimized geometry of the ground state. The different types of CIs reached are classified according to the respective geometry changes as O-H elongation (squares) and as ring-opening (triangles). The CIs characterized by O-H elongation are further colour-coded according to which specific bond is affected.

2.3.3. Field-Induced Surface Hopping Dynamics

In order to achieve a more realistic simulation of the initial light-induced excitation processes in glucose, additional FISH simulations with explicit light excitation have been carried out, in which a pump laser pulse of 193 nm (6.43 eV) central wavelength and a temporal FWHM of 30 fs was employed. Given the high number of energetically close-lying excited states, which also bear comparable oscillator strengths, the light pulse populates a manifold of electronic states rather than a single one, as can be seen from the time-dependent populations presented in Fig. 2.14. The overall excitation efficiency is about 80 %. However, 25 % of the trajectories already return to the ground state within the laser pulse duration due to the coupling with the field. After the field has ceased, the photoexcited trajectories exhibit several mechanisms for nonradiative decay. In general, the deactivation is fast and essentially completed after 300 fs, regardless of the specific states populated during the laser excitation. The transition to the ground state proceeds through the same types of CIs as found in the field-free dynamics. However, due to the intake of energy in the molecular system as a consequence of the light-molecule interaction, the temporal and energetic distribution of the CIs reached during the dynamics is different, as can be seen from Fig. 2.15. Most prominently, the time to reach O-H dissociative CIs can be much longer than the $\sim$50 fs observed in the field-free case. This might be due to the longer time needed for a highly excited trajectory to reach the S_1 state in which the respective CI is accessible. In addition, the number of ring-openings observed is lower, and these can occur at higher energies compared to the field-free dynamics. This may result from the different paths on the PES the trajectories follow when excited to higher-lying excited states instead of S_1 and S_2 only, allowing the trajectories to reach higher-energy parts the S_1-S_0 intersection seam. For some trajectories, instead of one of the aforementioned relaxation pathways via CIs, return to the ground state is also observed in regions of the PES far away from CIs due to residual nonadiabatic couplings that invoke changes of the electronic state coefficients. This mechanism is particularly well possible if it is, as in the present case, preceded by the creation of an electronic superposition state due to interaction with the laser field. After return to the ground state, the majority of trajectories anew assumes the original cyclic structure, similar to the case of the field-free dynamics. In a few cases, reactions are observed, involving H atom abstraction in one instance, and 6 occurrences of a ring opening reaction, which may be also due to the larger internal energy of the photoexcited trajectories.

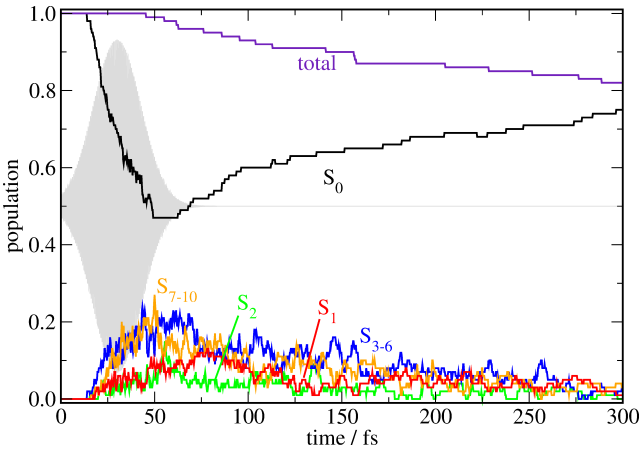

Figure 2.14.: Time-dependent electronic state populations for the field-induced dynamics of glucose in the manifold of 10 electronic states. The excitation field is indicated in grey in the background. The decrease of the total population is due to such trajectories that resided in the higher excited states above S_1 when reaching the vicinity of an S_0-S_1 CI, where the propagation was stopped.

2.4. Conclusions

The nonradiative relaxation of β-D-glucose from the lowest-lying excited electronic states takes place on a time scale of $\sim$ 100-200 fs. Return to the electronic ground state proceeds essentially quantitatively due to the presence of conical intersections (CIs) that can be easily accessed after photoexcitation. The geometries at which these CIs occur are consistent with those previously found by static calculations:[117] In most cases, elongation of O-H bonds takes place, while in some instances ring-opening due to dissociation of a C-O bond is observed. Although the O-H dissociative CIs tend to lie higher in energy, they are more easily reached due to the smaller geometric deformations necessary.

Since the UV absorption of glucose is characterized by the presence of many close-lying electronic states of similar oscillator strength, a direct simulation of the light-induced excitation process in the frame of the FISH method has been performed as well, using a field frequency corresponding to 6.43 eV photons. In this way, instead of a well defined single electronic state, a complex superposition is excited. Although this leads to a more involved electronic excitation and relaxation dynamics, the nuclear motion is qualitatively similar to the results of the field-free simulations, and the final return to the ground state occurs on the same time scale via the same types of CIs.

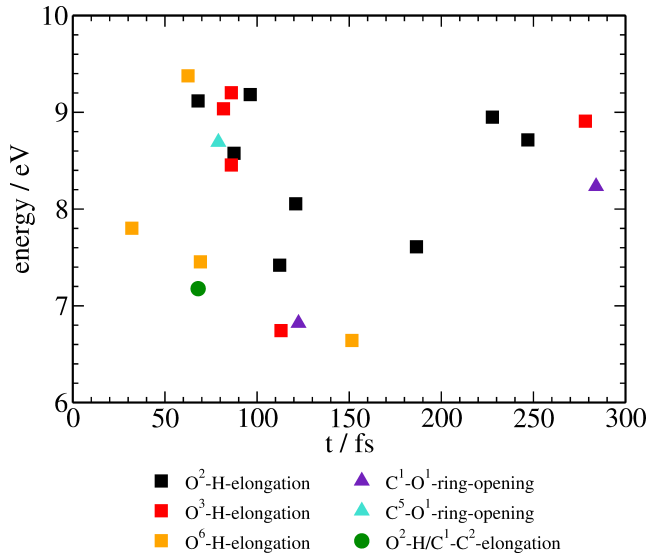

Figure 2.15.: Ground state energies of the photoexcited trajectories at the final time steps when the TDDFT energy gap between the S_0 and S_1 states closes. Energies are given relative to the optimized geometry of the ground state. The different types of CIs reached are classified according to the respective geometry changes as O-H elongation (squares) and as ring-opening (triangles). The CIs characterized by O-H elongation are further colour-coded according to which specific bond is affected.

Supporting Information

Additional computational details are provided: Cartesian coordinates of the optimized ground state structure of glucose, excitation energies and oscillator strengths of S_1 and S_2 obtained by TDDFT (B3LYP/6-31++G and 6-31++G**) and ADC(2)/aug-cc-pVDZ, electronic state populations and energies along selected nonadiabatic trajectories for TDDFT (B3LYP/6-31++G**) surface hopping dynamics, S_0 and S_1 energy scan along an O-H bond stretching coordinate for TDDFT (B3LYP/6-31++G, 6-31++G** and aug-cc-pVDZ) and ADC(2)/aug-cc-pVDZ.

Acknowledgment

We wish to thank Dr. Deniz Tuna for drawing our attention to this topic during the Symposium on Theoretical Chemistry 2015 in Potsdam, Germany. Furthermore, we acknowledge financial support by the Deutsche Forschungsgemeinschaft, project FOR1809, as well as by the European Research Council, Consolidator Grant DYNAMO (Grant No. 646737).

3. Multistate Metadynamics for Automatic Exploration of Conical Intersections

Reprinted with permission from

J. O. Lindner, M. I. S. Röhr, R. Mitrić,
Phys. Rev. A **2018**, *97*, 052502.

Abstract

We introduce multistate metadynamics for automatic exploration of conical intersection seams between adiabatic Born-Oppenheimer potential energy surfaces in molecular systems. By choosing the energy gap between the electronic states as a collective variable the metadynamics drives the system from an arbitrary ground-state configuration toward the intersection seam. Upon reaching the seam, the multistate electronic Hamiltonian is extended by introducing biasing potentials into the off-diagonal elements, and the molecular dynamics is continued on a modified potential energy surface obtained by diagonalization of the latter. The off-diagonal bias serves to locally open the energy gap and push the system to the next intersection point. In this way, the conical intersection energy landscape can be explored, identifying minimum energy crossing points and the barriers separating them. We illustrate the method on the example of furan, a prototype organic molecule exhibiting rich photophysics. The multistate metadynamics reveals plateaus on the conical intersection energy landscape from which the minimum energy crossing points with characteristic geometries can be extracted. The method can be combined with the broad spectrum of electronic structure methods and represents a generally applicable tool for the exploration of photophysics and photochemistry in complex molecules and materials.

3.1. Introduction

The Born-Oppenheimer (BO) approximation, the cornerstone of molecular physics, breaks down when molecules get electronically excited. This is most dramatically reflected in the presence of conical intersections (CI)[49–51] between BO potential energy surfaces (PES). A wide range of light-induced processes including vision in biology,[54,72] photostability of DNA,[136] a plethora of organic photochemical reactions,[137] and charge separation in photovoltaic devices[73] are governed by the efficient nonradiative transitions mediated by a strong coupling between electronic and nuclear dynamics at CIs. In this sense, they play a role in photophysics and photochemistry analogous to the transition states in the ground-state chemistry. However, unlike the transition states, CIs are not isolated points on the PES but form a multidimensional seam. A significant effort has been invested both experimentally and theoretically to identify and characterize CIs.[72,76,77,138–140] A number of algorithms has been developed with the aim to search for the minimum energy configurations within the CI seam, since their knowledge allows us to predict the fate of a photoexcited molecule.[79,80,82] In addition to these local optimization algorithms, methods have been also proposed for location of minimum energy crossing points (MECP), which are closest in terms of a mass-weighted distance to a predefined reference structure.[141] However, all these methods require a reasonable initial guess for the CI geometry. Alternatively, more elaborate approaches for the automated search of CI geometries based on the anharmonic downward distortion following (ADDF) and artificial force-induced reaction (AFIR) methods,[83,84,142,143] as well as the nudged elastic band method,[144] have also been introduced and applied for the exploration of conical intersection seams. Recent studies have emphasized the importance of conical intersections in coherent vibronic dynamics that involves nonadiabatic driving forces associated with the vibrational motion along the tuning modes.[145] While such effects can only be properly investigated in the frame of quantum dynamics simulation, systematic and unbiased sampling of the conical intersection seam might help in construction of reliable (diabatic) Hamiltonians that are needed for such simulations. Since CIs are usually found in the range of several eV above the ground-state equilibrium structure, it would be desirable to develop an accelerated molecular dynamics technique that is able to reach and sample the CI seam starting directly from the ground-state minimum. The metadynamics, introduced by Parrinello and coworkers,[32,33,35,146–148] represents an ingeniously simple sampling method that uses collective variables (CVs) to drive transitions between different barrier-separated basins on the PES, allowing for systematic sampling of the PES as well as determination of free energies. Depending on the problem to be solved, a wide variety of CVs has been used, ranging from simple geometrical quantities to complex variables constructed by machine learning and dimensionality reduction techniques.[148,149] In this article, we introduce a multistate metadynamics

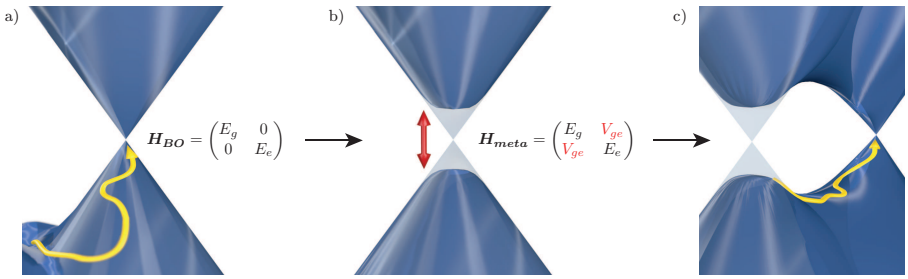

Figure 3.1.: Scheme of the algorithm. (a) Starting in the ground-state minimum, forces resulting from the bias potential V_G using energy gap CV drive the system toward the intersection seam (yellow trajectory). (b) Upon reaching the seam, an off-diagonal coupling V_{ge} (red) is added to the electronic Hamiltonian, opening a gap in the vicinity of the intersection point. The metadynamics subsequently explores configurations with nearly degenerate ground- and excited-state energies until the next intersection point is reached (c).

method for automatic exploration of conical intersection seams and identification of MECP.

3.2. Method

The central idea of our multistate metadynamics is to use the energy gap between the ground and excited electronic states as a collective variable to drive the system toward the CI starting from any ground-state structure. For this purpose, the system is propagated using the Newtonian equations of motion, which for the ith particle read

$$m_i \ddot{\mathbf{R}}_i = -\nabla_i [E_g + V_G(t)], \tag{3.1}$$

where E_g represents the ground-state PES and $V_G(t)$ is a history-dependent bias potential:

$$V_G(t) = \sum_{t'=\tau_G, 2\tau_G, \ldots}^{t} w \exp\left\{ -\frac{[\Delta E_{meta}(t) - \Delta E_{meta}(t')]^2}{2\delta s^2} \right\} \times \Theta(\Delta E_{meta}(t') - \epsilon), \tag{3.2}$$

which is dependent on the modified energy gap ΔE_{meta}, and w and δs represent the fixed height and width, respectively. The bias potential is updated at regular time steps τ_G but only if the value of the gap is larger than a numerical threshold ϵ, which is enforced by the presence of the Heaviside theta function $\Theta(\Delta E_{meta} - \epsilon)$

in Eq. (3.2). Starting from a minimum on the ground-state PES, the bias potential will drive the system toward the CI seam by systematically lowering the energy gap [see Fig. 3.1(a) for illustration]. After the intersection point is reached for the first time, the molecular electronic Hamiltonian, which is initially diagonal in the BO approximation, is extended by introducing a further biasing potential V_{ge} into the off-diagonal elements according to

$$\boldsymbol{H_{BO}} = \begin{pmatrix} E_g & 0 \\ 0 & E_e \end{pmatrix} \rightarrow \boldsymbol{H_{meta}} = \begin{pmatrix} E_g & V_{ge} \\ V_{ge} & E_e \end{pmatrix}. \tag{3.3}$$

Subsequently, the metadynamics is continued on a locally modified potential energy surface obtained by diagonalization of the above Hamiltonian which gives rise to a modified PES with the effective energy gap

$$\Delta E_{meta} = \sqrt{(E_g - E_e)^2 + 4V_{ge}^2}. \tag{3.4}$$

The off-diagonal bias V_{ge} serves to locally open the gap between the eigenstates of the modified Hamiltonian. The metadynamics then drives the system to the next intersection point. In order to prevent the return to the previously sampled regions of the CI seam, the V_{ge} is made dependent on a collective variable s_{CI}, which should be capable of distinguishing different molecular configurations and is updated only if the energy gap ΔE_{meta} is below ϵ according to

$$\begin{aligned} V_{ge}(t) = \sum_{t'=\tau_G,2\tau_G,\ldots}^{t} & w \exp\left\{ -\frac{[s_{CI}(t) - s_{CI}(t')]^2}{2\delta s^2} \right\} \\ & \times \Theta(\epsilon - \Delta E_{meta}(t')). \end{aligned} \tag{3.5}$$

One possible choice of s_{CI} is to use the distance matrix of a molecule, which is unique but inconvenient because of its high dimensionality and symmetry ambiguities. A better choice is to use its scalar invariants such as its lowest eigenvalue, or various topological indices.[150] As a CV for the off-diagonal bias s_{CI} in our simulations, we choose the 3D-Wiener number W [151] defined as

$$W = \frac{1}{2} \sum_{i}^{N} \sum_{j}^{N} d_{ij}, \tag{3.6}$$

where N is the number of atoms and d_{ij} are interatomic nonhydrogen distances. Its correlation with molecular shape made it a reliable topographical descriptor in numerous studies where structural unambiguity is important. Since the conical intersection seam is of dimension $f-2$, where f is the number of degrees of freedom, and W is a scalar function of the distances, there is no restriction to any specific

region on the seam. Therefore, the most possible structural variability is achieved and can be further extended by running several trajectories with different initial conditions.

We wish to point out that as long as no Gaussians have been added to the off-diagonal bias V_{ge}, ΔE_{meta} exactly equals the BO gap ΔE_{BO}. This can be derived from Eq. (3.4) and is due to the construction of $\boldsymbol{H_{meta}}$ that reduces to $\boldsymbol{H_{BO}}$ in case of the nonexisting off-diagonal coupling. Since V_{ge} is updated only in the vicinity of the CI seam, this holds true for the complete pathway until the intersection is reached for the first time [see Fig. 3.1(a)]. At this point, the metadynamics potential V_G is already overcompensating the minimum on the ground-state PES where the simulation had been started, resulting in a persistent force toward structures with small ΔE_{meta}. If now a Gaussian bias is added to V_{ge} at the current value of the collective variable s_{CI}, ΔE_{meta} will increase, thus opening again the gap between the two states [see Fig. 3.1(b)]. However, the bias potential V_G disfavors nonzero values of the energy gap, which in turn forces the molecule to change the value of the collective variable s_{CI} such that the intersection seam is reached again [see Fig. 3.1(c)]. In this way, the whole CI seam can be "unzipped", allowing for automatic exploration of its energy landscape. In order to calculate the force in Eq. (3.1), the gradient of the modified energy gap is needed:

$$\nabla\left(\Delta E_{meta}\right) = \frac{\Delta E_{BO}\nabla\left(\Delta E_{BO}\right) + 4V_{ge}\nabla\left(V_{ge}\right)}{\Delta E_{meta}}, \tag{3.7}$$

which requires the calculation of the gradients of the BO energies that can be provided by any suitable electronic structure method, as well as additional differentiation of V_{ge}:

$$\begin{aligned}\nabla\left(V_{ge}\right) = \sum_{t'=\tau_G,2\tau_G,\ldots}^{t} & w\exp\left\{-\frac{\left[s_{CI}(t)-s_{CI}(t')\right]^2}{2\delta s^2}\right\} \\ & \times\Theta(\epsilon-\Delta E_{meta}(t')) \\ & \times\left\{-\frac{s_{CI}(t)-s_{CI}(t')}{\delta s^2}\nabla\left[s_{CI}(t)\right]\right\}.\end{aligned} \tag{3.8}$$

Like the potential V_{ge} itself, it is given by a sum of Gaussians, but each of them is multiplied by an additional factor dependent on the gradient of the collective variable. For the 3D-Wiener number, $\nabla\left[s_{CI}(t)\right]$ is defined by

$$\nabla W = \frac{1}{2}\sum_{i}^{N}\sum_{j}^{N}\nabla d_{ij}. \tag{3.9}$$

The algorithm can be summarized with the following steps:

1. Initialize metadynamics trajectory with effective energy gap ΔE_{meta} as CV and choose an appropriate CV s_{CI} for the off-diagonal bias potential.
2. Integrate the Newtonian equations of motion using a conventional molecular dynamics algorithm. If the actual time step is a multiple of τ_G, proceed with one of the following steps:
   a) If $\Delta E_{meta} > \epsilon$, add new Gaussian to the diagonal metadynamics potential V_G.
   b) If $\Delta E_{meta} < \epsilon$, add new Gaussian to the off-diagonal coupling potential V_{ge} and diagonalize the electronic Hamiltonian to obtain modified PES.
3. Stop the simulation after a defined number of steps.
4. Identify the plateau regions in the CI energy landscape and select structures for MECP optimization.

The use of a threshold ϵ in Eqs. (3.2) and (3.5) for the switch between on- and off-diagonal metadynamics enables the addition of Gaussians to V_{ge} only if the trajectory is close to the CI seam. At the same time, it prevents biasing small values of ΔE_{meta} that would lead back to larger energy gaps again. A reasonable choice for ϵ is to use the same energy that is employed as Gaussian width for the V_{ge}. The Gaussian width and height for the off-diagonal bias should be chosen sufficiently small in order to bias the previously visited configurations as local as possible. Thus, it can be ensured that the system stays in close proximity to the intersection seam most of the simulation time. Unlike conventional metadynamics, the aim of this algorithm is not to converge the metadynamics potential to the free energy surface and the results are therefore less sensitive to the choice of parameters.

Periods of the trajectory with low ΔE_{BO} represent structures close to the intersection seam. It is convenient to apply a local CI optimization method on snapshots from these regions in order to group the resulting MECPs by energy.

3.3. Results and Discussion

In order to illustrate the ability of the multistate metadynamics to sample conical intersections, we choose the furan molecule, which exhibits versatile photochemistry that is still not completely understood and has been a subject of a number of recent experimental and theoretical studies.[152–156] Here, the electronic structure of furan is described in the frame of the ab initio complete active space self-consistent field (CASSCF) method as implemented in the MOLPRO quantum chemical package[157] with an active space of 10 electrons distributed over 9 orbitals together with

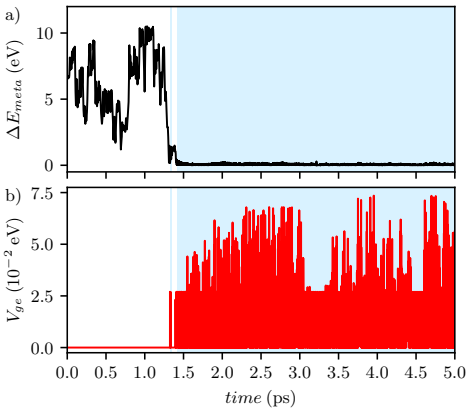

Figure 3.2.: Multistate metadynamics trajectory for furan: (a) The energy gap ΔE_{meta} along the trajectory and (b) the off-diagonal bias potential V_{ge}. Periods in which V_{ge} is updated ($\Delta E_{meta} < \epsilon$) are highlighted in light blue.

the 6-31G* atomic basis set, as in previous quantum-chemical studies.[156] The Newtonian equations of motion in the metadynamics simulations were integrated using the velocity Verlet algorithm[15] with a step size of $0.25\,\mathrm{fs}$ and the temperature was kept constant at $300\,\mathrm{K}$ utilizing the Berendsen thermostat.[23] Multistate metadynamics simulations were run using initial conditions sampled from a 2-ps-long MD trajectory propagated in the electronic ground state. Gaussian bias potentials with a width of $0.5\,\mathrm{eV}$ and a height of $1.0\,\mathrm{eV}$ were added every 100 steps ($25\,\mathrm{fs}$) to the diagonal bias. For the off-diagonal coupling V_{ge}, we apply the 3D-Wiener number (excluding hydrogen atoms) as CV with Gaussians of 0.01 Å width and $0.027\,\mathrm{eV}$ height. The update threshold ϵ was set to $0.5\,\mathrm{eV}$. As can be seen from Fig. 3.2(a), the energy gap decreases during the multistate metadynamics simulation from an initial Franck-Condon value of $6.97\,\mathrm{eV}$ to zero within the first 1.4 ps. At this point, the CI is reached for the first time and the off-diagonal coupling V_{ge} shown in Fig. 3.2(b) is automatically switched on. Together with the previously built-up bias potential V_G, this forces the system to continue exploring the CI energy landscape. The time evolution of the ground- and excited-state PES for three runs with different initial conditions sampled from the ground state trajectory is shown in Fig. 3.3. In each case, the system is initially driven from a local minimum toward the conical intersection, leading to the closure of the energy gap. Subsequently, the dynamics explores the CI landscape and the energy gap remains zero within the predefined numerical threshold. As can be seen from Fig. 3.3, CI energy landscape exhibits several plateaus and depending on the CI character, some of them are separated by relatively large barriers. Low barriers are in general present for transitions between

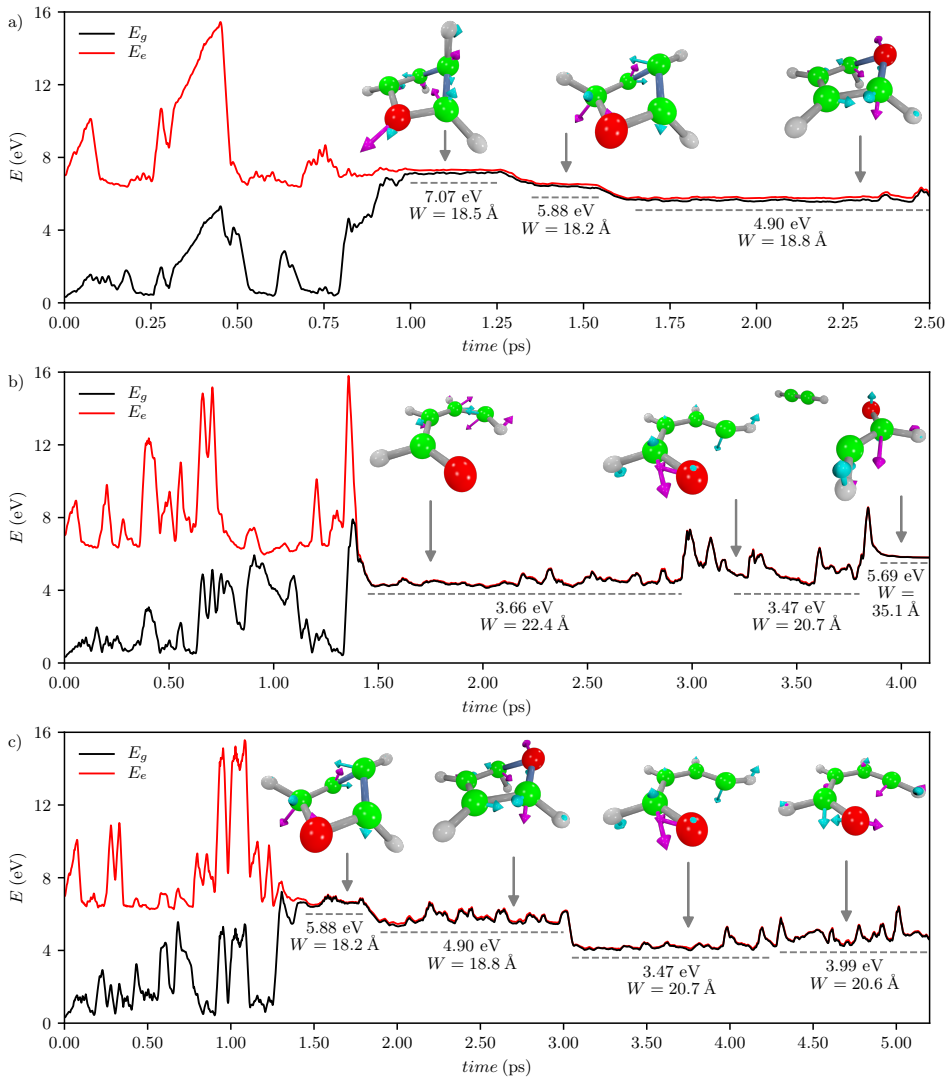

Figure 3.3.: Conical intersection energy landscapes of three different trajectories: Energies of the ground (black) and first excited (red) states along the metadynamics trajectory for furan. A moving average with a window of 25 fs has been applied for better visibility. Upon reaching the CI after 1.0–1.5 ps, the system remains confined to the CI seam and explores basins (dotted plateaus) corresponding to different MECPs. For each plateau, the optimized structures of the MECPs together with their branching space vectors, energies relative to the ground-state minimum (in eV), and values of the 3D-Wiener number are given. (a) Multiple ring puckering, (b) ring opening and fragmentation, and (c) combinations of both types are observed.

various ring-puckering CIs, as is seen in the trajectory depicted in Fig. 3.3(a). On the contrary, the trajectory shown in Fig. 3.3(b) leads to the CI structures exhibiting ring opening as well as fragmentation. Molecular fragmentations are typically found after longer simulation times since they are characterized by large Wiener numbers. It is interesting to note that both molecular geometries that have previously been held responsible for the ultrafast deactivation of furan,[154,156] a ring puckering of the oxygen atom and the low-energetic $C-O$ ring opening, have been identified in successive order in the third trajectory shown in Fig. 3.3(c). The found geometries have been subsequently fully optimized using the Bearpark-Robb local optimization algorithm[80] and their branching plane vectors have been determined (cf. Fig. 3.3).

3.4. Conclusion

In summary, we have developed a multistate extension of the metadynamics with the aim to automatically explore conical intersection seams between BO PES. Biasing metadynamics potentials are introduced as off-diagonal elements into the multistate electronic Hamiltonian and MD simulations are run on modified potential energy surface obtained by diagonalization of the latter, using the energy gap as a collective variable. The method can be easily implemented in the frame of any electronic structure method capable of providing energy gradients and excitation energies. It can be applied to explore photochemical reaction pathways, nonradiative relaxation channels, and photophysics of complex molecular systems. As an illustration, we have performed simulations starting from the ground-state structure of the furan and have demonstrated that the conical intersection landscape can be efficiently mapped, allowing us to systematically identify a large number of minimum energy crossing points that can mediate nonradiative relaxation and photochemical reactivity.

Acknowledgement

Funding by the European Research Council (ERC) Consolidator Grant DYNAMO (Grant No. 646737) is gratefully acknowledged.

4. metaFALCON: A Program Package for Automatic Sampling of Conical Intersection Seams Using Multistate Metadynamics

Reprinted with permission from

J. O. Lindner, K. Sultangaleeva, M. I. S. Röhr, R. Mitrić,
J. Chem. Theor. Comput. **2019**, *15*, 3450–3460.

Abstract

The multistate metadynamics for automatic exploration of conical intersection seams and systematic location of minimum energy crossing points in molecular systems and its implementation into the software package metaFALCON is presented. Based on a locally modified energy gap between two Born-Oppenheimer electronic states as a collective variable, multistate metadynamics trajectories are driven towards an intersection point starting from an arbitrary ground state geometry and are subsequently forced to explore the conical intersection seam landscape. For this purpose, an additional collective variable capable of distinguishing structures within the seam needs to be defined and an additional bias is introduced into the off-diagonal elements of an extended (multistate) electronic Hamiltonian. We demonstrate the performance of the algorithm on the examples of the 1,3-butadiene, benzene and 9H-adenine molecules, where multiple minimum energy crossing points could be systematically located using the Wiener number or Cremer-Pople parameters as collective variables. Finally, on the example of 9H-adenine we show that the multistate metadynamics potential can be used to obtain a global picture of a conical intersection seam. Our method can be straightforwardly connected with any ab initio or semiempirical electronic structure theory that provides energies and gradients of the respective electronic states and can serve for systematic elucidation of the role of conical intersections in the photophysics and photochemistry of complex molecular systems, thus complementing nonadiabatic dynamics simulations.

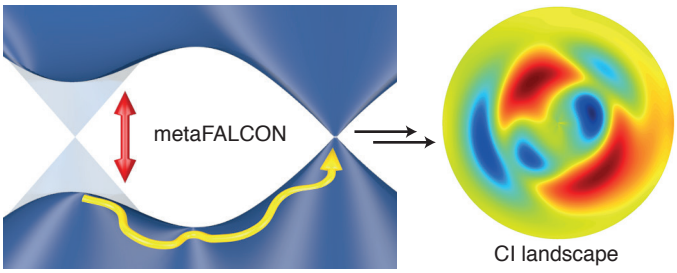

4.1. Introduction

The concept of adiabatic potential energy surfaces (PES), the source of the fundamental concepts of chemistry, is rooted in the Born Oppenheimer (BO) approximation. For the majority of chemical reactions taking place in the ground electronic state, the latter allows for the theoretical treatment of reactivity, the identification of reaction mechanisms as well as the prediction of kinetic parameters.

However, in photochemical processes involving electronically excited states the character of the electronic wavefunction may rapidly change with the nuclear configuration as the reaction proceeds, leading to the complete breakdown of the BO approximation. The change of the character of the electronic wavefunction leads to a large nonadiabatic coupling being responsible for efficient non-radiative transitions between electronic states. These couplings are largest in the vicinity of conical interesections (CIs) between the adiabatic potential energy surfaces.[49–51,158] The role of CIs in photochemistry, photophysics and photobiology is reflected in countless examples, such as vision,[54,72] the photostability of DNA,[136] organic photochemical synthesis[137] as well as the functionality of photovoltaic devices,[73] and a significant effort has been undertaken to identify them experimentally using various spectroscopic techniques.[72,77,78]

Therefore, in order to predict the fait of an electronically excited molecule it is crucial to theoretically characterize structure, energetics and reaction pathways leading to conical intersections. Several strategies have been applied for the optimization of minimum energy crossing points (MECP) based on penalty functions,[82] gradient projection[80] or Lagrange-Newton techniques.[79] All these methods require the knowledge of a reasonable initial guess that can be generated either by chemical intuition or, for example, by running nonadiabatic dynamics simulations. Although even an inaccurate guess may lead to some MECP, it is not clear which role this structure plays in the context of the complete crossing seam. Attempts to characterize the full intersection seam instead of individual geometries have so far relied on symmetry considerations[159] or the use of algorithms such as the nudged elastic band (NEB) method[144] or anharmonic downward distortion following (ADDF).[83,84,142,143] Furthermore, transition states on the intersection seam have been adressed by an analytical second-order description of the intersection seam and used for linking multiple crossing points.[160,161]

In order to drive a molecule from a ground state minimum to the lowest intersection points, the energy has to be raised by several eV, which is in the scope of what can be achieved by accelerated molecular dynamics (MD) techniques. The metadynamics introduced by Parrinello and coworkers[32,33,35,146–148] represents an enhanced sampling approach that is both easy to use and efficient. This recently lead us to introduce a multistate extension of the metadynamics that is suitable for a fully automatic exploration of conical intersection seams.[100] Usually, the main challenge

in applying the metadynamics method is to find suitable collective variables (CV) capable of driving transitions between different basins on the PES. Consequently, much effort has been put in the definition of suitable CVs, that can in principle be as simple as a single bond length but sometimes even require advanced techniques such as machine learning or dimensionality reduction to be generated.[148,149]

In our multistate metadynamics, we use a locally modified energy gap as CV, which is applicable to any molecular system, augmented by an additional geometric CV which drives seam exploration. In this article, we first provide a detailed formulation of the multistate metadynamics and its implementation within our newly developed metaFALCON package. In order to illustrate the method and test its robustness with respect to the choice of the simulation parameters we apply it to the well studied 1,3-butadiene and benzene molecules whose intersection seams have been thoroughly characterized before.[59,86,159,162–166] Finally, we demonstrate on the example of the DNA base 9H-adenine that a full intersection seam can be reconstructed based on the multistate metadynamics.

4.2. Methods

Multistate metadynamics algorithm. The idea of the multistate metadynamics[100] is to use the energy gap between the ground and excited electronic states as a collective variable serving to drive the molecule toward the CI seam starting from an arbitrary ground state structure (e.g. the ground state minimum). The system is propagated using the Newtonian equations of motion augmented by an additional history-dependent bias potential $V_G(t)$, which for the i-th particle read:

$$m_i \ddot{\mathbf{R}}_i = -\nabla_i (E_g + V_G(t)). \tag{4.1}$$

Here, E_g represents the ground state BO PES. The history-dependent bias potential is updated at regular time steps τ_G by adding Gaussian-shaped functions along the energy gap CV defined further below:

$$\begin{aligned} V_G(t) = \sum_{t'=\tau_G, 2\tau_G, \ldots}^{t} & w \exp\left(-\frac{(\Delta E_{meta}(t) - \Delta E_{meta}(t'))^2}{2\delta s^2} \right) \\ & \times \Theta(\Delta E_{meta}(t') - \epsilon), \end{aligned} \tag{4.2}$$

The bias potential is dependent on the modified energy gap ΔE_{meta}, and w and δs represent the fixed height and width, respectively. An important feature of the algorithm is that the bias potential is updated only if the value of the gap is larger than a numerical threshold ϵ. This is enforced by the presence of the Heaviside theta function $\Theta(\Delta E_{meta} - \epsilon)$ in Eq. 4.2.

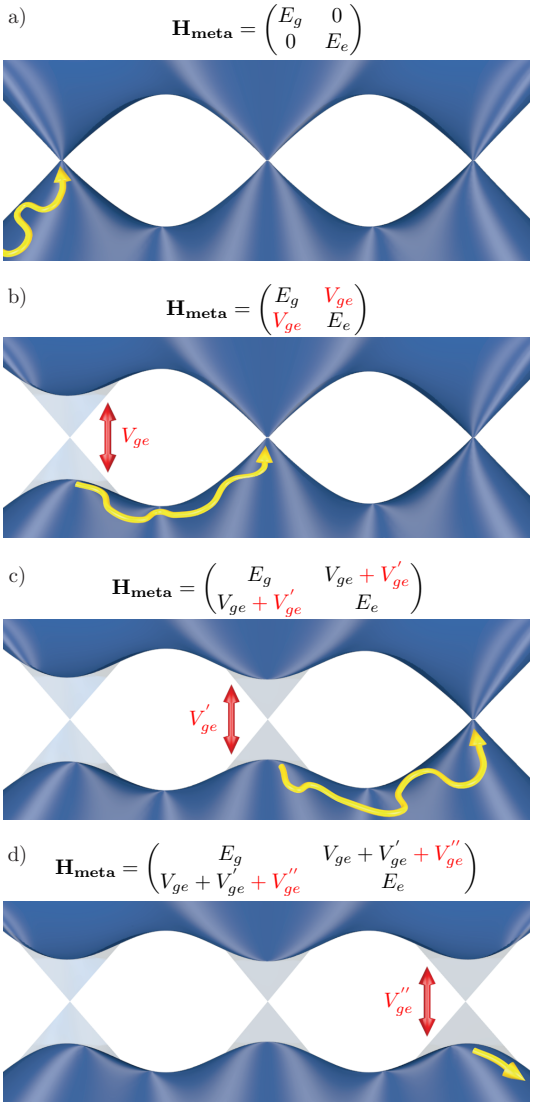

Figure 4.1.: Scheme of the algorithm. (a) The bias potential V_G is constructed in order to drive the system from lower-energy regions on the ground state PES toward the intersection seam (yellow trajectory). (b) Upon reaching the seam, an off-diagonal coupling V_{ge} (red) is added to the electronic Hamiltonian, opening the effective energy gap. The metadynamics subsequently reduces the impact of V_{ge} which leads to the next intersection point. The addition of the further bias potentials V'_{ge} (c) and V''_{ge} (d) enables the complete exploration of the CI seam.

Starting a molecular dynamics simulation e.g. from a minimum on the ground state PES, the bias potential will force the system to move toward the CI seam by systematically lowering the value of the energy gap (see Fig. 4.1a for illustration). Upon reaching the intersection seam for the first time, the molecular electronic Hamiltonian, which is initially diagonal in the BO approximation, is extended by introducing a further biasing potential V_{ge} into the off-diagonal elements according to

$$\mathbf{H_{BO}} = \begin{pmatrix} E_g & 0 \\ 0 & E_e \end{pmatrix} \rightarrow \mathbf{H_{meta}} = \begin{pmatrix} E_g & V_{ge} \\ V_{ge} & E_e \end{pmatrix}. \tag{4.3}$$

This is a crucial element of our algorithm, leading to a local modification of the PES, which is obtained by diagonalization of $\mathbf{H_{meta}}$. The metadynamics continues to run on a such locally modified potential energy surface with the effective energy gap

$$\Delta E_{meta} = \sqrt{(E_g - E_e)^2 + 4V_{ge}^2}. \tag{4.4}$$

The gap between the eigenstates of the modified Hamiltonian is enhanced by the contribution of the off-diagonal bias V_{ge}. Due to the Θ-function in Eq. 4.2, V_G is constructed such that large values of ΔE_{meta} are biased and the metadynamics drives the system to the next intersection point. This requires that V_{ge} is made dependent on an additional collective variable s_{CI}. If the latter is chosen in a way that it is able to distinguish between different molecular configurations, the return to the previously sampled regions of the CI seam is prevented. Complementary to V_G, V_{ge} is updated only if the energy gap ΔE_{meta} is below ϵ by addition of a Gaussian potential according to

$$\begin{aligned} V_{ge}(t) = \sum_{t'=\tau_G, 2\tau_G, \ldots}^{t} & w \exp\left(-\frac{(s_{CI}(t) - s_{CI}(t'))^2}{2\delta s^2}\right) \\ & \times \Theta(\epsilon - \Delta E_{meta}(t')). \end{aligned} \tag{4.5}$$

As illustrated in Fig. 4.1a, ΔE_{meta} exactly equals the BO gap ΔE_{BO} as long as no Gaussians have been added to the off-diagonal bias V_{ge}, since $\mathbf{H_{meta}}$ reduces to $\mathbf{H_{BO}}$. During the starting phase, ΔE_{meta} is by far larger than ϵ, meaning that V_G is periodically updated and drives the system toward the intersection seam. Only when V_G is strong enough to persistently force the system to the vicinity of the CI seam, V_{ge} is updated (see Fig. 4.1b). Diagonalization of $\mathbf{H_{meta}}$ enlarges the effective energy gap and the dynamics is continued on the modified PES. V_{ge} generates a force to change the current value of the collective variable s_{CI}, while V_G pushes the system back to the intersection seam. Upon reaching the next conical intersection, another Gaussian is added to V_{ge} (see Fig. 4.1c), which is specifically adjusted to bias the current CI-structure. This process is repeated (see Fig. 4.1d) until the whole part of the intersection seam accessible by s_{CI} is automatically "unzipped".

Besides the BO energy gradient of the ground state that can be obtained by a whole spectrum of electronic structure methods, the gradient of the modified energy gap is needed in order to calculate the force in Eq. 4.1. The latter can be obtained from the following expression:

$$\nabla\left(\Delta E_{meta}\right) = \frac{\Delta E_{BO}\nabla\left(\Delta E_{BO}\right) + 4V_{ge}\nabla\left(V_{ge}\right)}{\Delta E_{meta}}, \tag{4.6}$$

which additionally requires the calculation of the excited state energy gradient, as well as differentiation of V_{ge} with respect to the coordinates

$$\begin{aligned}\nabla\left(V_{ge}\right) = \sum_{t'=\tau_G,2\tau_G,\ldots}^{t} & w\exp\left(-\frac{\left(s_{CI}(t)-s_{CI}(t')\right)^2}{2\delta s^2}\right) \\ & \times\Theta(\epsilon-\Delta E_{meta}(t')) \\ & \times\left(-\frac{s_{CI}(t)-s_{CI}(t')}{\delta s^2}\nabla\left(s_{CI}(t)\right)\right).\end{aligned} \tag{4.7}$$

The algorithm as implemented in the metaFALCON package is summarized in the flowchart given in Fig. 4.2. It consists of a standard MD code where the forces used for the integration of the Newtonian equations of motion are modified as described above. A key feature of our algorithm is the threshold ϵ in Eq. 4.2 and 4.5 that controls which bias potential is updated in a given metadynamics step. V_{ge} is only updated, when ΔE_{meta} is small so that it acts only if the system is close to the CI seam. The complementary addition of Gaussians to V_G only when ΔE_{meta} is large ensures that there is a force leading into the direction of the intersection seam at all times. We therefore recommend to set ϵ to the same value that is used for the parameter w in Eq. 4.2. Plateau regions in the electronic BO energies then correspond to the CI energy landscape if ΔE_{BO} is low. Sampling from these periods of the dynamics allows for local CI optimization and subsequent classification of the found MECPs by structure and energy.

The choice of the collective variable s_{CI}. For the determination of the metadynamics forces, it is necessary to calculate s_{CI} and its gradient in every dynamics step. Ideally, s_{CI} should be unique for any structure on the intersection seam, which would be the case for example for the entries of the geometrical distance matrix. Unfortunately, an efficient metadynamics sampling of the configuration space is only achieved if the number of CVs is kept low which is definitely not the case for the complete distance matrix. Apart from that, symmetry ambiguities arise from the fact that the atoms have to be in a pre-defined order and commutation leads to a new matrix although the overall molecular shape is preserved. For these reasons, a better choice is to use scalar invariants like its lowest eigenvalue or other topological

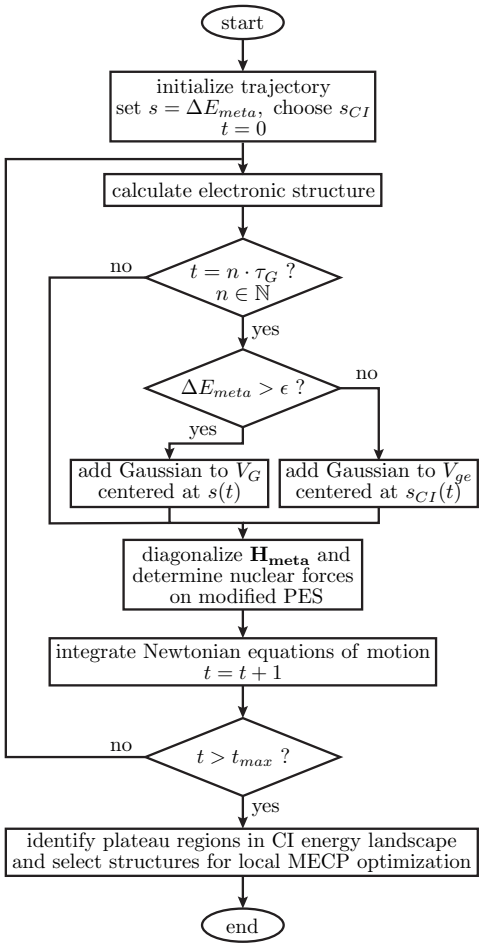

Figure 4.2.: Algorithm flowchart of the multistate metadynamics. After choosing an appropriate CV for the off-diagonal bias potential, a conventional molecular dynamics algorithm is used for integrating the Newtonian equations of motion on the PES modified by V_G. Finally, local MECP optimizations are carried out for the characterization of the CI landscape.

indices.[150] As a most general approach in our simulations, we choose the 3D-Wiener number W[151] defined as

$$W = \frac{1}{2}\sum_{i}^{N}\sum_{j}^{N} d_{ij}, \tag{4.8}$$

as a CV for the off-diagonal bias s_{CI}, where N is the number of atoms and d_{ij} are interatomic distances. It is convenient to consider only non-hydrogen distances, but we also examine the Wiener number including distances from and to hydrogen atoms, which we denote W^H. W correlates with the molecular shape and therefore enables the efficient sampling of a large variety of different configurations for a given system. Due to the reduction of dimensionality, there is no unique mapping of the Wiener number to the structure, meaning that $f-3$-dimensional isosurfaces are biased rather than single configurations on the $f-2$-dimensional CI seam, where f is the number of internal degrees of freedom. However, this problem can be adressed by running several trajectories with different initial conditions, leading to the largest possible structural variability.

The gradient of the collective variable, $\nabla\left(s_{CI}(t)\right)$, is needed for the evaluation of $\nabla\left(V_{ge}\right)$ according to Eq. 4.7 and for the 3D-Wiener number reads

$$\nabla W = \frac{1}{2}\sum_{i}^{N}\sum_{j}^{N} \nabla d_{ij}. \tag{4.9}$$

In aromatic and heteroaromatic organic molecules, many structures corresponding to conical intersections involve the displacement of atoms out of the ideal ring plane (ring puckering). We have already shown for the furan molecule[100] that it is possible to find some of these structures by the use of the Wiener number. However, distinction between different puckering motifs can only be achieved if a suitable collective variable is employed that is able to characterize the exact type of structural deformation. Therefore, we have chosen the systematics of Cremer-Pople ring puckering parameters which allow for the full description of puckering in six-membered rings with only three coordinates.[102] For a detailed description of the definition of Cremer-Pople parameters and the corresponding gradients see appendix B.

4.3. Computational Details

The multistate metadynamics simulations on 1,3-butadiene and benzene have been performed by using the ab initio complete active space self-consistent field (CASSCF) method as implemented in the Molpro 2012 program package.[157] The active space comprised all π-orbitals with the respective number of electrons, i.e. (4, 4) for butadiene and (6, 6) for benzene, and state-averaging has been applied for

the lowest two singlet states. We have used the 4-31G basis set[167] on butadiene and the 6-31G* basis set[127] on benzene. For the 9H-adenine molecule, we employed the semiempirical OM2 Hamiltonian combined with the GUGA MR-CI approach,[168,169] taking into account all single and double excitations of the four most important reference configurations. The computational parameters were chosen in order to ensure comparability with previous results from the literature.[46,159,162]

In order to perform multistate metadynamics, ten initial conditions were generated for each of the molecules by sampling over $2\,\mathrm{ps}$ trajectories propagated in the electronic ground state. The Newtonian equations of motion were integrated using the velocity Verlet algorithm[15] with a time step of $0.25\,\mathrm{fs}$ (butadiene and benzene) and $0.1\,\mathrm{fs}$ (adenine). Temperature was kept constant at $300\,\mathrm{K}$ using the Berendsen thermostat.[23] The parameters for multistate metadynamics were chosen such that the intersection seam is reached within short simulation times. Correspondingly, Gaussians with a width of $0.5\,\mathrm{eV}$ and a height of $1.0\,\mathrm{eV}$ were added to V_G, while τ_G was set to 100 time steps ($25\,\mathrm{fs}$). In the case of adenine, smoother sampling was achieved by adding Gaussians with a height of only $0.2\,\mathrm{eV}$ in intervals of 250 time steps. According to the chosen δs, the threshold ϵ for the Θ-functions in Eqs. 4.2 and 4.5 was also set to $0.5\,\mathrm{eV}$. The shape of the Gaussians added to V_{ge} has been adjusted to the respective CVs and is discussed in detail in section 4.4.1.

4.4. Results and Discussion

4.4.1. 1,3-Butadiene

As a first example we apply our method to explore the conical intersection seam in 1,3-butadiene. In the past decades, the role of conical intersections in the photochemistry of butadiene has been extensively studied as a model for conjugated π-systems and photoisomerizations.[162–164] The multistate metadynamics trajectory has been started from the ground state equilibrium structure with the Franck-Condon excitation energy of $6.65\,\mathrm{eV}$. The insertion of several Gaussians to the bias potential already induces oscillations in ΔE_{meta} between $4\,\mathrm{eV}$ and $10\,\mathrm{eV}$. The pathway from the ground state minimum structure to the intersection seam is represented by the time evolution of the energy gap ΔE_{meta}, depicted in Fig. 4.3a. Since V_{ge} is zero in the displayed time range, ΔE_{meta} equals ΔE_{BO}. As can be seen, the energy gap decreases within 600 fs from $6.65\,\mathrm{eV}$ to zero, which reflects the fact that the trajectory reaches the intersection point between the ground and excited state for the first time.

The shape of the metadynamics potential V_G is depicted in Fig. 4.3b in steps of five Gaussians ($0.125\,\mathrm{ps}$). Within the first $0.5\,\mathrm{ps}$, V_G is only slightly extended to the lower values of the gap. However, after 25 Gaussians have been added to V_G ($0.625\,\mathrm{ps}$), the induced forces are strong enough to let ΔE_{meta} become smaller than the threshold

ϵ. Consequently, the Θ-function in Eq. 4.2 stops the addition of further Gaussians and the potential V_G does not change as long as the system stays in the vicinity of the intersection seam.

The efficiency of the CI seam exploration is dependent on the chosen collective variable s_{CI} to build up V_{ge} and the respective parameters for the Gaussian shape. The CV, on the one hand, can be essentially one of two types, either specific to a given problem or of most possible general nature. The form of the Gaussians, on the other hand, requires the critical choice of δs and w in a way that the simulation time can be kept low with a maximum number of found MECP structures. In order to test the sensitivity of the method with respect to the choice of the Gaussian parameters we have run simulations with different values of δs and w. Since the role of conical intersections between ground and excited states of butadiene has first been discussed in 1993,[162] more than 30 different MECP structures have been reported for this small molecule.[86] Most importantly, s-*transoid* and s-*cisoid* structures have been described, differing in their rotation angles around the central $\mathrm{C}-\mathrm{C}$ bond. We therefore concentrate on these two MECPs by setting s_{CI} to the torsion angle ϕ defined by the four carbon atoms.

A comparison of differently shaped Gaussians added to V_{ge} when ΔE_{BO} reaches zero for the first time is provided in Fig. 4.4. In all of the four distinct combinations of w and δs, the trajectory follows the same pathway until the addition of the first Gaussian to V_{ge} at $0.65\,\mathrm{ps}$. When Gaussian heights are of the same order of magnitude as ΔE_{BO} and large values for the width δs are used, the algorithm can be nicely tracked step by step (see Fig. 4.4a). After the first occurrence of a non-zero V_{ge}, the forces resulting from V_G provoke a reduction of the latter which is related to a changing torsion angle ϕ. This process is completed at $0.67\,\mathrm{ps}$, right before the addition of the second Gaussian. If the system returns to a point that has been biased before, V_{ge} increases again, as is seen around $0.69\,\mathrm{ps}$. However, these parameters correspond to a relatively coarse-grained intersection seam following, since permanently high values of V_{ge} support the increase of ΔE_{BO}, meaning that the trajectory is allowed to temporarily sheer off from the intersection seam. Therefore, it is desirable to reduce both parameters to a minimum in order to stay in closest vicinity to the crossing region. If only the width is decreased (see Fig. 4.4b), the result is an off-diagonal potential V_{ge} composed from very narrow Gaussians with large derivatives close to their maxima, leading to an overshooting of the metadynamics forces. If instead only the height is decreased (see Fig. 4.4c), the system stays on the plateau-like top of the Gaussians for long times, because the acting force is negligible. The best performance is therefore achieved by choosing small values of w and δs simultaneously (see Fig. 4.4d). In the present paper, we use values of 0.1° for δs and $0.027\,\mathrm{eV}$ for w.

In general, V_{ge} is less sensitive to the choice of δs and w than V_G in conventional metadynamics, if the multistate metadynamics is only used to localize as many

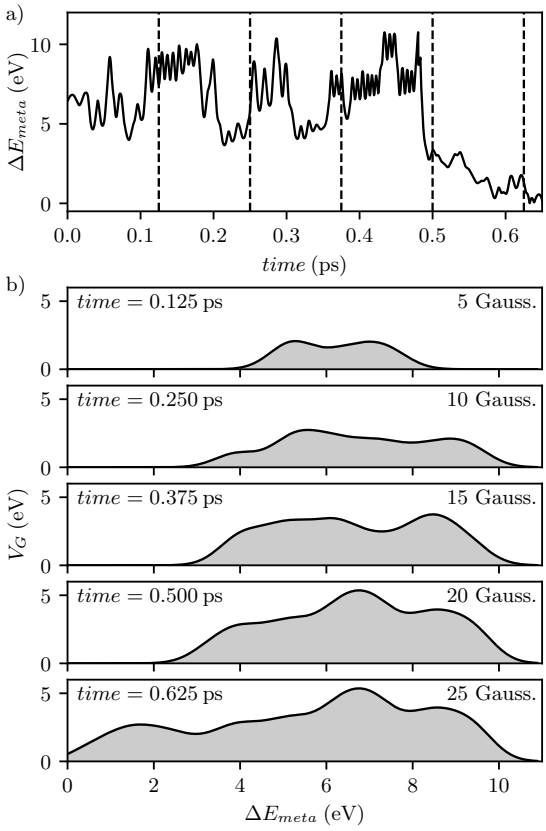

Figure 4.3.: a) Energy gap ΔE_{meta} over time until the intersection seam is reached for the first time. b) Metadynamics potential V_G dependent on the collective variable ΔE_{meta} at time steps symbolized by the dashed lines in a). The time steps are chosen corresponding to multiples of 5 Gaussians added to V_G.

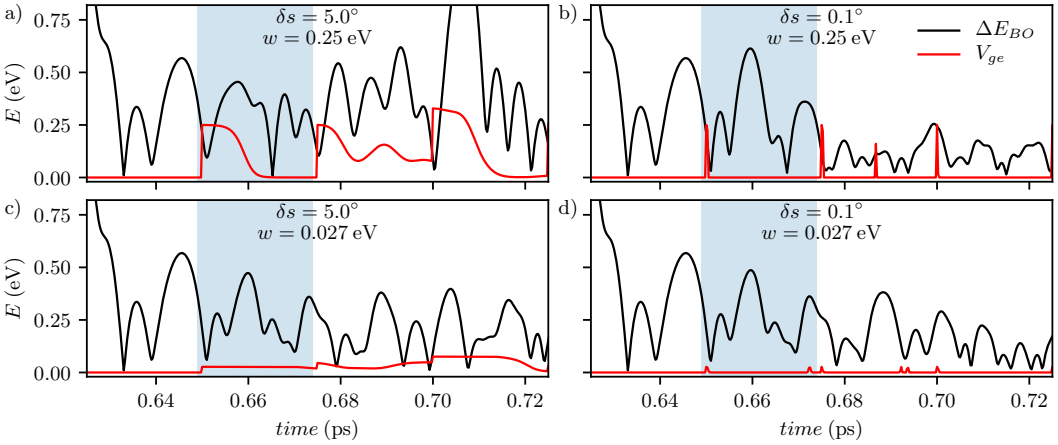

Figure 4.4.: Comparison of trajectories with different Gaussian shapes in V_{ge} for butadiene employing the torsion angle ϕ as the CV. The Born Oppenheimer energy gap ΔE_{BO} (black) and the off-diagonal coupling V_{ge} (red) are given for a) broad δs and high w, b) broad δs and low w, c) narrow δs and high w and d) narrow δs and low w. The 25 fs of relaxation subsequent to the insertion of the first Gaussian are highlighted in light blue.

CI structures as possible. However, if the aim is to achieve convergence to an intersection seam hypersurface as described in section 4.4.3, the guidelines known from the traditional metadynamics apply.[170]

As has been pointed out before, ϕ is the most natural choice of s for the representation of the well-characterized s-*cisoid* and s-*transoid* MECP structures of butadiene. The ground and excited state energies of an exemplary trajectory using this CV are depicted in Fig. 4.5a. The overall shape of E_g and E_e over time follows the energies of sampled snapshot geometries that are obtained by local optimization using the Bearpark-Robb optimization scheme for MECPs.[80] When the intersection seam is reached after the first $1.2\,\mathrm{ps}$ of the simulation, ϕ (see Fig. 4.5b) already takes values close to the torsion angle of $65.5°$ that is obtained in optimized structures of the s-*cisoid* MECP ($5.34\,\mathrm{eV}$) and oscillates around this angle for the next $2\,\mathrm{ps}$. However, in the regions where ϕ takes larger values, optimization of snapshots converge to a local minimum with similar structure compared to the lowest s-*cisoid* structure with a relative energy of $5.43\,\mathrm{eV}$ and $\phi = 69.9$. At $3.3\,\mathrm{ps}$, another plateau is reached at lower energy, associated to the optimized s-*transoid* structure with a torsion angle of $115.8°$ and a relative energy of $5.04\,\mathrm{eV}$.

The drawback of using a specialized CV like the torsion angle for butadiene is that it requires some preliminary knowledge on the character of existing CI-structures.

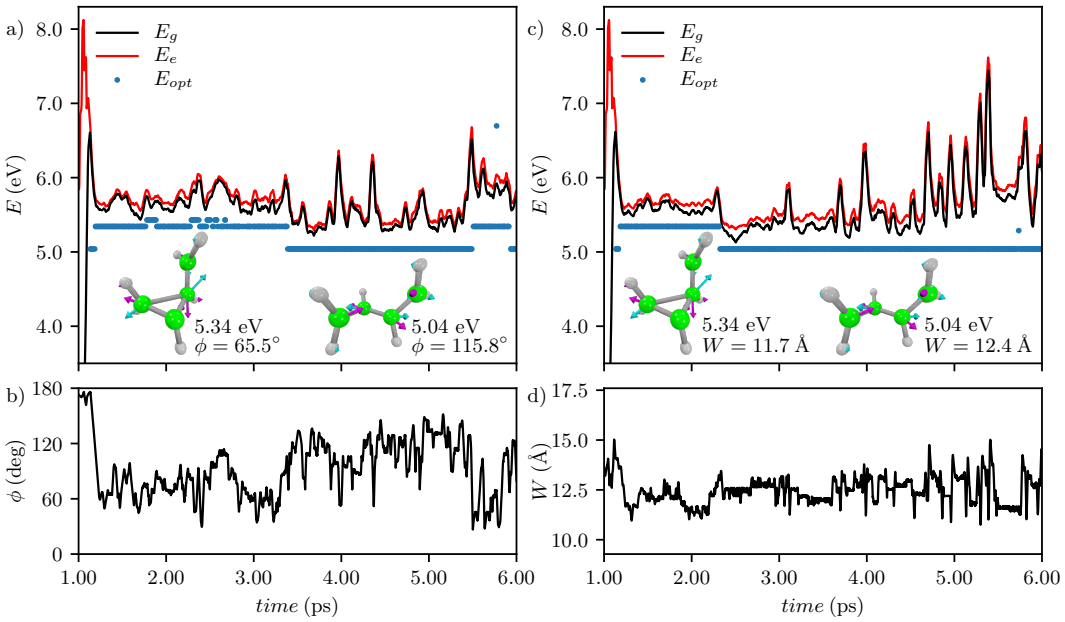

Figure 4.5.: a) Ground and excited state energies, as well as energies of optimized snapshots for an example trajectory of 1,3-butadiene using the torsion angle ϕ as CV. The insets show the most important optimized MECP structures together with their gradient difference and non-adiabatic coupling vectors plotted as arrows. The corresponding CV ϕ is depicted in b). c) Ground and excited state energies, as well as energies of optimized snapshots for an example trajectory of 1,3-butadiene with the same initial conditions as in a) but using the Wiener number W as CV. Again, the insets show the most important optimized MECP structures and in d) the corresponding CV W is depicted.

For this reason, we have already shown for the furan molecule that the 3D Wiener number W is a suitable choice of a generalized CV for multistate metadynamics.[100] Here, we prove that W is also appropriate for butadiene by comparison with the results obtained using the torsion angle. We used a Gaussian width δs of $0.1\,\text{Å}$ and w was set to $0.027\,\text{eV}$ as in the previous example.

In the trajectory given in Fig. 4.5c, most of the optimized structures found are the same as in Fig. 4.5a. The energy pathway in the beginning after closing the gap ΔE_{meta} is equal to the torsion angle CV, since the forces resulting from V_G need some time to manipulate the dynamics. Hence, the structure in this time range is of s-*cisoid* character, leading to a Wiener number of $11.7\,\text{Å}$ upon MECP optimization of dynamics snapshots. Then, with much shorter time delay compared to the usage of the torsion angle, the transition to the s-*transoid* structure is observed. The latter exhibits a Wiener number of $12.4\,\text{Å}$ and can therefore reduce the off-diagonal coupling acting as a bias for low W at that time. It is worth to note that in contrast to the application of the torsion angle as CV, the trajectory does not return to the s-*cisoid* structure within the given time range. The reason for that is that values for W are not unique with respect to different structures. From $5\,\text{ps}$ onwards, the Wiener number repeatedly gets similar to that of the s-*cisoid* structure although the overall character is still s-*transoid*. As a consequence, there is no force that induces a change back to the original torsion angle.

4.4.2. Benzene

In this section we discuss multistate metadynamics simulations on benzene, which serves as a representative of the class of aromatic molecules. It exhibits a large number of MECPs between the electronic ground and excited states,[159] of which a half-boat shaped ring-puckering structure is the best known one.[59]

Interestingly, a number of differing MECP structures have been reported with similar geometrical arrangement of the carbon atoms, i.e. the positions of hydrogen atoms are crucial to distinguish between them.[159] Especially ring-puckering structures are typically found in the low-energy regions of the intersection seam. For this purpose, we tested the use of the Wiener number W^H including all distances to hydrogen atoms and compared the results to these obtained with the Wiener number W excluding hydrogens. Selected optimized structures and their corresponding W and W^H values are presented in Fig. 4.6. In the metadynamics simulations we used values of $0.027\,\text{eV}$ and $0.01\,\text{Å}$ for the w and δs parameters, respectively. In order to account for the larger changes in the values of W^H compared to W, δs was increased to $0.05\,\text{Å}$, when hydrogen atoms were taken into account. The simulations show that both collective variables are appropriate for the efficient localization of the low-energetic and most important ring-puckering structures at $5.49\,\text{eV}$ and $5.76\,\text{eV}$. In most trajectories, the intersection seam is first reached close to the

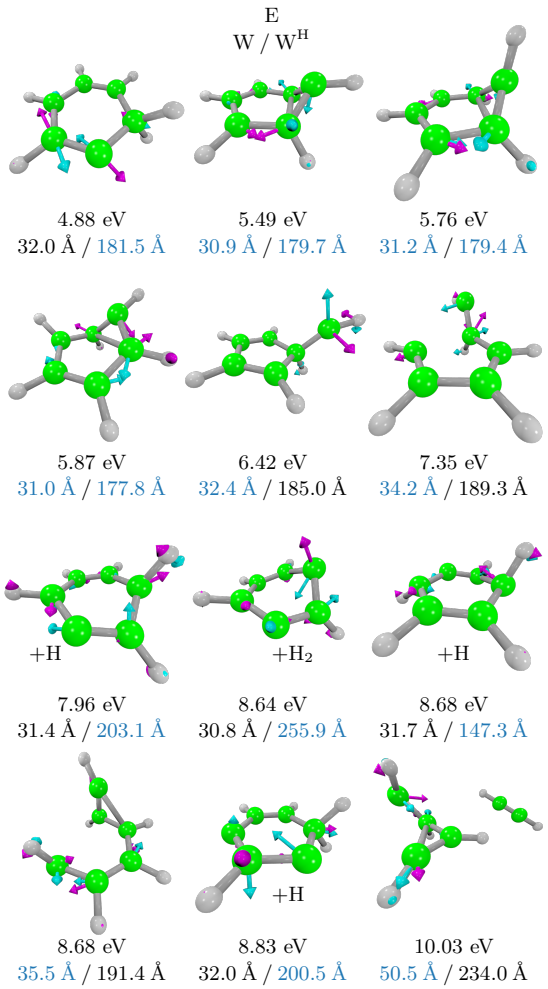

Figure 4.6.: Optimized MECP structures of benzene obtained with multistate metadynamics followed by local MECP optimization. The gradient difference and non-adiabatic coupling vectors are displayed as arrows. Energies are given relative to the optimized ground state structure and the Wiener number is provided by calculation with and without consideration of hydrogen atoms. Numbers highlighted in blue mean that the structure has been obtained by application of the respective CV.

higher energy structure and after a short time, relaxation to the lower-energetic one with the hydrogen atom in equatorial position takes place. A similar structure with reduced symmetry is found at $5.87\,\mathrm{eV}$ in some trajectories. Since the Wiener number has a natural lower bound, long simulation times usually lead to increasing values. Therefore, compared to W^H the use of W excluding hydrogens tends to favor geometrical rearrangements and fragmentations of the carbon scaffold at longer times. In the example of benzene, 5-membered ring structures and ring-openings are found in the range above $6.42\,\mathrm{eV}$. Another frequently observed channel leading to the damage of benzene is the dissociation of an acetylene unit.

Since the Wiener number is defined as the sum over all interatomic distances, its value is larger the more atoms are included. Furthermore, non-bonding $\mathrm{H-H}$ and $\mathrm{C-H}$ distances are generally larger than $\mathrm{C-C}$ distances, since hydrogen atoms are located at the outside of the benzene ring. For this reason, the impact of $\mathrm{C-C}$ distances on changes in W^H is generally lower than for distances including hydrogen atoms. Forces to change the Wiener number may therefore lead to irreversibly large displacements of hydrogen atoms, while more subtle changes in the geometry can be overlooked. The ensemble of higher-energetic MECP structures obtained with the hydrogen-including W^H hence contains mainly modifications of ring-puckering structures with dissociated hydrogen atoms. However, the application of W^H also enabled the characterization of a planar ring structure (see first structure in Fig. 4.6) generated by hydrogen transfer of two neighboring carbon atoms that, interestingly, lies more than $0.6\,\mathrm{eV}$ below the equatorial ring-puckering (see second structure in Fig. 4.6).

4.4.3. 9H-Adenine

The previous sections have demonstrated that the outcome of the multistate metadynamics is mainly dependent on which collective variable is employed. The metadynamics method, however, also allows one to use multiple CVs, if the Gaussian functions in Eq. 4.2 are replaced by products of Gaussians with different s_{CI}. If a set of CVs is defined such that it approximately spans the branching plane perpendicular to the intersection seam, the negative multistate metadynamics potential can be used to reconstruct the intersection seam hypersurface just like standard metadynamics yields the free energy surface. This will be illustrated here on the example of 9H-adenine. It is worth noting that nonradiative decay upon photoexcitation does not need to proceed through a MECP but can also be probable from higher energy regions, depending on the magnitude and direction of nuclear velocities. Since the obtained hypersurface is spanned over the complete CV space, it is a more general representation of the CI seam than methods which rely only on MECP optimization and connecting pathways. DNA nucleobases are a paramount example of molecules whose deactivation processes proceed through conical in-

tersections, which prohibits their damage upon UV-excitation.[136] The key MECPs found in these molecules are characterized by heteroaromatic ring-puckering structures. For example, in the case of adenine, a great number of ring-puckering MECPs has been found and characterized,[171] most of them lying more than $5\,\mathrm{eV}$ above the ground state minimum. However, deformation of the six-membered pyrimidine ring system leads to the four low-energetic MECPs **1**-**4**,[172] with the NH_2-group or the H-atom arranged nearly $90°$ with respect to the ring plane, respectively (cf. Fig. 4.7a). Such ring-puckering structures can be characterized and distinguished by the Cremer-Pople parameters[102] that allow the precise characterization of six-membered rings with only three variables. Besides an amplitude Q, two angles ϕ and θ are calculated from the displacement of the ring atoms out of the plane, as described in detail in the Appendix B. Their large flexibility paired with structural unambiguity makes Cremer-Pople parameters the perfect CVs for investigating the conical intersection seam of cyclic structures such as adenine. Such multiple CVs for the construction of V_{ge} in multistate metadynamics can be implemented analogously as in conventional metadynamics. Here, we use the multistate metadynamics with Q, ϕ and θ as CVs aiming to obtain a complete picture of the intersection seam in adenine with respect to ring-puckerings in the pyrimidine unit.

The exemplary multistate metadynamics trajectory for adenine shown in Fig. 4.8 leads to the formation of three out of four expected CI structures. As can be seen, starting from the ground state structure, after $1.5\,\mathrm{ps}$, ΔE_{meta} drops close to zero and the intersection seam is reached through a NH_2-puckered structure that can be assigned to structure **2** in Fig. 4.7a. Shortly afterwards, the gap increases again, but the trajectory returns to the intersection seam and stays on the higher-lying plateau corresponding to the structure **3** for $0.7\,\mathrm{ps}$. Finally, the energy is decreased again, leading to structure **1** which is similar to **3**.

A pitfall of using Cremer-Pople parameters as CVs again are dissociation events of hydrogen atoms that can occur during the simulation. Since ring-puckering is coupled to large values of Q, reducing the amplitude provides an escape pathway from the already built up bias potential V_{ge}. Low values of Q however correspond to a flattening of the ring structure that usually would cause an increase of ΔE_{meta}. The dissociation of a hydrogen atom is the most probable pathway in such a situation, since this leads to a decreasing energy gap also for a planar ring structure. Despite the fact that ultrafast hydrogen abstractions are physically meaningful pathways,[172] they cause an irreversible structure damage. For that reason, it is unfortunately not possible to drive a single trajectory until the convergence of the metadynamics potential because the failure of the semiempirical SCF calculation forces the simulation run to stop whenever a dissociation event occurs. Therefore, we ran multiple trajectories with different initial conditions and, inspired by multiple walkers metadynamics,[146] summed up the individually obtained V_{ge} potentials to a single potential V'_{ge}. The number of trajectories has been gradually increased until the approximate

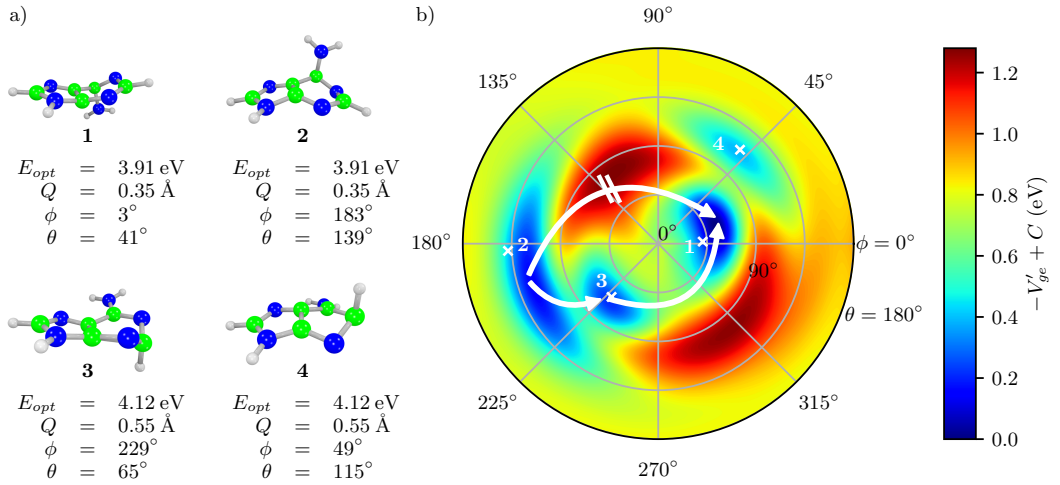

Figure 4.7.: a) Literature-known optimized MECP structures of adenine **1** to **4** together with their energies referenced to the ground state equilibrium and Cremer-Pople parameters. b) Relative intersection seam hypersurface obtained with multistate metadynamics using Cremer-Pople parameters as CVs. The MECPs are marked with white crosses and the white arrows symbolize MECP-connecting pathways on the surface. Energies have been shifted by a constant C such that the lowest MECP **1** lies at 0 eV.

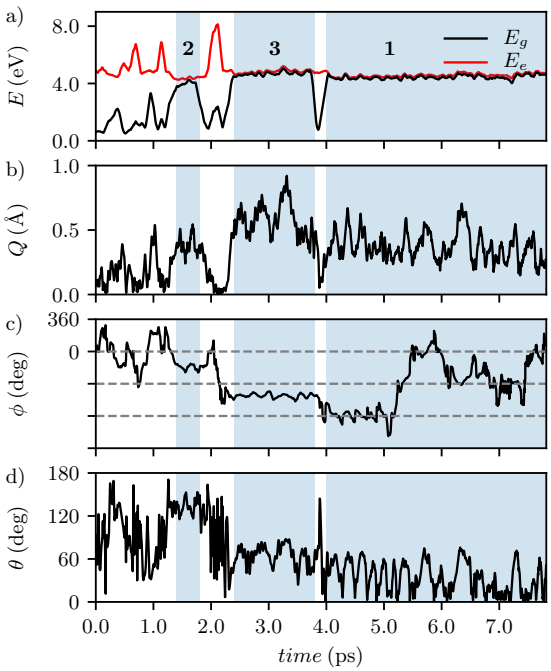

Figure 4.8.: Example trajectory of multistate metadynamics of adenine. Besides the a) ground and excited state energies along the trajectory, b) the amplitude Q, c) the angle ϕ and d) the angle θ are depicted. The bold numbers in a) correspond to the structure character in the surrounding blue-highlighted time ranges. Note that ϕ is periodic in the range from $0°$ to $360°$ which is illustrated by horizontal dashed lines in c).

convergence of V'_{ge} was achieved. Since Q is only the amplitude of the puckering processes and does not include information on the type of puckering, it was integrated out of the potential in the range from $0.13\,\text{Å}$ to $1.06\,\text{Å}$ for the sake of visualization. The resulting total potential from 20 trajectories depends only on ϕ and θ. It exhibits four maxima that can be assigned to the minimum energy crossing points **1**-**4** on the intersection seam hypersurface which is depicted in Fig. 4.7b as $-V'_{ge}$ shifted by a constant C. As expected, the NH_2-puckered structures are found to be more stable than the H-puckered ones. An average difference of $0.24\,\text{eV}$ is obtained from the multistate metadynamics simulation which nicely resembles the energy difference of $0.22\,\text{eV}$ between optimized **1**/**2** and **3**/**4** structures. The pathway that is followed by the trajectory in Fig. 4.8 can also be explained by the obtained intersection seam hypersurface. The direct conversion from **2** to **1** is extremely unfavorable (crossed white arrow in Fig. 4.7b) due to the high barrier $>1\,\text{eV}$. The two-step pathway observed in the example trajectory (consecutive white arrows), on the other hand, only requires the crossing of two relatively low barriers from **2** to **3** ($0.36\,\text{eV}$) and from **3** to **1** ($0.47\,\text{eV}$).

4.5. Conclusion

A multistate metadynamics algorithm has been developed and implemented into the metaFALCON program package allowing for automatic exploration of conical intersection seams between adiabatic Born Oppenheimer potential energy surfaces. In order to confine the MD simulation to the CI seam, the multistate electronic Hamiltonian is extended by introducing Gaussian-shaped off-diagonal bias potentials. By diagonalization of such an extended electronic Hamiltonian and introduction of the energy gap between two states as a collective variable, a modified PES is obtained that can be used to run molecular dynamics within the CI seam. The algorithm can be straightforwardly combined with any ab initio or semi-empirical electronic structure method that can provide ground and excited state energies and their gradients.

As an illustration, multistate metadynamics has been applied to explore the CI seams in 1,3-butadiene, benzene and 9H-adenine, and the influence of the simulation parameters on the seam exploration has been systematically investigated. Starting from the ground-state minimum structures, we have performed simulations that show that the intersection seam in all three systems can be efficiently reached. Special attention has been paid to the choice of parameters that define the shape of the Gaussians contributing to the bias potential that is included in the multistate electronic Hamiltonian. Furthermore, the problem of finding the correct collective variable that drives the seam exploration has been addressed on the example of 1,3-butadiene. The use of the Wiener number has proven to successfully provide a

reliable map of the conical intersection landscape. The impact of including hydrogen atoms into the calculation of the Wiener number has also been evaluated on the example of the benzene molecule. Both variants allowed us to systematically identify a large number of minimum energy crossing points, so we recommend using the Wiener number excluding hydrogen atoms as the most general starting point for any system. However, depending on the investigated system, a more specialized collective variable may be more appropriate in order to find all crossing points that may be relevant for understanding photochemical reaction pathways and nonradiative relaxation channels in complex molecular systems. Finally, on the example of 9H-adenine we have demonstrated that multistate metadynamics can be used to obtain a global representation of the CI seam by converging the multistate metadynamics potential to a stable energy hypersurface. The developed methodology has been implemented into the program package metaFALCON that is publicly available free of charge (http://metafalcon.chemie.uni-wuerzburg.de/).

Acknowledgement

J.O.L. and R.M. are grateful to the Deutsche Forschungsgemeinschaft (DFG) for financial support through GRK2112: "Molecular Biradicals: Structure, Properties and Reactivity". M.I.S.R. and R.M. acknowledge funding from the European Research Council (ERC) Consolidator Grant DYNAMO (Grant No. 646737).

5. Metadynamics for Automatic Sampling of Quantum Property Manifolds: Exploration of Molecular Biradicality Landscapes

Reproduced from

J. O. Lindner, M. I. S. Röhr,
Phys. Chem. Chem. Phys. **2019**, Accepted Manuscript, DOI: 10.1039/C9CP05182A

Abstract

We present a general extension of the metadynamics allowing for an automatic sampling of quantum property manifolds (ASQPM) giving rise to functional landscapes that are analogous to the potential energy surfaces in the frame of the Born-Oppenheimer approximation. For this purpose, we employ generalized electronic collective variables to carry out biased molecular dynamics simulations in the framework of quantum chemical methods that explore the desired property manifold. We illustrate our method on the example of the "biradicality landscapes", which we explore by introducing the natural orbital occupation numbers (NOONs) as the electronic collective variable driving the dynamics. We demonstrate the applicability of the method on the simulation of *p*-xylylene and [8]annulene allowing to automatically extract the biradical geometries. In the case of [8]annulene the ASQPM metadynamics leads to the prediction of biradical scaffolds that can be stabilized by a suitable chemical substitution, leading to the design of novel functional molecules exhibiting biradical functionality.

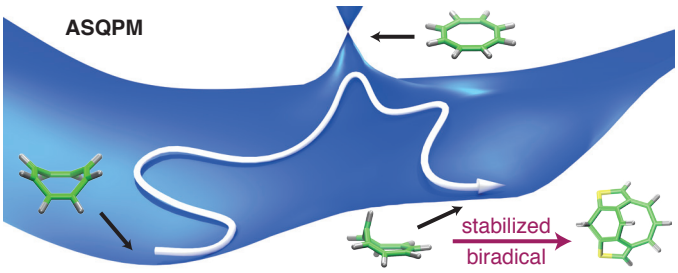

5.1. Introduction

Molecular functionality can often be assigned to a given property of the electronic wavefunction, e.g., the strength of the transition dipole moment determines the efficiency in light-harvesting processes,[173] while in catalytic processes, properties such as the charge distribution and spin-density define the intrinsic activity of the catalysts as well as their reaction route.[174–176] Since the electronic wavefunction exhibits a direct dependence on the nuclear coordinates of the molecule, its characteristics are directly dependent on the structural evolution of the system. Therefore, within the framework of the Born-Oppenheimer (BO) approximation,[4] these properties can be represented as "functional landscapes", in analogy to the concept of potential energy surfaces (PES). The theoretical investigation of these multidimensional hypersurfaces enables a systematic exploration of the structure-function relationship in molecules, allowing to obtain information about their stability and thus to ascertain the structural and energetic accessibility of desired functions in molecules and functional conformations. A molecular functionality of particular interest consists in the biradical character.[88] Several light-induced processes in molecules take place upon transient population of biradical conformations, e. g. at crossing points of the first excited and the ground BO states, where strong nonadiabatic coupling leads to efficient non-radiative decay of excited molecules.[54] Also several bond forming reactions take place via biradical intermediates, such as photoinduced cycloaddition reactions.[177] The introduction of protecting groups allows to stabilize these highly reactive compounds, giving rise to new classes of functional molecules with several potential applications: Organic biradical molecules serve as attractive candidates for optoelectronic applications such as singlet fission.[178–180] Successful strategies for the realization of new organic biradicals consist in consideration of quinoidal compounds and to produce their open-shell resonance structure upon substitution, following the ideas of i) strengthening the π electron conjugation and thus aromatic structure or ii) biasing the biradical configuration by introduction of a steric strain.[181] Also inorganic biradicals can be stabilized upon introduction of protecting ligands. Only recently, a biradical complex bearing a twisted boron-boron double bond stabilized by the introduction of bulky cyclic (alkyl)(amino)carbene (CAAC) ligands has been presented.[182]

Therefore, development of theoretical methods that allow for systematic generation of new biradical molecular scaffolds is highly desired. Accompanied with the development of strategies for the energetic stabilization of the generated biradicals this would enable systematic prediction of new molecules with desired biradical-based functionality.

In this contribution we wish to present a new methodology for an "automatic sampling of quantum property manifolds" (ASQPM) which allows to theoretically investigate the functional landscape of molecules with a given chemical compo-

sition. Therefore, based on the idea of Parrinello's metadynamics[32,33,35,146–148] we have developed a multistate extension of the latter by introduction of quantum mechanical, electronic collective variables that are capable to represent the function of interest. Furthermore, we employ an additional bias that serves to locally modify the already explored regions, driving the dynamics forward, in the limit sampling the whole conformational space.

As a first demonstration, we apply this method in the framework of the complete active space self-consistent field method (CASSCF) to the exploration of "biradicality landscapes" of *p*-xylylene and [8]annulene. From the theoretical point of view, biradicality can be clearly definded employing the occupation numbers of natural orbitals (NOONs) which can be derived from the electronic wavefunction upon calculation and subsequent diagonalization of the density matrix. Therefore, sampling the NOONs within the structural conformation space gives a direct picture of the "biradicality landscape" as presented for *p*-xylylene. In addition, we have carried out further calculations on the biradical conformations of [8]annulene obtained from the ASQPM simulations, enabling the design of stable biradical molecules upon rational substitution, proving that the ASQPM simulations can deliver useful information for the realization of new functional molecules.

5.2. Method

The original metadynamics introduced by Parrinello and coworkers[32,33,35,146–148] represents a sophisticated accelerated molecular dynamics technique using collective variables (CVs) to drive transitions between different barrier-separated basins on the PES, thus allowing for systematic sampling of the PES as well as the determination of free energies. A wide variety of classic CVs has been implemented, ranging from simple geometrical quantities to complex variables constructed by machine learning and dimensionality reduction techniques.[148,149] The method finds broad application in the frame of force field simulations e.g. for investigation of folding mechanisms in proteins,[183] while studies based on quantum chemical metadynamics simulations are still relatively rare.[184,185]

To the best of our knowledge, we have recently published a first multistate formulation of the quantum chemical metadynamics, capable of the automatic localization of conical intersections in molecular systems. The algorithm is available through the metaFALCON program package.[100,101] In the present study, we employ the NOONs as an electronic collective variable, which can be derived from the electronic wavefunction by calculating the one-electron reduced density matrix expanded into the molecular orbital basis. Upon diagonalization, a set of eigenvalue-eigenvector pairs is obtained, representing the reduced density matrix $\mathbf{D}$ in terms of natural orbitals

(NO) φ_i as

$$\mathbf{D}(\mathbf{x}_1, \mathbf{x}_1') = \sum_i n_i \varphi_i^*(\mathbf{x}_1)\varphi_i(\mathbf{x}_1'). \tag{5.1}$$

It should be noticed that the NOs are the best possible approximation of the many-particle problem based on one-electron wavefunctions and can therefore be used as an indicator for unpaired electrons in a molecular system. The corresponding eigenvalues n_i can be interpreted as NOONs.[89,96]

In a closed-shell configuration, all NOONs lie either close to zero or two, i.e. electrons occupy the NOs in pairwise manner. The orbital with the lowest NOON close to two is referred to as highest occupied natural orbital (HONO) with NOON n_H, while the orbital with the highest NOON close to zero is called lowest unoccupied natural orbital (LUNO) with NOON n_L. In an open-shell configuration with even total number of electrons, however, one or several pairs of NOs are singly occupied leading to NOON values close to 1. In the special case of a biradical, two unpaired weakly interacting electrons are present, i.e. $N/2-1$ NOs are doubly occupied, followed by the two NOs with NOON value n_H and n_L that are approximately one. Therefore, the gap between n_H and n_L can serve as a measure for the degree of biradicality (if all other NOONs have values close to zero or two), and thus can be employed as a clearly defined, quantum-mechanical collective variable for the systematic sampling of the biradicality landscape.

Our ASQPM method relies on a molecular dynamics simulation propagating Newtons equation of motion, biased by the modification of the potential energy surface (PES) upon adding a history-dependent potential $V_G(t)$:

$$m_i \ddot{\mathbf{R}}_i = -\nabla_i (V_{el} + V_G(t)), \tag{5.2}$$

with V_{el} representing the unbiased BO PES. The bias potential $V_G(t)$ is built up at regular time steps τ_G by adding gaussian-shaped functions along the electronic CV Δn_{meta} :

$$V_G(t) = \sum_{t'=\tau_G, 2\tau_G, \ldots}^{t} w_G \exp\left(-\frac{\left(\Delta n_{meta}(t) - \Delta n_{meta}(t')\right)^2}{2\delta {\Delta n_{meta}}^2} \right) \cdot \Theta(\Delta n_{meta}(t') - \epsilon), \tag{5.3}$$

while the shape of the added Gaussians is defined by the height w_G and width $\delta\Delta n_{meta}$ parameters. The Heaviside Θ-function is used in order to update the potential only when Δn_{meta} exceeds the threshold ϵ. In order to systematically sample the biradicality landscape we introduce an additional off-diagonal coupling term V_N into the sub-block of the density matrix $\mathbf{D_{diag}}$ containing the HONO and LUNO (represented by their NOON values n_H and n_L). In this way, the corresponding submatrix becomes

$$\mathbf{D_{meta}} = \begin{pmatrix} n_L & V_N \\ V_N & n_H \end{pmatrix}. \tag{5.4}$$

Upon diagonalization of the latter, we obtain an effective NOON gap

$$\Delta n_{meta} = \sqrt{(n_L - n_H)^2 + 4V_N^2}. \tag{5.5}$$

which assumes values between 2 (closed shell structure) and 0 (bi- or polyradical structure), as long as V_N is zero. The off-diagonal biasing potential V_N plays a crucial role in the method allowing the system to move along the biradicalicity landscape. For this purpose, V_N is updated every τ_G steps, if Δn_{meta} drops below ϵ, according to

$$V_N(t) = \sum_{t'=\tau_G,2\tau_G,\ldots}^{t} w_N \exp\left(-\sum_i \frac{(s_i(t) - s_i(t'))^2}{2\delta {s_i}^2}\right) \cdot \Theta(\epsilon - \Delta n_{meta}(t')). \tag{5.6}$$

In order to distinguish between different biradical geometries and prevent the simulation to visit the same part of the landscape several times, a set of additional (geometric) CVs $\{s_i\}$ needs to be chosen. The algorithm and the role of the biasing potentials is schematically illustrated in Fig. 5.1. The restriction to the exploration of biradical structures rather than polyradicals, i.e. all NOONs other than n_L and n_H are close to 0 or 2, is achieved by two quadratic wall potentials acting on n_{L+1} and n_{H-1}

$$V_{wall}^{L+1} = \begin{cases} k(n_{L+1} - \epsilon_{L+1})^2 & \text{for } n_{L+1} > \epsilon_{L+1} \\ 0 & \text{for } n_{L+1} < \epsilon_{L+1} \end{cases}, \tag{5.7}$$

$$V_{wall}^{H-1} = \begin{cases} k(n_{H-1} - \epsilon_{H-1})^2 & \text{for } n_{H-1} < \epsilon_{H-1} \\ 0 & \text{for } n_{H-1} < \epsilon_{H-1} \end{cases}. \tag{5.8}$$

Due to the sorting of the NOONs, these two wall potentials restrict all NOONs other than n_H and n_L to values below ϵ_{L+1} or above ϵ_{H-1}.

Thus, the full equation of motion for the nuclei in the frame of the ASQPM method has the form:

$$m_i \ddot{\mathbf{R}}_i = -\nabla_i (V_{el} + V_G + V_{wall}^{L+1} + V_{wall}^{H-1}), \tag{5.9}$$

where V_{el} is the original electronic potential obtained from the chosen electronic structure method and V_G and $V_{wall}^{L+1} + V_{wall}^{H-1}$ represent the above described biasing potentials.

Evaluation of the nuclear gradients requires the differentiation of Δn_{meta} with respect to the nuclear coordinates

$$\nabla (\Delta n_{meta}) = \frac{(n_L - n_H)\nabla (n_L - n_H) + 4V_N \nabla V_N}{\Delta n_{meta}}, \tag{5.10}$$

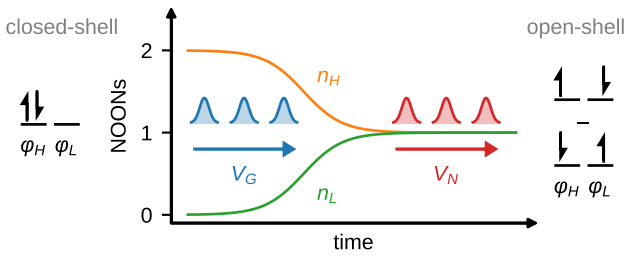

Figure 5.1.: Scheme illustrating the ASQPM algorithm for exploration of the biradicality landscape. At $t = 0$ the system has a closed shell electronic structure with $n_H = 2$ and $n_L = 0$ indicated also by the closed shell electronic configuration in the left part of the figure. Periodic addition of the biasing potentials V_G along the Δn collective variable leads to the gap closing, which is associated with the formation of a singlet biradical geometry characterized by $n_H = 1$ and $n_L = 1$. The exploration of the biradicality landscape is enforced by a periodic addition of an off-diagonal bias V_N forcing the system to explore different geometries with an open shell biradical structure indicated by the electronic configuration in the right part of the figure.

while the gradients ∇n_H and ∇n_L are needed for calculation of the wall potentials in Eqs. 5.7 and 5.8 and are available through numerical differentiation, which can be efficiently parallelized.

For initializing an ASQPM simulation any arbitrary structure of the studied molecular system can be used. For integration of the nuclear equations of motion we employ the velocity Verlet algorithm.[22] The nuclear forces are calculated "on the fly" according to Eq. 5.9. If the starting structure favors a closed shell configuration, the dynamics is dominated by the electronic potential V_{el} in the beginning. As the simulation proceeds, Gaussian-shaped potentials are added to V_G, until the influence of the latter is strong enough to lead the system to a biradical structure with $\Delta n_{meta} \approx 0$. From there on, V_N has growing impact on the dynamics because the small Δn_{meta} activates the addition of Gaussians according to Eq. 5.6, thus starting the biradicalicity landscape exploration phase. The interplay of the two bias potentials V_G and V_N allows to subsequently visit multiple different biradical structures while V_N converges to a hypersurface that can be interpreted as "biradical functional landscape" with respect to the (geometric) CVs s_i.

5.3. Results and Discussion

5.3.1. *p*-Xylylene

In contrast to *m*-xylylene which is a biradical in its most stable singlet ground state structure, a closed-shell quinoidal structure is preferred for *p*-xylylene.[186–188] However, rotation of one of the methylene groups by 90° separates one electron at the respective carbon atom from the planar π-system and therefore changes the electronic character from closed-shell to biradical qualifying *p*-xylylene as an illustrative example for the demonstration of NOON-gap metadynamics. We use the two torsion angles $\{\phi_1, \phi_2\}$ defining the orientation of the methylene groups with respect to the ring plane as a set of CVs in Eq. 5.6 (see Fig. 5.2a), proving in the following section that the ASQPM approach is suitable to find the expected biradical conformations.

Starting the ASQPM simulations from planar *p*-xylylene (shown in Fig. 5.2a), the bias potential V_G drives the molecular dynamics into a biradical configuration space within $1.2\,\mathrm{ps}$. The resulting structure, displayed in Fig. 5.2b, exhibits a 90° twist and pyramidalization of the methylene group. The progression of the frontier NOONs along the $12.0\,\mathrm{ps}$ trajectory presented in Fig. 5.2c clearly indicates that the initial electronic structure is of closed-shell singlet character in the beginning, reflected in occupation numbers close to 0 and 2 while during the first $1.2\,\mathrm{ps}$ the gap between n_H and n_L decreases, reaching an occupation of 1 and 1, respectively. After $2.9\,\mathrm{ps}$, the acting V_G is strong enough to preserve the biradical open-shell singlet character of the wavefunction. Once having reached this NOON configuration, the MD is forced to evolve to "new" structural regions by adding repulsive Gaussians to V_N at the current positions. Therefore, the whole landscape of ϕ_1 and ϕ_2 can be explored (see Fig. C.1 in the ESI) while the value of both n_H and n_L is kept close to 1. When this degeneracy is lifted after $4.5\,\mathrm{ps}$, V_G is again updated, so that the bias towards large values of Δn_{meta} is intensified and thus, the system returns to the closed gap configuration after very short times.

In analogy to the free energy surface obtained from conventional metadynamics,[32] the negative of the resulting V_N represents a hypersurface bearing minima with configurations of ϕ_1 and ϕ_2 corresponding to energetically favorable biradical structures. In contrast to a conventional 2d-scan along the two variables ϕ_1 and ϕ_2 (see Fig.~S2 in the ESI), all degrees of freedom are intrinsically considered and the whole surface refers to biradical structures. The surface depicted in Fig. 5.2d has been obtained after $12.0\,\mathrm{ps}$ from the sum of 110 Gaussians and subsequent symmetrization according to the equivalent nature of ϕ_1 and ϕ_2 as well as positive and negative values of torsion angles. It can be clearly seen that rotation of a single CH_2-moiety is the energetically most affordable way to obtain biradical character in *p*-xylylene. A biradical conformation of both methylenes standing perpendicu-

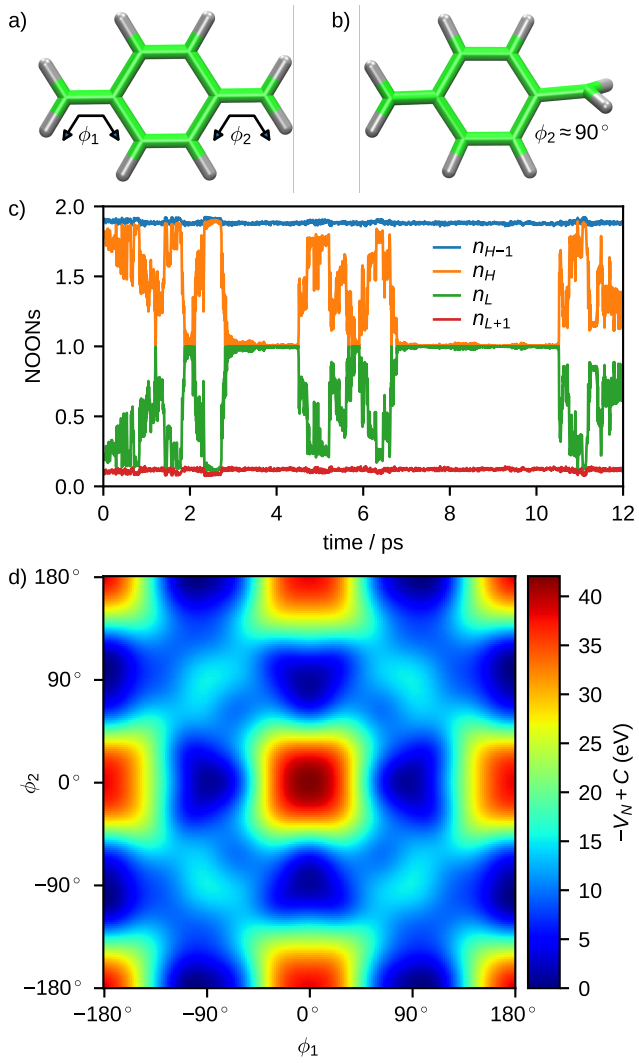

Figure 5.2.: a) Structure of *p*-xylylene and definition of CVs ϕ_1 and ϕ_2. b) Biradical structure reached after $1.2\,\mathrm{ps}$ with one of the methylene groups twisted by almost $90°$. c) Evolution of frontier NOONs along the ASQPM trajectory. d) Biradicalicity hypersurface constructed from the metadynamics potential V_N. The lowest point of the surface has been set to zero.

lar to the central phenyl ring, however, is about $15\,\mathrm{eV}$ less stable in energy, which is probably due to the two strongly localized unpaired electrons on the methylene groups, while in structures with only one rotated CH_2 group, the unpaired electron of the other CH_2 moiety is partly delocalized over the whole remaining π system (see Fig. C.3 in the ESI).

5.3.2. [8]Annulene

In the second example, we elucidate the biradical landscape of [8]annulene, representing a class of molecules bearing a high structural flexibility and therefore several isomeric conformations.[189] The potential energy surface for [8]annulene has been studied in great detail, also employing CASSCF calculations.[190–193] For this purpose, we employ ASQPM simulations along with the NOON gap as electronic CV and the three-dimensional Wiener number[151] W as a versatile CV s_1 in Eq. 5.6. The Wiener number is given as the sum over all interatomic distances in the molecule and therefore correlates with molecular shape. A small Wiener number thereby refers to a relatively compact, sphere-like structure, while planar structures lead to larger values of W. These properties make the Wiener number a generally applicable CV which is especially valuable for systems in which the conformational space should not be limited. In Fig. 5.3a the energy evolution of the singlet and triplet as well as the first excited state along the obtained trajectory is presented. The lowest ground state structure of [8]annulene chosen as initial conformation in the simulation is non-planar, bearing $\mathrm{D_{2d}}$ symmetry (see Fig. 5.3c). As a consequence of the non-degenerate HOMO and LUMO levels, it exhibits a pronounced singlet-triplet gap of more than $3\,\mathrm{eV}$. As depicted in Fig. 5.3b, with growing V_G the molecule rapidly escapes from the initial closed-shell configuration of the frontier orbitals n_H and n_L rearranging in a planar biradical conformation within 400 fs.

The following $7.0\,\mathrm{ps}$ are characterized by an oscillation around the $\mathrm{D_{8h}}$ symmetric structure in which HOMO and LUMO are degenerate in energy and thus the open-shell singlet configuration is favored. As shown in the enlarged view given as inset in Fig. 5.3a, the energy gap between S_0 and S_1 decreases and increases periodically. Furthermore, the occupation of n_H and n_L strongly oscillates indicating that already only slight nuclear motion of the molecule immediately cancels the biradical character of the conformer. These observations can be assigned to the presence of a Jahn-Teller conical intersection arising in axial biradicals like [8]annulene in $\mathrm{D_{8h}}$ symmetry.[54] In this region of the trajectory, the molecule stays almost planar, but C–C bond stretching leads to periodic transient formation of equal bond length and an alternating single / double bond character which breaks the symmetry. In the third section of the trajectory, V_N drives the dynamics towards a $\mathrm{C_s}$ symmetric structure, baring a smaller Wiener number compared to the planar structure (see Fig. C.5 and S6 in the ESI). Remarkably, from $7.0\,\mathrm{ps}$ on, Δn stays close to zero. This

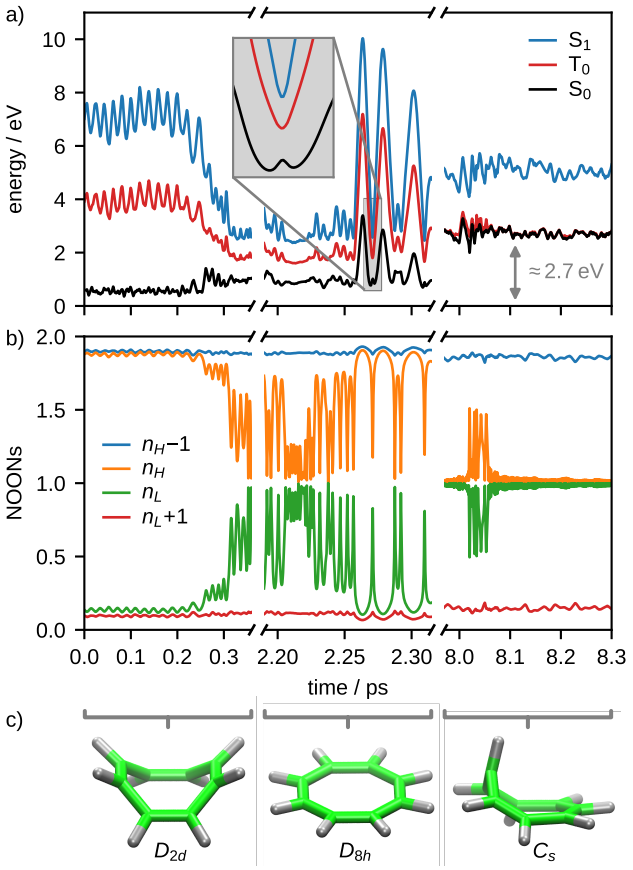

Figure 5.3.: a) Energies of the lowest singlet and triplet as well as the first excited singlet electronic states along an ASQPM trajectory of [8]annulene. b) Evolution of NOONs within the ASQPM simulation. c) Dominant structural character in the highlighted parts of the trajectory.

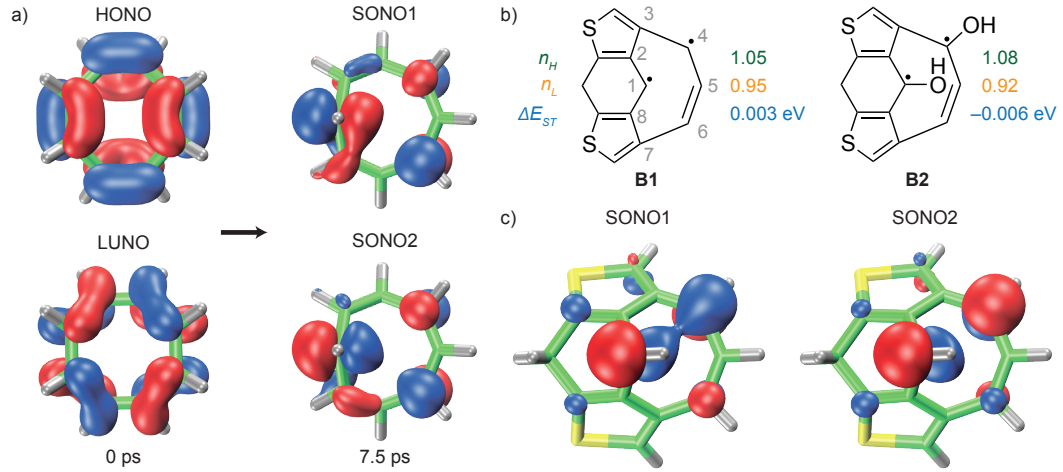

Figure 5.4.: a) HONO and LUNO of the starting structure in the trajectory from Fig. 5.3 compared to the two SONOs after 7.5 ps. b) Rationally designed substituted [8]annulene derivatives **B1** and **B2** with frontier NOONs and singlet triplet gap ΔE_{ST}. The employed numbering scheme for the carbon atoms is depicted in gray. c) Optimized structure and singly-occupied NOs of the stabilized biradical. **B1**.

indicates that the electronic configuration in this range is less sensitive to structural changes. As expected, singlet and triplet energies are degenerate which allows us to characterize the structure to be of biradical character.

The obtained C_s structure is 2.7 eV higher in energy than the ground state equilibrium structure and does not represent a minimum on the potential energy surface. By analyzing the shape of the calculated singly occupied natural orbital (SONO), the location of the respective unpaired electron can be determined. From the orbitals in Fig. 5.4a, it can be seen that both HONO and LUNO are delocalized over all carbon atoms in the beginning of the trajectory. By reaching the biradical C_s structure, they transform into two SONOs that have the largest coefficients at C1, C4 and C6 (see Fig. 5.4b for atom numbering). This allows the interpretation of two unpaired electrons each being localized at one of these three carbon atoms with high probability. This information can be used for the rational stabilization of the biradical structure by the introduction of appropriate substituents (see Fig. 5.4 b). First, we make use of the idea of strengthening the π electron conjugation and thus aromatic structure by introduction of two thiophene units fused to the annulene ring allowing the electronic isolation of two double bonds adjacent to the puckered C1 atom because of the aromaticity of the two 6-electron systems. Additional sterical stability is created by another methylene bridge between the two thiophenes. By these modifications, the

π system of annulene can be characterized as two isolated radicals separated by two closed-shell units integrated into aromatic subsystems. The resulting molecule **B1** has a distorted structure with cancelled symmetry due to partial double bond character between two of the carbon atoms in the remaining planar part. The SONOs of **B1**, given in Fig. 5.4 c), consequently are more localized to one side compared to the unsubstituted annulene. Furthermore, no significant contributions are observed from the carbon atoms fused to the thiophenes. On the other hand, the unpaired electron density is partly delocalized into the thiophene rings. Frontier NOONs of 1.05 and 0.95 and a singlet-triplet gap close to zero indicate an almost perfect biradical character. The introduction of additional hydroxy groups at position 1 and 4 leads to a molecule **B2** (see Fig. 5.4 b) in which the biradical character is mostly preserved and which might be synthetically accessible upon preparation by twofold reduction of the corresponding closed-shell dicarbonyl species. To the best of our knowledge, both **B1** and **B2** have not been described before and are promising candidates to be synthesized. The corresponding frontier natural orbitals are depicted in Fig. C.7 (ESI).

5.4. Computational Details

The electronic structures of both *p*-xylylene and [8]annulene have been calculated on the CASSCF(8,8)/6-31G[125,167,194,195] level as implemented in Molpro2012,[157] including all π orbitals in the active space. MD simulations have been performed using the metaFALCON program[101] utilizing the velocity Verlet algorithm[22] for the integration of the Newtonian equations of motion in steps of $0.25\,\mathrm{fs}$ and temperature was controlled using a Berendsen thermostat[23] at $300\,\mathrm{K}$. Gaussians with a width of 0.1 and height of $0.2\,\mathrm{eV}$ have been added to V_G every 200 time steps according to Eq. 5.3, while a value of 0.1 has been used for ϵ. V_N has been composed from Gaussians with parameters of $0.5\,\mathrm{eV}$ for w_G and $20°$ for $\delta\phi_1$ and $\delta\phi_2$ in *p*-xylylene and $0.1\,\mathrm{eV}$ for w_N and $0.1\,\text{Å}$ for δW in [8]annulene. Parameters of $k = 1.0$, $\epsilon_{L+1} = 0.2$ and $\epsilon_{H-1} = 1.8$ have been used for the construction of V_{wall}^{L+1} and V_{wall}^{H-1}.

5.5. Conclusion

In conclusion, we have introduced a new methodology that allows for an automatic sampling of quantum property manifolds (ASQPM) giving rise to functional landscapes of molecules in analogy to the potential energy surfaces of BO states. This has been achieved by performing biased molecular dynamics simulations, that employ quantum mechanical properties derived from an electronic wavefunction as collective variable.

As a first application we employ the ASQPM simulations in the framework of CASSCF, chosing NOONs as an electronic CV. By inserting an additional off-diagonal bias into the sub-block of the density matrix $\mathbf{D_{diag}}$ containing the HONO and LUNO NOONS n_H and n_L and subsequent diagonalization at the already explored regions, we force the dynamics to systematically sample the biradical conformational space. This allows us to obtain the "biradicality landscape" of *p*-xylylene. Furthermore, we use the ASQPM algorithm in order to generate a biradical conformation of [8]annulene that could be successfully stabilized upon rational substitution as proven by structure optimization and analysis of the obtained NOONs. We have demonstrated that information obtained from ASQPM simulations provides general insight in the structure-function relation in molecular systems and allows designing new stable biradical molecules upon rational substitution. In this way, our method should support experimental chemists in the realization of new molecules with tailored functionality. The method has been implemented into the metaFALCON program package. [101] In principle, within the ASQPM framework any function of interest that can be assigned to a property of the electronic wavefunction, both in ground and in excited state, can be explored and the simulations can be carried out in the framework of an arbitrary quantum chemical method that provides energy gradients and (if desired) excited state energies. Our future work will be devoted to to the implementation of further electronic CVs as well as the extension to QM/MM simulations allowing us to study and design catalytic reaction routes as well as new molecules of tailored functionality.

Acknowledgement

J.O.L. is grateful to the Deutsche Forschungsgemeinschaft (DFG) for financial support through GRK2112: "Molecular Biradicals: Structure, Properties and Reactivity". J.O.L. and M.I.S.R. wish to thank Roland Mitrić for fruitful discussions.

Electronic Supplementary Information

Electronic supplementary information (ESI) available: Further information on the *p*-xylylene and [8]annulene trajectories, static scans of the employed CVs, natural orbitals and cartesian coordinates of the optimized structures.

6. Discussion and Outlook

The photophysics and photochemistry of β-*D*-glucose have been elucidated[99] by nonadiabatic surface hopping[20] and FISH simulations[45] which allow to derive a comprehensive picture of the underlying light-induced processes, giving rise to time scales and explicit population dynamics initiated upon irradiation by light. This is explicitly taken into account by inserting the interaction with the electric field of a simulated laser pulse into the time-dependent Schrödinger equation and propagating classical trajectories that are allowed to hop between electronic BO PESs according to quantum-mechanically derived probabilities.

Due to the absence of a chromophoric unit, β-*D*-glucose has a well-separated electronic ground state and absorbs light in the UV range. Nonetheless, it exhibits interesting excited state dynamics, since the nonadiabatic simulations presented in chapter 2 reveal that nonradiative decay upon excitation into one of the excited singlet states appears on the femtosecond time scale. Furthermore, the simulations of the real time evolution of electronically excited glucose show that CIs with O−H bond elongation or ring-opening character are responsible for the ultrafast return to the ground state which is in line with former static calculations.[117] Remarkably, CIs with elongated O−H bonds are higher in energy compared to ring-opening CIs, but are reached more easily after photoexcitation because of smaller geometric distortion. This indicates that investigations of photophysical processes should not be limited to the low-energetic regions of the intersection seam only. Instead, depending on the pathway connecting the Franck-Condon region with the intersection seam, higher energetic parts can also be important. Despite the small size of the glucose molecule, a large variety of different CIs is involved in the photophysical processes after the initial excitation.

This raises the question to which extent CIs play a role also in the photophysics of other classes of molecules, bearing higher complexity. As a first estimation, the energetic and structural assessment of the CIs is already a valuable information, without the need to perform detailed dynamics simulations.

For this purpose, the multistate metadynamics was developed as a method for the systematic exploration of CIs in large molecular systems.[100] This method, introduced in chapter 3, is particularly interesting because of its low prerequisites. Although some basic knowledge on the shape of CI structures might be helpful for the definition of suitable CVs, any arbitrary ground state structure of the molecule of interest is sufficient for the exploration of a large part of the conformational space.

This is clearly an advantage over the established methods that usually require an initial guess of the CI structure, e.g. from previously performed nonadiabatic dynamics simulations. Furthermore, the method presented herein does not require the calculation of nonadiabatic couplings, only energy and gradients of the regarded states have to be available from the applied electronic structure methods. Apart from that, the established CI optimization procedures rely on the detection of MECPs. However, as already shown for the glucose molecule, the structural and energetic accessibility of the pathways connecting the intersection seam with the Franck-Condon region determines the points at which transitions into other electronic states are likely to occur.

As a consequence, for an estimation of the photophysics in molecules it is necessary to obtain a global picture of the intersection seam rather than only MECPs. As shown in chapter 4, the multistate metadynamics algorithm allows to systematically investigate the intersection seam[101] and is therefore perfectly suited for the investigation of complex molecular species for which the photophysics and photochemistry are not known in detail. Furthermore, the method allows to estimate the accessibility of regions, where transitions between the investigated electronic states most likely happen, as presented for 9H-adenine.

The publication of the metaFALCON software[101] as a framework for the multistate metadynamics enables the broad use of the method on any desired molecular system and therefore helps establish the algorithm as a generally applicable tool for the investigation of photophysical and photochemical processes. In particular, the information obtained by the use of the metaFALCON package might be helpful for the design of new molecules with specific light-induced functionality.

Following the idea of designing molecules with tailored functionality, the multistate metadynamics has been generalized to the exploration of any quantum-mechanical property of the electronic wavefunction, giving rise to the ASQPM method[103] as introduced in chapter 5. This method serves as a valuable tool, for example for the further development of promising new materials for optoelectronic devices, as demonstrated in a first application in which the biradical character in singlet state molecular species has been elucidated. Because of their remarkably low-lying triplet state energies, biradicals and biradicaloids have promising properties for example for future improvements in efficient OLED design or towards the application of singlet fission, but, on the other hand, are demanding to handle because of their open-shell character. Especially the challenging task of increasing their stability needs to be addressed in order to create durable devices for consumer applications. The simulation-assisted identification of new scaffolds can enable the synthesis of new compound classes. Based on a distorted geometry of [8]annulene, we have proposed new stabilized molecular biradicals (see section 5.3.2), and the systematic investigation of larger annulenes with different sizes would be an interesting further application of the presented method. Due to the larger conforma-

tional flexibility, it is expected that more different biradical scaffolds can be found with increasing ring system size.

For both the multistate metadynamics and ASQPM methods, the efficiency in terms of simulation time is crucial for the question whether these approaches will become established alongside the conventional local optimization schemes. In all the examples shown in chapters 3 – 5, trajectories of several picoseconds length are needed to sample multiple structures with the desired electronic properties. The metadynamics approach,[32] which is the basis of the presented methods, in principle is suitable to be used for large molecular systems since it does not require solving of computationally expensive mathematical equations. Furthermore, whenever numerical gradients of CVs are necessary, a parallelized implementation is employed in the metaFALCON program which allows the efficient computation even for large systems. The main computational effort during such simulations is the electronic structure calculation and the determination of the electronic energy gradients carried out in every dynamics step. One possibility for the acceleration of the sampling would be to strengthen the acting bias by increasing the deposition rate or height of the Gaussians added to the metadynamics potential. However, there is a natural limit for this approach, since trajectory heating upon continuous addition of large energy amounts cannot be controlled by the thermostat anymore. At this point it is worth to emphasize that the automatic sampling methods presented in this thesis do not require the relative electronic energies of the identified structures to be quantitatively correct, since the explorations are driven by qualitative changes of collective variables. A more promising approach, therefore, is to reduce the computational effort by using efficient semiempirical or tight-binding methods, as has been demonstrated in section 4.4.3. This allows for an efficient global sampling which can be followed by local improvements to the identified promising structures on a higher level of theory (see Fig. 6.1). Another point of potential improvement is the optimization of interfaces to electronic structure programs. Especially for fast quantum chemical methods, the utilization of text-based interfaces produces large overhead to the computation time because of numerous file reading and writing processes. Electronic structure codes that can be directly interfaced to the metaFALCON program, such as the python-based DFTBaby[196] for tight-binding DFT, should be strongly preferred.

Apart from efficiency, the stability of the presented automatic sampling algorithms is an important aspect and can potentially be further improved. Although the new methodology allows to successfully obtain multiple CI structures in a single multistate metadynamics trajectory, in all the examples given in chapters 3 and 4, irreversible molecular fragmentations and especially the dissociation of hydrogen atoms forced the dynamics to stop. Consequently, a multi-trajectory approach was applied for the sampling of a complete picture of the intersection seam. A methodology to prevent a trajectory from abortion because of dissociations is therefore highly

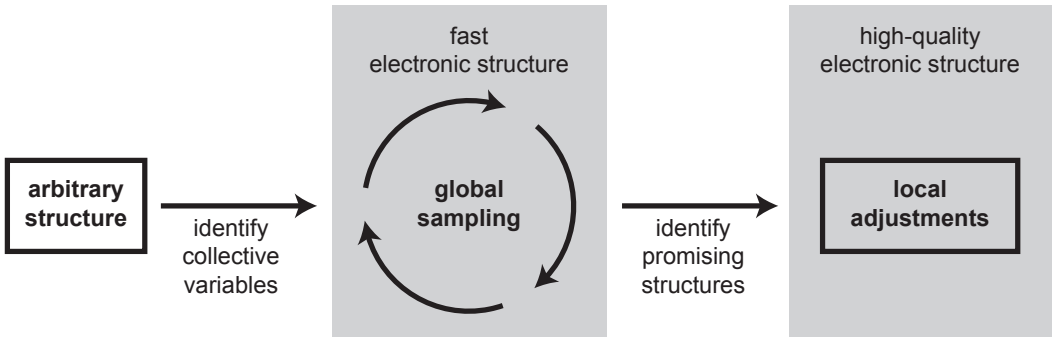

Figure 6.1.: Proposed two-step procedure for the efficient automatic enhanced sampling. An arbitrary structure is used as a starting point for the metadynamics with electronic CVs. The most time consuming part of the simulation is the global exploration of the desired functional landscape which should therefore be performed in the framework of a fast electronic structure method. Promising candidates for the further investigation (e.g. local optimization or stabilization by the introduction of substituents) can follow employing a high-quality electronic structure method.

desired, for example based on additional wall potentials or simply by an automatic reset of the respective trajectory to a time step before the dissociation accompanied by a small perturbation. In this way, the simulation could proceed in the already built-up bias potentials and a different pathway than before is likely to be taken.

For the implementation of all the newly developed methods described in this thesis, the metaFALCON program package[101] has been developed as a comprehensive tool for numerous application scenarios. This software can be employed for MD simulations at constant energy or coupled to an external bath using different kinds of thermostats,[23,24] as well as metadynamics simulations in the original[32] and well-tempered[33] formulations. Its core functionality is the application of multistate metadynamics[100] and ASQPM methods[103] for the exploration of conical intersection seams and biradicalicity landscapes in molecular systems. Interfaces to several *ab initio* and semiempirical quantum chemistry codes are provided, allowing to choose the best suited electronic structure method for the investigated system. The package is written in python, a versatile and popular programming language, which easily allows modifications for future research and method development.

In this regard, the implementation of highly specialized geometric CVs for the exploration of CI seams or biradicalicity landscapes is easily possible, enabling the application to many kinds of different molecules. Furthermore, the extension of the ASQPM method with respect to other electronic CVs is straightforwardly

possible. An interesting extension of the multistate metadynamics would be the generalization to CIs between states with different spin. Singlet-triplet ISC for example plays an important role in catalysis mediated by transition metals such as oxygen release in the natural oxygen-evolving complex[197] or artificial molecular water oxidation catalysts.[198] Further improvement of the simulations, for example for the explicit inclusion of solvent effects, would be achieved by the combination of the presented methods with hybrid QM/MM schemes that could also be implemented into the metaFALCON package.

7. Summary

The aim of this thesis was to develop new automatic enhanced sampling methods by extending the idea of Parrinello's metadynamics[32] to multistate problems and by introducing new quantum-mechanical electronic collective variables. These methods open up a rich perspective for applications to the photophysical processes in complex molecular systems, which play a major role in many natural processes such as vision and photosynthesis, but also in the development of new materials for organic electronics, whose function depends on specific electronic properties such as biradicalicity.

In the context of photochemistry and photophysics, conical intersections – crossing points between two Born-Oppenheimer potential energy surfaces – are of particular interest, since population transfer and thus nonradiative relaxation is particularly efficient for molecular geometries in their vicinity.

In chapter 2, quantum-classical nonadiabatic surface-hopping dynamics are performed to investigate the ultrafast photodynamics upon UV excitation in β-*D*-Glucose.[99] In spite of their importance as ubiquitous biomolecules, the excited state properties of carbohydrates have been subject to only few studies in the past, mainly due to the absence of a chromophore unit and relatively high excitation energies that are not easily accessible experimentally. Because of the high density of excited electronic states, field-induced surface hopping (FISH) dynamics was applied in addition to the conventional nonadiabatic dynamics simulations in order to account for the realistic excited state population dynamics after a laser excitation. Consistent with static calculations, a variety of conical intersection geometries have been identified to be responsible for ultrafast return into the ground state which can be categorized into different O−H elongations and ring-openings. The results show that even in relatively small molecular systems like glucose, photophysical and photochemical processes can be complicated and thus a global assessment of the intersection seam would be highly desirable.

This has motivated the development of the multistate metadynamics with electronic collective variables,[100] which represents the major methodological achievement of this thesis and is presented in chapter 3. In order to allow for systematic exploration of conical intersections in molecular systems, the multistate electronic hamiltonian in the framework of the Born-Oppenheimer approximation has been extended by an off-diagonal (repulsive) bias potential. The resulting effective energy gap between the electronic states of interest is employed as a collective vari-

able in the metadynamics simulations. In this way, classical trajectories in the electronic ground state starting from an arbitrary initial structure are driven towards the conical intersection seam. When the system is close to the crossing region, the off-diagonal bias is updated in regular time steps in order to allow the subsequent exploration of multiple conical intersection structures within a single trajectory run. The furan molecule has been used as an illustrative example to demonstrate that the method is able to find a variety of ring-puckering and ring-opening conical intersections, that have been recently also detected experimentally.[78]

In chapter 4, the implementation of the developed methodology into the ***meta**dynamics package **f**or the **a**utomatic **l**ocalization of **con**ical intersections* (metaFALCON) program package is presented.[101] Here, the multistate metadynamics has been interfaced to several widely used eletronic structure codes within an open source python-based program package. In addition, systematic assessments of the employed collective variables and parameters used to construct the Gaussian-shaped bias potentials are performed to improve the sampling efficiency. For this purpose, simulations on 1,3-butadiene and benzene reveal that the three-dimensional Wiener number is a valuable descriptor for multistate metadynamics simulations with minimal prerequisite knowledge. Furthermore, Cremer-Pople ring-puckering coordinates have been implemented as collective variables in order to systematically explore the possible distortions in cyclic systems and have been applied to the pyrimidine ring in 9H-adenine. For the first time, a global picture on the intersection seam is automatically obtained as an energetic hypersurface on which all minimum energy crossing points in the configurational space appear as minima.

Finally, in chapter 5, a new concept for the automatic sampling of quantum property manifolds (ASQPM) is introduced, based on a generalization of the multistate metadynamics.[103] In this approach, electronic collective variables are used to generate "functional landscapes" which can be helpful for the tailored design of new molecules serving as building blocks in functional materials. Occupation numbers of natural orbitals are employed as a measure for biradical character and the extended metadynamics is used to identify biradical conformations of organic molecules which have closed-shell character in their equilibrium conformation. Rotation of the methylene groups in *p*-xylylene is used as an example to obtain a biradicalicity landscape from which information on low-energetic biradical conformations can be extracted. As illustrated in a study of [8]annulene, the obtained structures can be used as building blocks for the design of new stable biradicals. By tuning the steric and electronic properties of the molecule with the introduction of suitable substituents, the antiaromatic ring system could be stabilized in structures with pronounced biradical character and degenerate singlet and triplet ground states. The method can be easily extended to other properties of the electronic wavefunction and therefore represents a valuable tool for the simulation-assisted design of

novel functional materials.

8. Zusammenfassung

Das Ziel dieser Arbeit war die Entwicklung neuer automatisierter Methoden für beschleunigtes Sampling molekularer Strukturen durch eine Erweiterung von Parrinellos Metadynamik[32] auf Mehrzustandsprobleme und die Verwendung neuer quantenmechanischer elektronischer kollektiver Variablen. Die entwickelten Methoden bieten einen breiten Anwendungsspielraum im Bereich der photophysikalischen Prozesse komplexer molekularer Systeme, welchen in vielen natürlichen Vorgängen wie beispielsweise dem Sehen und der Photosynthese, aber auch in der Entwicklung neuer Materialien für die organische Elektronik eine Schlüsselrolle zukommt. Die Eigenschaften solcher funktioneller Materialien werden durch spezifische elektronische Eigenschaften wie dem Biradikalcharakter bestimmt.

Im Kontext der Photochemie und Photophysik sind konische Durchschneidungen, also Kreuzungspunkte zwischen zwei Born-Oppenheimer Potentialenergieflächen, von besonderer Bedeutung, da der Populationstransfer und somit nichtstrahlende Zerfallsprozesse in ihrer Nähe besonders effizient ablaufen können.

In Kapitel 2 wird mit Hilfe von quantenklassischen nichtadiabatischen Surface-Hopping Simulationen die ultraschnelle Photodynamik in β-*D*-Glukose untersucht,[99] die durch UV-Anregung ausgelöst wird. Obwohl Kohlenhydrate eine Klasse von allgegenwärtigen Biomolekülen darstellen, sind die Eigenschaften ihrer elektronisch angeregten Zustände bisher wenig erforscht, was hauptsächlich daran liegt, dass sie keine farbgebenden Einheiten aufweisen und die Realisierung der relativ hohen benötigten Anregungsenergien experimentell anspruchsvoll ist. Aufgrund der hohen Dichte von elektronisch angeregten Zuständen wurde neben den konventionellen nichtadiabatischen Dynamiksimulationen auch die Methode des feldinduzierten Surface-Hopping (FISH) angewendet, um die realistischen Zustandsbesetzungen nach einer Laseranregung korrekt abzubilden. In Übereinstimmung mit früheren statischen Rechnungen wurden verschiedenste konische Durchschneidungen identifiziert, die für die ultraschnelle Rückkehr in den Grundzustand verantwortlich sind. Diese können in eine Gruppe von unterschiedlichen O–H Bindungsstreckungen und eine Gruppe von Ringöffnungsgeometrien eingeteilt werden. Die Ergebnisse zeigen, dass die photophysikalischen und photochemischen Prozesse selbst in relativ kleinen Molekülen wie Glukose bereits kompliziert sein können und dass ein globaler Blick auf den Durchschneidungssaum sehr hilfreich wäre.

Vor diesem Hintergrund wurde die Mehrzustandsmetadynamik mit elektroni-

schen kollektiven Variablen entwickelt, welche die wichtigste methodologische Errungenschaft dieser Arbeit darstellt und in Kapitel 3 beschrieben wird.[100] Um eine systematische Erkundung von konischen Durchschneidungen in molekularen Systemen zu ermöglichen, wurde die elektronische Mehrzustands-Hamiltonmatrix im Rahmen der Born-Oppenheimer-Näherung durch ein (repulsives) Störpotential in den Außerdiagonalelementen erweitert. Die daraus erhaltene effektive Energielücke zwischen den beiden untersuchten elektronischen Zuständen wird als kollektive Variable für Metadynamiksimulationen verwendet. Dadurch werden klassische Trajektorien von einer beliebigen Ausgangsgeometrie in Richtung des Durchschneidungssaums getrieben. Wenn sich das System der Kreuzungsregion nähert, wird das außerdiagonale Potential in regelmäßigen Zeitabständen aktualisiert, um die Erkundung mehrerer konischer Durchschneidungen mit der Simulation einer einzigen Trajektorie zu ermöglichen. Am Beispiel des Furanmoleküls wird gezeigt, dass die Methode geeignet ist, eine Reihe von sogenannten Puckering- und Ringöffnungsdurchschneidungen zu finden, welche vor Kurzem auch experimentell nachgewiesen wurden.[78]

In Kapitel 4 wird die Implementierung der entwickelten Methode im Softwarepaket ***meta****dynamics package* ***f****or the* ***a****utomatic* ***l****ocalization of* ***con****ical intersections* (metaFALCON) beschrieben.[101] Dieses Python-Paket auf Open-Source Basis verbindet die Mehrzustandsmetadynamik mit einigen verbreiteten Programmen zur Berechnung der elektronischen Struktur. Zusätzlich wird die optimale Wahl der verwendeten kollektiven Variablen sowie die Form der für die Störpotentiale verwendeten Gaussfunktionen ausführlich untersucht, um die Effizienz zu steigern. Anhand der Beispiele von 1,3-Butadien und Benzol wird gezeigt, dass die dreidimensionale Wienerzahl ein geeigneter Deskriptor für die Mehrzustandsmetadynamik mit möglichst wenig vorausgesetztem Wissen über das betrachtete System ist. Desweiteren wurden Cremer-Pople-Parameter als kollektive Variablen implementiert. Sie erlauben die automatische Erkundung der Verzerrung von Ringsystemen, wie am Beispiel des Pyrimidinrings in 9H-Adenin gezeigt wird. Erstmalig wurde automatisch ein globales Bild des Durchschneidungssaums in Form einer energetischen Hyperfläche generiert, auf der alle Kreuzungspunkte minimaler Energie des betrachteten Konfigurationsraums als Minima auftreten.

Schließlich wird in Kapitel 5 eine Verallgemeinerung der Mehrzustandsmetadynamik für das automatische Sampling von Strukturen mit bestimmten quantenmechanischen Eigenschaften (Automatic Sampling of Quantum Property Manifolds, ASQPM) eingeführt.[103] In diesem Ansatz werden elektronische kollektive Variablen verwendet, um „funktionelle Landschaften“ zu generieren, die hilfreich für das zielgerichtete Design von neuen Molekülen für Materialanwendungen sind. Dabei werden Besetzungszahlen natürlicher Orbitale als Maß für den Biradikalcharakter herangezogen. Die erweiterte Metadynamik wird verwendet, um biradikalische Konformationen von organischen Molekülen zu identifizieren, welche

in ihrer Gleichgewichtsstruktur einen geschlossenschaligen Charakter haben. Die Rotation der Methylengruppen in *p*-Xylylen dient als Beispiel für die Generierung einer Biradikalitätslandschaft, aus der Informationen zu niedrigenergetischen Biradikalkonformationen gewonnen werden können. Wie am Beispiel von [8]Annulen gezeigt, können die erhaltenen Strukturen als Grundbausteine für neue, stabile Biradikale genutzt werden. Die zielgerichtete Einstellung der sterischen und elektronischen Eigenschaften durch die Einführung von passenden Substituenten ermöglicht die Stabilisierung des antiaromatischen Ringsystems in einer Konformation mit ausgeprägtem Biradikalcharakter und entarteten Singulett- und Triplett-Grundzuständen. Die Methode ist leicht auf andere Eigenschaften der elektronischen Wellenfunktion erweiterbar und stellt daher ein nützliches Werkzeug für das simulationsgestützte Design von neuen funktionellen Materialien dar.

A. Supporting Information to Ultrafast Photodynamics of Glucose

Table A.1.: Cartesian coordinates of the optimized structure of β-D-glucose obtained by DFT (B3LYP, 6-31++G). Energy: $-686.6305948165\,E_H$hgh

O	0.4425785	-1.4005781	-0.2078745
C	-0.9920354	-1.2947353	-0.4384342
C	1.2309564	-0.2297851	-0.6592670
O	-1.6202497	-2.4422834	0.1242136
C	2.6733396	-0.5646484	-0.2997864
H	1.1358423	-0.1216849	-1.7498507
C	0.6982570	1.0357827	0.0238594
O	1.3945078	2.1521014	-0.6011656
C	-0.8093450	1.1757813	-0.1700347
H	0.9294265	1.0012006	1.0950725
O	-1.2169021	2.3458541	0.5959337
H	-1.0262036	1.3481246	-1.2344534
C	-1.5428949	-0.0765062	0.2920252
O	-2.9511355	0.1387357	-0.0144094
H	-1.4051370	-0.227966	1.3696792
H	-3.4916842	-0.6079658	0.3135854
H	-2.1869412	2.4636568	0.5330705
H	1.0886865	2.9921970	-0.2020192
H	3.3136596	0.2933365	-0.5074477
O	2.8215000	-0.8432738	1.1220251
H	3.0050920	-1.4259765	-0.8940281
H	2.2191465	-1.5747827	1.3719849
H	-1.2862741	-3.2706160	-0.2748250
H	-1.1773819	-1.2307745	-1.5216727

Table A.2.: Lowest excitation energies (in eV) of β-D-glucose obtained by the different quantum chemical methods employed for surface hopping simulations. The oscillator strengths are given in parentheses.

State	TDDFT (B3LYP/6-31++G)	TDDFT (B3LYP/6-31++G**)	ADC(2) (aug-cc-pVDZ)
S_1	6.284 (0.0033)	6.204 (0.0047)	6.276 (0.0067)
S_2	6.410 (0.0042)	6.462 (0.0037)	6.617 (0.0084)

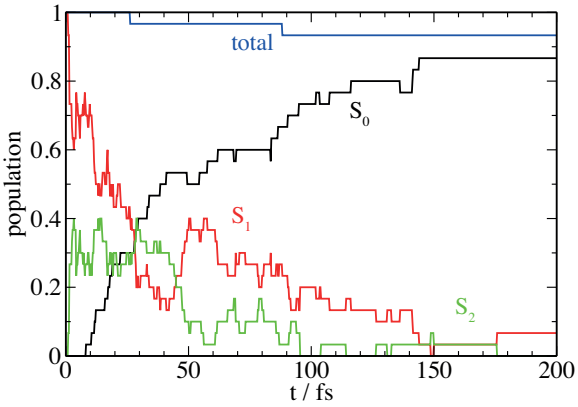

Figure A.1.: Time-dependent electronic state populations for nonadiabatic surface-hopping dynamics of β-D-glucose starting in the S_1 state, obtained by TDDFT employing the B3LYP functional and 6-31++G** basis set. The ensemble comprised 30 trajectories whose initial conditions were sampled from a harmonic Wigner function at 250 K. The decrease of the total population is due to such trajectories that resided in the S_2 state when reaching the vicinity of an S_0-S_1 CI, where the propagation was stopped.

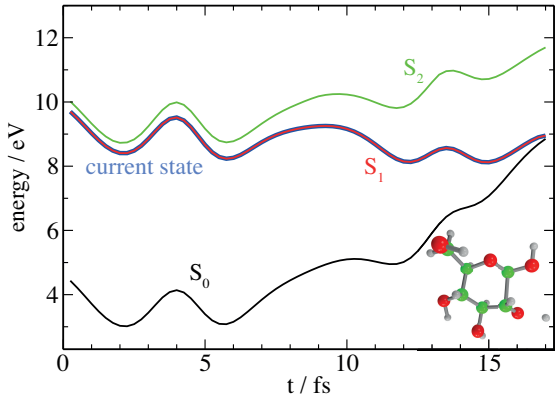

Figure A.2.: Energies of the lowest 3 electronic states along a selected TDDFT (B3LYP/6-31++G**) trajectory initiated in the S_1 state, where the O^2-H-elongation leads to a conical intersection. Energies are given relative to the optimized geometry of the ground state.

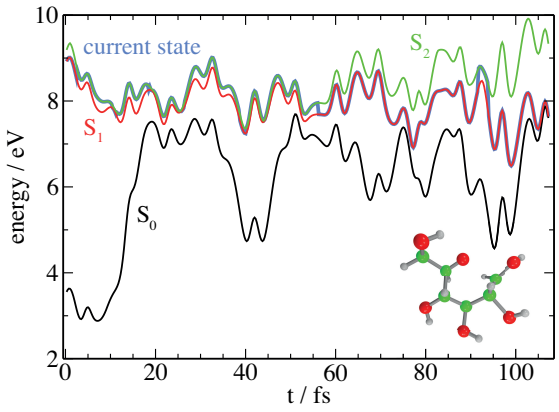

Figure A.3.: Energies of the lowest 3 electronic states along a selected TDDFT (B3LYP/6-31++G**) trajectory initiated in the S_1 state, where the C^1-O^1 ring-opening leads to a conical intersection. Energies are given relative to the optimized geometry of the ground state.

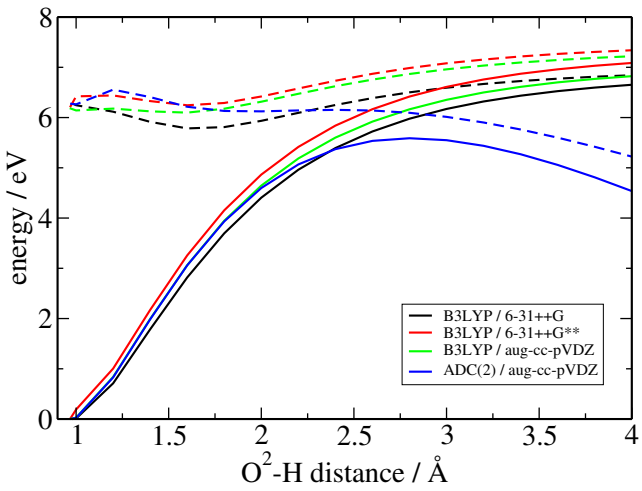

Figure A.4.: Scan of the energies of the electronic ground state (full lines) and the first excited state (dashed lines) along the O^2-H bond stretching coordinate employing different quantum chemical methods.

B. Definition of Cremer-Pople Parameters

Cremer-Pople parameters as CVs in N-membered cyclic systems. In order to define the Cremer-Pople parameters in a N-membered cyclic system, it is first necessary to shift the molecular coordinates $\mathbf{R}$ with respect to the origin such that the following condition is satisfied,

$$\sum_{i=1}^{N} \mathbf{R_i} = 0, \tag{B.1}$$

and rotate them in a way that the xy-plane is the mean ring plane and the atomic positions on the z-axis correspond to the displacements from the latter. In order to define such a plane uniquely, the y-axis is fixed to the position vector of atom 1 and two vectors

$$\mathbf{R}' = \sum_{i=1}^{N} \mathbf{R_i} \sin\left[2\pi(i-1)/N\right], \tag{B.2}$$

$$\mathbf{R}'' = \sum_{i=1}^{N} \mathbf{R_i} \cos\left[2\pi(i-1)/N\right] \tag{B.3}$$

are used to define the unit normal vector of the plane

$$\mathbf{n} = \frac{\mathbf{R}' \times \mathbf{R}''}{|\mathbf{R}' \times \mathbf{R}''|}. \tag{B.4}$$

Note that $\mathbf{R}'$ and $\mathbf{R}''$ are dependent on the atom-numbering. The new z-coordinates of all atoms within the ring are then obtained by the projection of $\mathbf{R_i}$ on $\mathbf{n}$

$$z_i = \mathbf{R_i} \cdot \mathbf{n}. \tag{B.5}$$

Based on this set of transformed coordinates, Cremer and Pople define $(N-3)/2$ amplitude-phase pairs if N is odd. Otherwise, $(N-4)/2$ amplitude-phase pairs are obtained alongside another single amplitude. A six-membered ring, for example, leads to the definition of the amplitude q_2 and phase ϕ_2 in the following manner:

$$q_2 \sin\phi_2 = -\frac{1}{\sqrt{3}} \sum_{i=1}^{6} z_i \sin\left(\frac{2}{3}\pi(i-1)\right) =: A \tag{B.6}$$

$$q_2 \cos\phi_2 = \frac{1}{\sqrt{3}} \sum_{i=1}^{6} z_i \cos\left(\frac{2}{3}\pi(i-1)\right) =: B \tag{B.7}$$

The additional single puckering amplitude q_3 reads

$$q_3 = \frac{1}{\sqrt{6}} \sum_{i=1}^{6} (-1)^{i-1} z_i. \tag{B.8}$$

Since the physical meanings of q_2 and q_3 are not straightforward, it is convenient to transform the three parameters from Eqs. B.6–B.8 into a set of spherical polar coordinates Q, ϕ and θ. For this reason, q_2 and q_3 are expressed in polar coordinates

$$q_2 = Q \sin\theta, \tag{B.9}$$

$$q_3 = Q \cos\theta. \tag{B.10}$$

That leads, on the one hand, to the definition of the total puckering amplitude

$$Q = \left(q_2^2 + q_3^2\right)^{1/2} = \left(\sum_{i=1}^{6} z_i^2\right)^{1/2} \tag{B.11}$$

which is zero for the flat ring structure and increases for larger $|z_i|$ values. On the other hand, the corresponding angle

$$\theta = \arctan\frac{q_2}{q_3} \tag{B.12}$$

represents the puckering character, i.e. the transition from one chair ($0°$) over boat / skew-boat ($90°$) structures to the other chair form ($180°$). The third parameter

$$\phi = \phi_2 = \arctan\frac{A}{B} \tag{B.13}$$

can be understood as a phase angle and takes values from $0°$ to $360°$.

According to the chain rule, gradients of Cremer-Pople parameters split into the differentiation with respect to the vector of z_i-components $\mathbf{z}$ and the derivative of the latter with respect to the cartesian coordinates $\mathbf{R}$

$$\nabla Q = \frac{\partial Q}{\partial \mathbf{z}} \frac{\partial \mathbf{z}}{\partial \mathbf{R}}, \nabla\phi = \frac{\partial \phi}{\partial \mathbf{z}} \frac{\partial \mathbf{z}}{\partial \mathbf{R}}, \nabla\theta = \frac{\partial \theta}{\partial \mathbf{z}} \frac{\partial \mathbf{z}}{\partial \mathbf{R}}. \tag{B.14}$$

Since Q is only dependent on the components of $\mathbf{z}$ directly according to Eq. B.11, its derivative takes the simple form

$$\frac{\partial Q}{\partial \mathbf{z}} = \frac{\partial}{\partial \mathbf{z}} \sqrt{\sum_{i=1}^{6} z_i^2} = \frac{\mathbf{z}}{Q}. \tag{B.15}$$

The derivative of ϕ with respect to $\mathbf{z}$

$$\frac{\partial \phi}{\partial \mathbf{z}} = \frac{B\frac{\partial A}{\partial \mathbf{z}} - A\frac{\partial B}{\partial \mathbf{z}}}{B^2\left(1+(A/B)^2\right)} \tag{B.16}$$

follows from Eq. B.13 and requires the additional differentiation of the term A from Eq. B.6

$$\frac{\partial A}{\partial z_i} = \sin\left(\frac{2}{3}\pi(i-1)\right) \tag{B.17}$$

and the term B from Eq. B.7

$$\frac{\partial B}{\partial z_i} = \cos\left(\frac{2}{3}\pi(i-1)\right). \tag{B.18}$$

For the evaluation of $\nabla\theta$, either of Eq. B.9, Eq. B.10 and Eq. B.12 could be used, but the easiest approach is reached from the expression in Eq. B.10

$$\frac{\partial \theta}{\partial \mathbf{z}} = \left(\left(\frac{q_3}{Q}\right)^2 - 1\right)^{-1/2} \frac{Q\frac{\partial q_3}{\partial \mathbf{z}} - q_3\frac{\partial Q}{\partial \mathbf{z}}}{Q^2}, \tag{B.19}$$

because $\partial Q/\partial \mathbf{z}$ is easily accessible from Eq. B.15 and $\partial q_3/\partial z_i$ is derived from Eq. B.8 as

$$\frac{\partial q_3}{\partial z_i} = \frac{1}{\sqrt{6}}(-1)^{i-1}. \tag{B.20}$$

Finally, each component of $\mathbf{z}$ depends on $\mathbf{R}$ in $\mathbf{R_i}$ and $\mathbf{n}$, so its derivative is given by

$$\frac{\partial z_i}{\partial \mathbf{R}} = \frac{\partial \mathbf{R_i}}{\partial \mathbf{R}} \cdot \mathbf{n} + \mathbf{R_i} \cdot \frac{\partial \mathbf{n}}{\partial \mathbf{R}} \tag{B.21}$$

where $\partial \mathbf{R_i}/\partial \mathbf{R}$ is trivial and the gradient of the normed normal vector has the form

$$\frac{\partial \mathbf{n}}{\partial \mathbf{R}} = \frac{\frac{\partial}{\partial \mathbf{R}}\left(\mathbf{R}' \times \mathbf{R}''\right)\left|\mathbf{R}' \times \mathbf{R}''\right| - \left(\mathbf{R}' \times \mathbf{R}''\right)\frac{\partial}{\partial \mathbf{R}}\left|\mathbf{R}' \times \mathbf{R}''\right|}{\left|\mathbf{R}' \times \mathbf{R}''\right|^2}. \tag{B.22}$$

This requires the differentiation of the cross product between the vectors $\mathbf{R}'$ and $\mathbf{R}''$

$$\frac{\partial}{\partial \mathbf{R}}\left(\mathbf{R}' \times \mathbf{R}''\right) = \frac{\partial \mathbf{R}'}{\partial \mathbf{R}} \times \mathbf{R}'' + \mathbf{R}' \times \frac{\partial \mathbf{R}''}{\partial \mathbf{R}}, \tag{B.23}$$

with the 3×3 components

$$\frac{\partial \mathbf{R}'}{\partial \mathbf{R_i}} = \sin\left(\frac{1}{3}\pi(i-1)\right)\mathbf{I} \tag{B.24}$$

and

$$\frac{\partial \mathbf{R}''}{\partial \mathbf{R_i}} = \cos\left(\frac{1}{3}\pi(i-1)\right)\mathbf{I}, \tag{B.25}$$

where $\mathbf{I}$ is the three-dimensional identity matrix.

C. Supporting Information to Metadynamics for Automatic Sampling of Quantum Property Manifolds: Exploration of Molecular Biradicality Landscapes

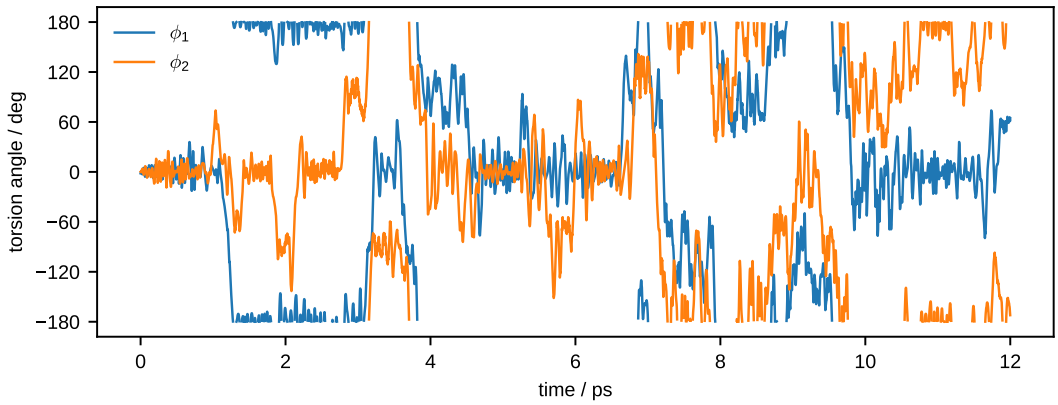

Figure C.1.: Torsion angles ϕ_1 and ϕ_2 along the ASQPM trajectory of *p*-xylylene.

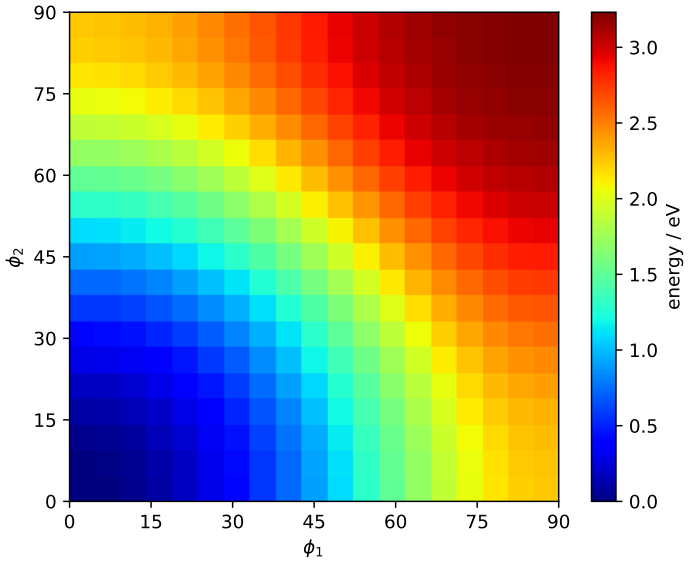

(a)

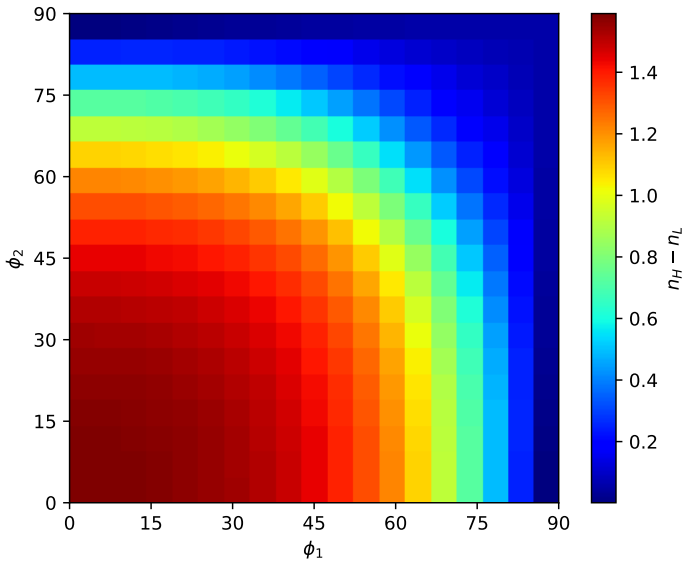

(b)

Figure C.2.: a) Ground state energy and b) gap between frontier NOONs along a fixed scan of the two CVs ϕ_1 and ϕ_2 in *p*-xylylene using an increment of 5 degrees.

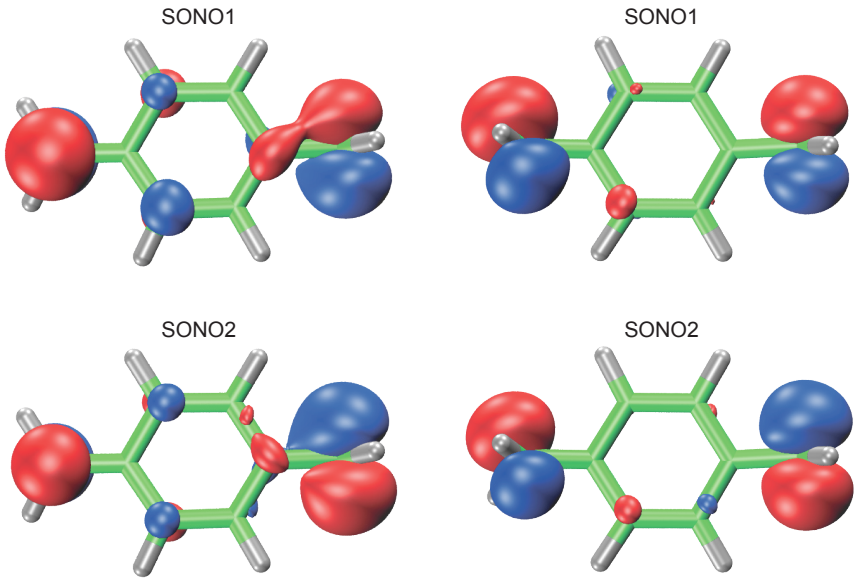

(a) 1.208 ps (b) 3.990 ps

Figure C.3.: SONOs of *p*-xylylene at different time steps with a) one rotated methylene unit and b) two rotated methylene units.

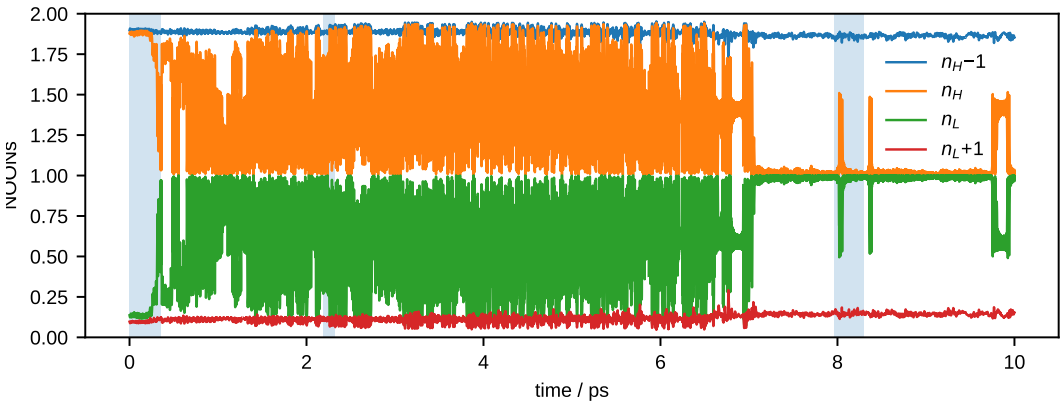

Figure C.4.: NOONs along the ASQPM trajectory of [8]annulene. The regions shown in Fig. 3 of the main article are highlighted with blue background.

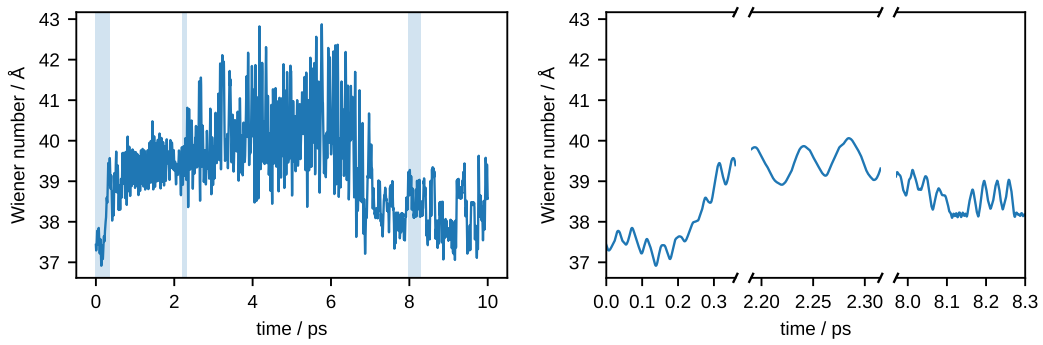

(a) (b)

Figure C.5.: Wiener number along the ASQPM trajectory of [8]annulene. a) Complete time evolution of the 10 ps trajectory. The regions shown in Fig. 3 of the main article are highlighted with blue background. b) Zoomed to the representative regions shown in Fig. 3 of the main article.

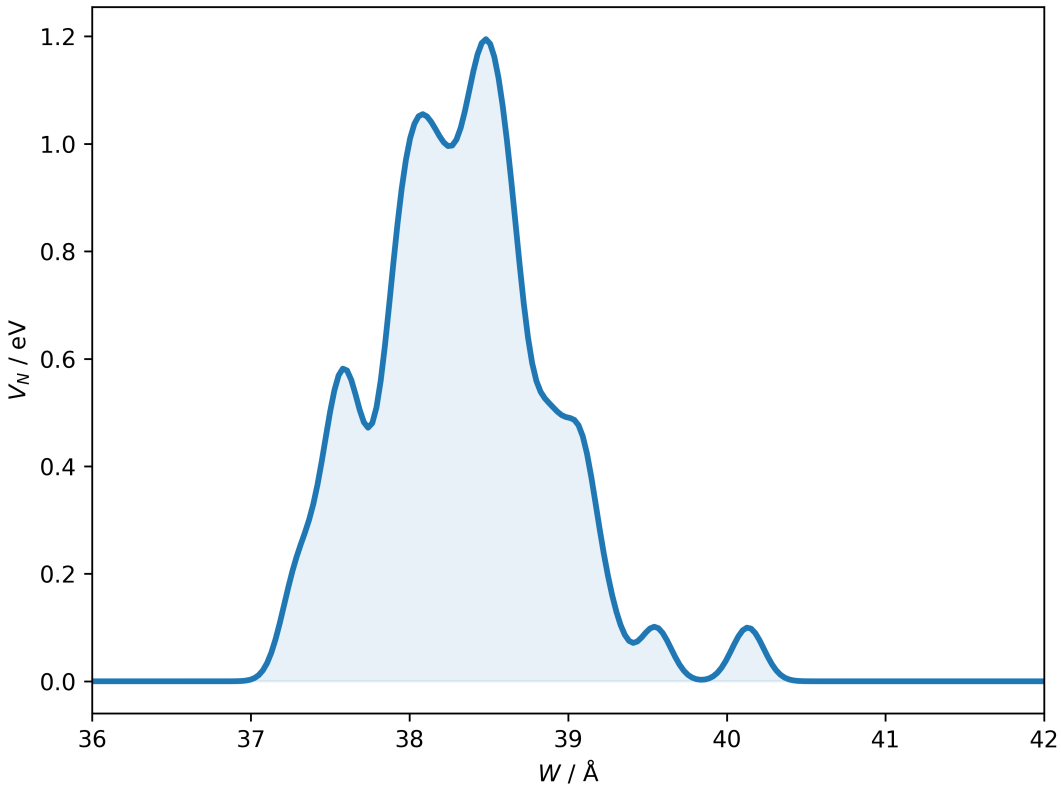

Figure C.6.: Bias potential V_N in dependence of the Wiener number W, obtained from the ASQPM trajectory of [8]annulene after 10 ps, when 59 Gaussians have been added.

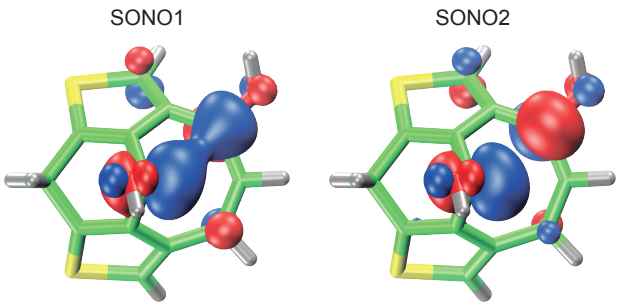

Figure C.7.: Optimized structure and SONOs of the stabilized biradical **B2**.

Table C.1.: Cartesian coordinates of the optimized geometry of [8]annulene in Å on the CASSCF(8, 8)/6-31G level of theory ($E = -307.53180233\,\mathrm{a.u.}$).

C	-1.5830145777	0.2808515314	0.4304507653
C	-1.2921523200	-1.0354077273	0.4043890949
C	-0.2469717743	-1.6998044437	-0.4021610608
C	1.0693053815	-1.4086073491	-0.4237177604
C	1.7610559362	-0.3594075741	0.3538525632
C	1.4701486624	0.9568843864	0.3790355063
C	0.3940685061	1.6444599919	-0.3647949833
C	-0.9222504678	1.3534816475	-0.3421442385
H	-2.4192584592	0.5985718360	1.0310041868
H	-1.9110653678	-1.6981959869	0.9861516444
H	-0.5853137206	-2.5390744312	-0.9868922547
H	1.7114187327	-2.0306067013	-1.0249579002
H	2.6206437139	-0.6944034225	0.9102626244
H	2.1124850714	1.6021790304	0.9548877056
H	0.7091754800	2.5011436933	-0.9371550193
H	-1.5875112669	1.9926022891	-0.8986628435

Table C.2.: Cartesian coordinates of the optimized geometry of **B1** in Å on the CASSCF(8, 8)/6-31G level of theory ($E = -1291.58989906\,\mathrm{a.u.}$).

C	-1.4906566719	0.3543665167	0.7460648330
C	-1.7759335667	-0.7004577140	-0.2249453588
C	-0.6869022731	-1.5210095772	-0.7324828926
C	0.6925999274	-1.3772860520	-0.1988337635
C	1.4047877325	-0.2572350908	0.0693296858
C	1.2182773240	1.1942049259	-0.0530776426
C	0.0300038559	1.9429811645	-0.4967878064
C	-1.3046502013	1.5505121967	-0.0716572361
C	-1.0282257111	-2.1476750885	-1.8938835242
H	2.4011113576	-0.4705204675	0.4180948726
C	-0.0118851705	2.8241123716	-1.5139900914
C	-2.3137747376	1.8919830171	-0.9201030568
C	-3.4655589287	0.8991044472	-1.1184928961
H	-4.1908089058	0.9907867214	-0.3175471307
H	-3.9820016321	1.0732290731	-2.0501588609
C	-2.8062020109	-0.4861988163	-1.0931129797
H	-0.9376173319	0.1786415082	1.6447150876
H	2.1317588720	1.7534536840	0.0310470387
H	1.2216114441	-2.3012578569	-0.0456018864
S	-2.6617091111	-1.6261468899	-2.5048344020
S	-1.6917493399	3.0896606711	-2.1371453970
H	0.8055996290	3.2840623646	-2.0243518321
H	-0.4311345499	-2.7937911090	-2.4988647604

Table C.3.: Cartesian coordinates of the optimized geometry of **B2** in Å on the CASSCF(8, 8)/6-31G level of theory ($E = -1441.22883733\,\mathrm{a.u.}$).

C	-1.4766746189	0.3402677967	0.7625665170
C	-1.7484442231	-0.7467223757	-0.1989843396
C	-0.6495247606	-1.5104751013	-0.7573204184
C	0.7407446498	-1.3638601257	-0.2528862428
C	1.4460524301	-0.2467674314	0.0145610072
C	1.2270746695	1.2012858132	-0.0715947021
C	0.0473141569	1.9424014808	-0.5131407413
C	-1.2686389461	1.5012396091	-0.1154383734
C	-1.0150089983	-2.1353929916	-1.9128964328
H	2.4574120699	-0.4217576674	0.3329647233
C	-0.0203339531	2.8673601963	-1.5214538591
C	-2.2713095319	1.8216883809	-0.9370113014
C	-3.4566586761	0.8552302102	-1.0634969143
H	-4.1476529304	0.9876615054	-0.2401256141
H	-3.9967239592	1.0118228305	-1.9843997843
C	-2.8198692891	-0.5484151785	-1.0247921144
O	-2.3121498065	0.5387479034	1.8469703072
O	2.4400315740	1.8765565845	-0.0787223334
H	1.2795355254	-2.2849225005	-0.1218412745
S	-2.6857927785	-1.6615267062	-2.4574403787
S	-1.7237591255	3.0767153558	-2.1210732155
H	0.7768566026	3.3471603570	-2.0438540914
H	-0.4296766157	-2.7754797910	-2.5351693257
H	-2.5098668971	-0.2569012871	2.3294581439
H	2.3728234320	2.7983431327	0.1435507586

Bibliography

[1] Schrödinger, E. *Ann. Phys.* **1926**, *384*, 361–376.

[2] Born, M.; Heisenberg, W. *Ann. Phys.* **1924**, *379*, 1–31.

[3] Hund, F. *Z. Phys.* **1927**, *40*, 742–764.

[4] Born, M.; Oppenheimer, R. *Ann. Phys.* **1927**, *389*, 457–484.

[5] Hartree, D. R. *Math. Proc. Cambridge Philos. Soc.* **1928**, *24*, 111–132.

[6] Fock, V. *Z. Phys.* **1930**, *61*, 126–148.

[7] Shavitt, I. *Mol. Phys.* **1998**, *94*, 3–17.

[8] Møller, C.; Plesset, M. S. *Phys. Rev.* **1934**, *46*, 618–622.

[9] Čížek, J. *J. Chem. Phys.* **1966**, *45*, 4256–4266.

[10] Hohenberg, P.; Kohn, W. *Phys. Rev.* **1964**, *136*, B864–B871.

[11] Kohn, W.; Sham, L. J. *Phys. Rev.* **1965**, *140*, A1133–A1138.

[12] Frenkel, D.; Smit, B. *Understanding Molecular Simulation*; Elsevier LTD, Oxford, 2001.

[13] Eyring, H.; Polanyi, M. *Z. Phys. Chem. Abt. B* **1931**, *12*, 279–311.

[14] McCammon, J. A.; Gelin, B. R.; Karplus, M. *Nature* **1977**, *267*, 585–590.

[15] Verlet, L. *Phys. Rev.* **1967**, *159*, 98–103.

[16] Warshel, A.; Karplus, M. *J. Am. Chem. Soc.* **1972**, *94*, 5612–5625.

[17] Warshel, A.; Levitt, M. *J. Mol. Biol.* **1976**, *103*, 227–249.

[18] Maseras, F.; Morokuma, K. *J. Comput. Chem.* **1995**, *16*, 1170–1179.

[19] Car, R.; Parrinello, M. *Phys. Rev. Lett.* **1985**, *55*, 2471–2474.

[20] Tully, J. C. *J. Chem. Phys.* **1990**, *93*, 1061–1071.

[21] Tully, J. C. *Theor. Chem. Acc.* **2000**, *103*, 173–176.

[22] Swope, W. C.; Andersen, H. C.; Berens, P. H.; Wilson, K. R. *J. Chem. Phys.* **1982**, *76*, 637–649.

[23] Berendsen, H. J. C.; Postma, J. P. M.; van Gunsteren, W. F.; DiNola, A.; Haak, J. R. *J. Chem. Phys.* **1984**, *81*, 3684–3690.

[24] Bussi, G.; Donadio, D.; Parrinello, M. *J. Chem. Phys.* **2007**, *126*, 014101.

[25] Wehner, M.; Röhr, M. I. S.; Bühler, M.; Stepanenko, V.; Wagner, W.; Würthner, F. *J. Am. Chem. Soc.* **2019**, *141*, 6092–6107.

[26] Darve, E.; Pohorille, A. *J. Chem. Phys.* **2001**, *115*, 9169–9183.

[27] Hansmann, U. H. E.; Wille, L. T. *Phys. Rev. Lett.* **2002**, *88*, 068105.

[28] Huber, T.; Torda, A. E.; van Gunsteren, W. F. *J. Comput.-Aided Mol. Des.* **1994**, *8*, 695–708.

[29] Maragakis, P.; van der Vaart, A.; Karplus, M. *J. Phys. Chem. B* **2009**, *113*, 4664–4673.

[30] Wang, F.; Landau, D. P. *Phys. Rev. Lett.* **2001**, *86*, 2050–2053.

[31] Torrie, G. M.; Valleau, J. P. *J. Comput. Phys.* **1977**, *23*, 187–199.

[32] Laio, A.; Parrinello, M. *Proc. Nat. Acad. Sci. U. S. A.* **2002**, *99*, 12562–12566.

[33] Barducci, A.; Bussi, G.; Parrinello, M. *Phys. Rev. Lett.* **2008**, *100*, 020603.

[34] Dama, J. F.; Rotskoff, G.; Parrinello, M.; Voth, G. A. *J. Chem. Theory Comput.* **2014**, *10*, 3626–3633.

[35] Branduardi, D.; Bussi, G.; Parrinello, M. *J. Chem. Theory Comput.* **2012**, *8*, 2247–2254.

[36] Valsson, O.; Tiwary, P.; Parrinello, M. *Annu. Rev. Phys. Chem.* **2016**, *67*, 159–184.

[37] Franck, J.; Dymond, E. G. *Trans. Faraday Soc.* **1926**, *21*, 536–542.

[38] Condon, E. *Phys. Rev.* **1926**, *28*, 1182–1201.

[39] Condon, E. U. *Phys. Rev.* **1928**, *32*, 858–872.

[40] Kasha, M. *Discuss. Faraday Soc.* **1950**, *9*, 14–19.

[41] Ehrenfest, P. *Z. Phys.* **1927**, *45*, 455–457.

[42] Tully, J. C. In *Classical and Quantum Dynamics in Condensed Phase Simulations*; Berne, B. J., Ciccotti, G., Coker, D. F., Eds.; World Scientific: Singapore, 1998; pp 489–514.

[43] Mitrić, R.; Petersen, J.; Bonačić-Koutecký, V. In *Conical Intersections - Theory, Computation and Experiment*; Domcke, W., Yarkony, D. R., Köppel, H., Eds.; Advanced Series in Physical Chemistry; World Scientific: Singapore, 2011; pp 497–568.

[44] Lisinetskaya, P. G.; Mitrić, R. *Phys. Rev. A* **2011**, *83*, 033408.

[45] Mitrić, R.; Petersen, J.; Bonačić-Koutecký, V. *Phys. Rev. A* **2009**, *79*, 053416.

[46] Petersen, J.; Wohlgemuth, M.; Sellner, B.; Bonačić-Koutecký, V.; Lischka, H.; Mitrić, R. *Phys. Chem. Chem. Phys.* **2012**, *14*, 4687–4694.

[47] Röhr, M. I. S.; Petersen, J.; Wohlgemuth, M.; Bonačić-Koutecký, V.; Mitrić, R. *ChemPhysChem* **2013**, *14*, 1377–1386.

[48] Wohlgemuth, M.; Mitrić, R. *J. Phys. Chem. A* **2016**, *120*, 8976–8982.

[49] Yarkony, D. R. *Rev. Mod. Phys.* **1996**, *68*, 985–1013.

[50] Domcke, W., Yarkony, D. R., Köppel, H., Eds. *Conical Intersections: Electronic Structure, Dynamics and Spectroscopy*; Advanced Series in Physical Chemistry; World Scientific: Singapore, 2004.

[51] Domcke, W., Yarkony, D. R., Köppel, H., Eds. *Conical Intersections: Theory, Computation and Experiment*; Advanced Series in Physical Chemistry; World Scientific: Singapore, 2011.

[52] von Neumann, J.; Wigner, E. P. *Phys. Z.* **1929**, *30*, 467–470.

[53] Michl, J. *Top. Curr. Chem.* **1974**, *46*, 1–59.

[54] Bonačić-Koutecký, V.; Koutecký, J.; Michl, J. *Angew. Chem. Int. Ed.* **1987**, *26*, 170–189.

[55] Bernardi, F.; Olivucci, M.; Robb, M. A. *Acc. Chem. Res.* **1990**, *23*, 405–412.

[56] Yarkony, D. R. *J. Chem. Phys.* **1990**, *92*, 2457–2463.

[57] Atchity, G. J.; Xantheas, S. S.; Ruedenberg, K. *J. Chem. Phys.* **1991**, *95*, 1862–1876.

[58] Bernardi, F.; De, S.; Olivucci, M.; Robb, M. A. *J. Am. Chem. Soc.* **1990**, *112*, 1737–1744.

[59] Palmer, I. J.; Ragazos, I. N.; Bernardi, F.; Olivucci, M.; Robb, M. A. *J. Am. Chem. Soc.* **1993**, *115*, 673–682.

[60] Jahn, H. A.; Teller, E. *Proc. R. Soc. London, Ser. A* **1937**, *161*, 220–235.

[61] Yarkony, D. R. In *Conical Intersections: Electronic Structure, Dynamics and Spectroscopy*; Domcke, W., Yarkony, D. R., Köppel, H., Eds.; Advanced Series in Physical Chemistry; World Scientific: Singapore, 2004; pp 41–127.

[62] Longuet-Higgins, H. C.; Öpik, U.; Pryce, M. H. L.; Sack, R. A. *Proc. R. Soc. London, Ser. A* **1958**, *244*, 1–16.

[63] Mead, C. A.; Truhlar, D. G. *J. Chem. Phys.* **1979**, *70*, 2284–2296.

[64] Berry, M. V. *Proc. R. Soc. London, Ser. A* **1984**, *392*, 45–57.

[65] Schuurman, M. S.; Stolow, A. *Annu. Rev. Phys. Chem.* **2018**, *69*, 427–450.

[66] Barbatti, M.; Aquino, A. J. A.; Szymczak, J. J.; Nachtigallová, D.; Hobza, P.; Lischka, H. *Proc. Natl. Acad. Sci. U. S. A.* **2010**, *107*, 21453–21458.

[67] Blancafort, L.; Cohen, B.; Hare, P. M.; Kohler, B.; Robb, M. A. *J. Phys. Chem. A* **2005**, *109*, 4431–4436.

[68] Yoshizawa, T.; Wald, G. *Nature* **1963**, *197*, 1279–1286.

[69] Garavelli, M.; Celani, P.; Bernardi, F.; Robb, M. A.; Olivucci, M. *J. Am. Chem. Soc.* **1997**, *119*, 6891–6901.

[70] Garavelli, M.; Vreven, T.; Celani, P.; Bernardi, F.; Robb, M. A.; Olivucci, M. *J. Am. Chem. Soc.* **1998**, *120*, 1285–1288.

[71] González-Luque, R.; Garavelli, M.; Bernardi, F.; Merchán, M.; Robb, M. A.; Olivucci, M. *Proc. Natl. Acad. Sci. U. S. A.* **2000**, *97*, 9379–9384.

[72] Polli, D.; Altoè, P.; Weingart, O.; Spillane, K. M.; Manzoni, C.; Brida, D.; Tomasello, G.; Orlandi, G.; Kukura, P.; Mathies, R. A.; Garavelli, M.; Cerullo, G. *Nature* **2010**, *467*, 440–443.

[73] Musser, A. J.; Liebel, M.; Schnedermann, C.; Wende, T.; Kehoe, T. B.; Rao, A.; Kukura, P. *Nat. Phys.* **2015**, *11*, 352–357.

[74] Lim, J. M.; Kim, P.; Yoon, M.-C.; Sung, J.; Dehm, V.; Chen, Z.; Würthner, F.; Kim, D. *Chem. Sci.* **2013**, *4*, 388–397.

[75] Hoche, J.; Schmitt, H.-C.; Humeniuk, A.; Fischer, I.; Mitrić, R.; Röhr, M. I. S. *Phys. Chem. Chem. Phys.* **2017**, *19*, 25002–25015.

[76] Sorgues, S.; Mestdagh, J. M.; Visticot, J. P.; Soep, B. *Phys. Rev. Lett.* **2003**, *91*, 103001.

[77] Kowalewski, M.; Bennett, K.; Dorfman, K. E.; Mukamel, S. *Phys. Rev. Lett.* **2015**, *115*, 193003.

[78] Adachi, S.; Schatteburg, T.; Humeniuk, A.; Mitrić, R.; Suzuki, T. *Phys. Chem. Chem. Phys.* **2019**, *21*, 13902–13905.

[79] Manaa, M. R.; Yarkony, D. R. *J. Chem. Phys.* **1993**, *99*, 5251–5256.

[80] Bearpark, M. J.; Robb, M. A.; Schlegel, H. B. *Chem. Phys. Lett.* **1994**, *223*, 269–274.

[81] Keal, T. W.; Koslowski, A.; Thiel, W. *Theor. Chem. Acc.* **2007**, *118*, 837–844.

[82] Ciminelli, C.; Granucci, G.; Persico, M. *Chem. Eur. J.* **2004**, *10*, 2327–2341.

[83] Maeda, S.; Ohno, K.; Morokuma, K. *J. Phys. Chem. A* **2009**, *113*, 1704–1710.

[84] Harabuchi, Y.; Maeda, S.; Taketsugu, T.; Minezawa, N.; Morokuma, K. *J. Chem. Theory Comput.* **2013**, *9*, 4116–4123.

[85] Maeda, S.; Taketsugu, T.; Morokuma, K. *Z. Phys. Chem.* **2013**, *227*, 1421–1433.

[86] Maeda, S.; Harabuchi, Y.; Taketsugu, T.; Morokuma, K. *J. Phys. Chem. A* **2014**, *118*, 12050–12058.

[87] Harabuchi, Y.; Taketsugu, T.; Maeda, S. *Chem. Phys. Lett.* **2017**, *674*, 141–145.

[88] Abe, M. *Chem. Rev.* **2013**, *113*, 7011–7088.

[89] Flynn, C. R.; Michl, J. *J. Am. Chem. Soc.* **1974**, *96*, 3280–3288.

[90] Xu, C.; Braun-Unkhoff, M.; Naumann, C.; Frank, P. *Proc. Combust. Inst.* **2007**, *31*, 231–239.

[91] Johnson, M. S.; Feilberg, K. L.; von Hessberg, P.; Nielsen, O. J. *Chem. Soc. Rev.* **2002**, *31*, 313–323.

[92] Liu, Y.; Li, C.; Ren, Z.; Yan, S.; Bryce, M. R. *Nat. Rev. Mater.* **2018**, *3*, 18020.

[93] Ai, X.; Evans, E. W.; Dong, S.; Gillett, A. J.; Guo, H.; Chen, Y.; Hele, T. J. H.; Friend, R. H.; Li, F. *Nature* **2018**, *563*, 536–540.

[94] Rausch, R.; Schmidt, D.; Bialas, D.; Krummenacher, I.; Braunschweig, H.; Würthner, F. *Chem. Eur. J.* **2018**, *24*, 3420–3424.

[95] Kamada, K.; Ohta, K.; Shimizu, A.; Kubo, T.; Kishi, R.; Takahashi, H.; Botek, E.; Champagne, B.; Nakano, M. *J. Phys. Chem. Lett.* **2010**, *1*, 937–940.

[96] Döhnert, D.; Koutecký, J. *J. Am. Chem. Soc.* **1980**, *102*, 1789–1796.

[97] Nakano, M. *Top. Curr. Chem.* **2017**, *375*, 1–67.

[98] Shao, Y.; Head-Gordon, M.; Krylov, A. I. *J. Chem. Phys.* **2003**, *118*, 4807–4818.

[99] Petersen, J.; Lindner, J. O.; Mitrić, R. *J. Phys. Chem. B* **2018**, *122*, 19–27.

[100] Lindner, J. O.; Röhr, M. I. S.; Mitrić, R. *Phys. Rev. A* **2018**, *97*, 052502.

[101] Lindner, J. O.; Sultangaleeva, K.; Röhr, M. I. S.; Mitrić, R. *J. Chem. Theory Comput.* **2019**, *15*, 3450–3460.

[102] Cremer, D.; Pople, J. A. *J. Am. Chem. Soc.* **1975**, *97*, 1354–1358.

[103] Lindner, J. O.; Röhr, M. I. S. *Phys. Chem. Chem. Phys.* **2019**, Accepted Manuscript, DOI: 10.1039/C9CP05182A.

[104] Imberty, A.; Perez, S. *Chem. Rev.* **2000**, *100*, 4567–4588.

[105] Simons, J. P.; Jockusch, R. A.; ÇarÇabal, P.; Hünig, I.; Kroemer, R. T.; Macleod, N. A.; Snoek, L. C. *Int. Rev. Phys. Chem.* **2005**, *24*, 489–531.

[106] da Silva, C. O. *Theor. Chem. Acc.* **2006**, *116*, 137–147.

[107] Meinert, C.; Myrgorodska, I.; de Marcellus, P.; Buhse, T.; Nahon, L.; Hoffmann, S. V.; d'Hendecourt, L. L. S.; Meierhenrich, U. J. *Science* **2016**, *352*, 208–212.

[108] Laurent, T. C.; Wertheim, E. M.; Åkerström, Å.; Finsnes, E.; Sörensen, J. S.; Sörensen, N. A. *Acta Chem. Scand.* **1952**, *6*, 678–681.

[109] Laurent, T. C. *J. Am. Chem. Soc.* **1956**, *78*, 1875–1877.

[110] Phillips, G. O.; Rickards, T. *J. Chem. Soc. B* **1969**, 455–461.

[111] Sobolewski, A. L.; Domcke, W. *J. Phys. Chem. A* **1999**, *103*, 4494–4504.

[112] Sobolewski, A. L.; Domcke, W. *Chem. Phys.* **2000**, *259*, 181–191.

[113] Sobolewski, A. L.; Domcke, W.; Dedonder-Lardeux, C.; Jouvet, C. *Phys. Chem. Chem. Phys.* **2002**, *4*, 1093–1100.

[114] Lucena, J. R.; Ventura, E.; do Monte, S. A.; Araújo, R. C. M. U.; Ramos, M. N.; Fausto, R. *J. Chem. Phys.* **2007**, *127*, 164320.

[115] Ashfold, M. N. R.; King, G. A.; Murdock, D.; Nix, M. G. D.; Oliver, T. A. A.; Sage, A. G. *Phys. Chem. Chem. Phys.* **2010**, *12*, 1218–1238.

[116] Murdock, D.; Harris, S. J.; Luke, J.; Grubb, M. P.; Orr-Ewing, A. J.; Ashfold, M. N. R. *Phys. Chem. Chem. Phys.* **2014**, *16*, 21271–21279.

[117] Tuna, D.; Sobolewski, A. L.; Domcke, W. *Phys. Chem. Chem. Phys.* **2014**, *16*, 38–47.

[118] Tuna, D.; Sobolewski, A. L.; Domcke, W. *J. Phys. Chem. B* **2016**, *120*, 10729–10735.

[119] Roig, B.; Thomas, O. *Anal. Chim. Acta* **2003**, *477*, 325–329.

[120] Sarazin, C.; Delaunay, N.; Costanza, C.; Eudes, V.; Mallet, J.-M.; Gareil, P. *Anal. Chem.* **2011**, *83*, 7381–7387.

[121] Schmid, T.; Himmelsbach, M.; Oliver, J. D.; Gaborieau, M.; Castignolles, P.; Buchberger, W. *J. Chromatogr. A* **2015**, *1388*, 259–266.

[122] Schmid, T.; Himmelsbach, M.; Buchberger, W. W. *Electrophoresis* **2016**, *37*, 947–953.

[123] *TURBOMOLE, version V6.3*; Turbomole GmbH, Karlsruhe, Germany, 2011.

[124] Becke, A. D. *J. Chem. Phys.* **1993**, *98*, 5648–5652.

[125] Hehre, W. J.; Ditchfield, R.; Pople, J. A. *J. Chem. Phys.* **1972**, *56*, 2257–2261.

[126] Clark, T.; Chandrasekhar, J.; Spitznagel, G. W.; von Ragué Schleyer, P. *J. Comput. Chem.* **1983**, *4*, 294–301.

[127] Hariharan, P. C.; Pople, J. A. *Theor. Chim. Acta* **1973**, *28*, 213–222.

[128] Dunning, T. H. *J. Chem. Phys.* **1989**, *90*, 1007–1023.

[129] Kendall, R. A.; Dunning, T. H.; Harrison, R. J. *J. Chem. Phys.* **1992**, *96*, 6796–6806.

[130] Bauernschmitt, R.; Ahlrichs, R. *Chem. Phys. Lett.* **1996**, *256*, 454–464.

[131] Mitrić, R.; Werner, U.; Bonačić-Koutecký, V. *J. Chem. Phys.* **2008**, *129*, 164118.

[132] Levine, B. G.; Ko, C.; Quenneville, J.; Martínez, T. J. *Mol. Phys.* **2006**, *104*, 1039–1051.

[133] Schirmer, J. *Phys. Rev. A* **1982**, *26*, 2395–2416.

[134] Plasser, F.; Crespo-Otero, R.; Pederzoli, M.; Pittner, J.; Lischka, H.; Barbatti, M. *J. Chem. Theor. Comput.* **2014**, *10*, 1395–1405.

[135] Dutta, A.; Sherill, C. D. *J. Chem. Phys.* **2003**, *118*, 1610–1619.

[136] Schultz, T.; Samoylova, E.; Radloff, W.; Hertel, I. V.; Sobolewski, A. L.; Domcke, W. *Science* **2004**, *306*, 1765–1768.

[137] Bernardi, F.; Olivucci, M.; Robb, M. A. *Chem. Soc. Rev.* **1996**, *25*, 321–328.

[138] Mitrić, R.; Bonačić-Koutecký, V.; Pittner, J.; Lischka, H. *J. Chem. Phys.* **2006**, *125*, 024303.

[139] Liebel, M.; Schnedermann, C.; Kukura, P. *Phys. Rev. Lett.* **2014**, *112*, 198302.

[140] Kowalewski, M.; Bennett, K.; Rouxel, J. R.; Mukamel, S. *Phys. Rev. Lett.* **2016**, *117*, 043201.

[141] Levine, B. G.; Coe, J. D.; Martínez, T. J. *J. Phys. Chem. B* **2008**, *112*, 405–413.

[142] Maeda, S.; Saito, R.; Morokuma, K. *J. Phys. Chem. Lett.* **2011**, *2*, 852–857.

[143] Maeda, S.; Taketsugu, T.; Ohno, K.; Morokuma, K. *J. Am. Chem. Soc.* **2015**, *137*, 3433–3445.

[144] Mori, T.; Martínez, T. J. *J. Chem. Theory Comput.* **2013**, *9*, 1155–1163.

[145] Duan, H.-G.; Miller, R. J. D.; Thorwart, M. *J. Phys. Chem. Lett.* **2016**, *7*, 3491–3496.

[146] Raiteri, P.; Laio, A.; Gervasio, F. L.; Micheletti, C.; Parrinello, M. *J. Phys. Chem. B* **2006**, *110*, 3533–3539.

[147] Bonomi, M.; Parrinello, M. *Phys. Rev. Lett.* **2010**, *104*, 190601.

[148] Tribello, G. A.; Ceriotti, M.; Parrinello, M. *Proc. Nat. Acad. Sci. U. S. A.* **2010**, *107*, 17509–17514.

[149] Ceriotti, M.; Tribello, G. A.; Parrinello, M. *Proc. Nat. Acad. Sci. U. S. A.* **2011**, *108*, 13023–13028.

[150] Mihalić, Z.; Nikolić, S.; Trinajstić, N. *J. Chem. Inf. Model.* **1992**, *32*, 28–37.

[151] Bogdanov, B.; Nikolić, S.; Trinajstić, N. *J. Math. Chem.* **1989**, *3*, 299–309.

[152] Stenrup, M.; Larson, Å. *Chem. Phys.* **2011**, *379*, 6–12.

[153] Gavrilov, N.; Salzmann, S.; Marian, C. M. *Chem. Phys.* **2008**, *349*, 269–277.

[154] Fuji, T.; Suzuki, Y.-I.; Horio, T.; Suzuki, T.; Mitrić, R.; Werner, U.; Bonačić-Koutecký, V. *J. Chem. Phys.* **2010**, *133*, 234303.

[155] Spesyvtsev, R.; Horio, T.; Suzuki, Y.-I.; Suzuki, T. *J. Chem. Phys.* **2015**, *143*, 014302.

[156] Oesterling, S.; Schalk, O.; Geng, T.; Thomas, R. D.; Hansson, T.; de Vivie-Riedle, R. *Phys. Chem. Chem. Phys.* **2017**, *19*, 2025–2035.

[157] Werner, H.-J.; Knowles, P. J.; Knizia, G.; Manby, F. R.; Schütz, M. *WIREs Comput. Mol. Sci.* **2011**, *2*, 242–253.

[158] Robb, M. A. *Theoretical Chemistry for Electronic Excited States*; Theoretical and Computational Chemistry Series; Royal Society of Chemistry: Cambridge, 2018.

[159] Li, Q.; Mendive-Tapia, D.; Paterson, M. J.; Migani, A.; Bearpark, M. J.; Robb, M. A.; Blancafort, L. *Chem. Phys.* **2010**, *377*, 60–65.

[160] Sicilia, F.; Bearpark, M. J.; Blancafort, L.; Robb, M. A. *Theor. Chem. Acc.* **2007**, *118*, 241–251.

[161] Sicilia, F.; Blancafort, L.; Bearpark, M. J.; Robb, M. A. *J. Chem. Theory Comput.* **2008**, *4*, 257–266.

[162] Olivucci, M.; Ragazos, I. N.; Bernardi, F.; Robb, M. A. *J. Am. Chem. Soc.* **1993**, *115*, 3710–3721.

[163] Bernardi, F.; Olivucci, M.; Robb, M. A. *J. Photoch. Photobio. A* **1997**, *105*, 365–371.

[164] Krawczyk, R. P.; Malsch, K.; Hohlneicher, G.; Gillen, R. C.; Domcke, W. *Chem. Phys. Lett.* **2000**, *320*, 535–541.

[165] Lasorne, B.; Bearpark, M. J.; Robb, M. A.; Worth, G. A. *J. Phys. Chem. A* **2008**, *112*, 13017–13027.

[166] Parker, D.; Minns, R.; Penfold, T.; Worth, G.; Fielding, H. *Chem. Phys. Lett.* **2009**, *469*, 43–47.

[167] Ditchfield, R.; Hehre, W. J.; Pople, J. A. *J. Chem. Phys.* **1971**, *54*, 724–728.

[168] Koslowski, A.; Beck, M. E.; Thiel, W. *J. Comput. Chem.* **2003**, *24*, 714–726.

[169] Patchkovskii, S.; Koslowski, A.; Thiel, W. *Theor. Chem. Acc.* **2005**, *114*, 84–89.

[170] Bussi, G.; Branduardi, D. *Rev. Comput. Chem.* **2015**, *28*, 1–49.

[171] Barbatti, M.; Lischka, H. *J. Am. Chem. Soc.* **2008**, *130*, 6831–6839.

[172] Perun, S.; Sobolewski, A. L.; Domcke, W. *J. Am. Chem. Soc.* **2005**, *127*, 6257–6265.

[173] Oviedo, M. B.; Sánchez, C. G. *J. Phys. Chem. A* **2011**, *115*, 12280–12285.

[174] Galván, M.; Gázquez, J. L.; Vela, A. *J. Chem. Phys.* **1986**, *85*, 2337–2338.

[175] Remenyi, C.; Kaupp, M. *J. Am. Chem. Soc.* **2005**, *127*, 11399–11413.

[176] Yang, N.; Li, L.; Li, J.; Ding, W.; Wei, Z. *Chem. Sci.* **2018**, *9*, 5795–5804.

[177] Alcaide, B.; Almendros, P.; Aragoncillo, C. *Chem. Soc. Rev.* **2010**, *39*, 783–816.

[178] Minami, T.; Nakano, M. *J. Phys. Chem. Lett.* **2011**, *3*, 145–150.

[179] Smith, M. B.; Michl, J. *Chem. Rev.* **2010**, *110*, 6891–6936.

[180] Zeng, Z.; Shi, X.; Chi, C.; Navarrete, J. T. L.; Casado, J.; Wu, J. *Chem. Soc. Rev.* **2015**, *44*, 6578–6596.

[181] DeFrancisco, J. R.; López-Espejo, G.; Zafra, J. L.; Yadav, S.; Messersmith, R. E.; Gómez-García, C. J.; Ottosson, H.; Casado, J.; Tovar, J. D. *J. Phys. Chem. C* **2018**, *122*, 12148–12157.

[182] Böhnke, J. et al. *Nat. Commun.* **2018**, *9*, 1197.

[183] Piana, S.; Laio, A. *J. Phys. Chem. B* **2007**, *111*, 4553–4559.

[184] Grimme, S. *J. Chem. Theory Comput.* **2019**, *15*, 2847–2862.

[185] Hodel, F. H.; Deglmann, P.; Luber, S. *J. Chem. Theory Comput.* **2017**, *13*, 3348–3358.

[186] Schaefgen, J. R. *J. Polym. Sci.* **1955**, *15*, 203–219.

[187] Coulson, C. A.; Craig, D. P.; Maccoll, A.; Pullman, A. *Discuss. Faraday Soc.* **1947**, *2*, 36–38.

[188] Williams, D. J.; Pearson, J. M.; Levy, M. *J. Am. Chem. Soc.* **1970**, *92*, 1436–1438.

[189] Gellini, C.; Salvi, P. R. *Symmetry* **2010**, *2*, 1846–1924.

[190] Kummli, D. S.; Lobsiger, S.; Frey, H. M.; Leutwyler, S.; Stanton, J. F. *J. Phys. Chem. A* **2008**, *112*, 9134–9143.

[191] Paquette, L. A. *Acc. Chem. Res.* **1993**, *26*, 57–62.

[192] Hrovat, D. A.; Borden, W. T. *J. Am. Chem. Soc.* **1992**, *114*, 5879–5881.

[193] Andres, J. L.; Castano, O.; Morreale, A.; Palmeiro, R.; Gomperts, R. *J. Chem. Phys.* **1998**, *108*, 203–207.

[194] Gordon, M. S.; Binkley, J. S.; Pople, J. A.; Pietro, W. J.; Hehre, W. J. *J. Am. Chem. Soc.* **1982**, *104*, 2797–2803.

[195] Francl, M. M.; Pietro, W. J.; Hehre, W. J.; Binkley, J. S.; Gordon, M. S.; DeFrees, D. J.; Pople, J. A. *J. Chem. Phys.* **1982**, *77*, 3654–3665.

[196] Humeniuk, A.; Mitrić, R. *Comput. Phys. Commun.* **2017**, *221*, 174–202.

[197] Cox, N.; Pantazis, D. A.; Neese, F.; Lubitz, W. *Interface Focus* **2015**, *5*, 20150009.

[198] Meyer, T. J.; Sheridan, M. V.; Sherman, B. D. *Chem. Soc. Rev.* **2017**, *46*, 6148–6169.

Individual Contributions

All co-authors of the manuscripts included in this cumulative thesis are informed about and agree with the reprint and the respective individual contributions as stated below.

Ultrafast Photodynamics of Glucose

J. Petersen, J. O. Lindner, R. Mitrić, *J. Phys. Chem. B* **2018**, *122*, 19–27.

author	J.P.	J.O.L.	R.M.
design of the research	50%		50%
theoretical simulations		100%	
publication writing	40%	60%	
publication correction			100%
publication coordination	50%		50%

Multistate Metadynamics for Automatic Exploration of Conical Intersections

J. O. Lindner, M. I. S. Röhr, R. Mitrić, *Phys. Rev. A* **2018**, *97*, 052502.

author	J.O.L.	M.I.S.R.	R.M.
design of the research		40%	60%
method implementation	100%		
example calculation furan	100%		
publication writing	80%		20%
publication correction		50%	50%
publication coordination		50%	50%

metaFALCON: A Program Package for Automatic Sampling of Conical Intersection Seams Using Multistate Metadynamics

J. O. Lindner, K. Sultangaleeva, M. I. S. Röhr, R. Mitrić, *J. Chem. Theor. Comput.* **2019**, *15*, 3450–3460.

author	J.O.L.	K.S.	M.I.S.R.	R.M.
design of the research			50%	50%
method implementation	80%	20%		
example calculations 1,3-butadiene and benzene	100%			
example calculation 9H-adenine	20%	80%		
metaFALCON software development	100%			
publication writing	80%		10%	10%
publication correction			50%	50%
publication coordination			50%	50%

Metadynamics for Automatic Sampling of Quantum Property Manifolds for Exploration of Molecular Biradicalicity Landscapes

J. O. Lindner, M. I. S. Röhr, *Phys. Chem. Chem. Phys.* **2019**, Accepted Manuscript, DOI: 10.1039/C9CP05182A.

author	J.O.L.	M.I.S.R.
design of the research		100%
method implementation	100%	
example calulations p-xylylene and [8]annulene	100%	
publication writing	80%	20%
publication correction		100%
publication coordination		100%

Acknowledgement

I would like to thank

- Prof. Dr. Roland Mitrić for giving me the opportunity to join his group, but also for his excellent supervision, many fruitful discussions and the possibility to visit several (inter-)national conferences and workshops;
- Dr. Merle Röhr for scientific supervision, encouraging support and successful teamwork;
- Prof. Dr. Ingo Fischer for being part of my mentoring committee and for his dedication to the GRK2112;
- Dr. Jens Petersen and Dr. Merle Röhr for attentive proof-reading;
- the whole Mitrić group, especially the co-authors of the presented papers, as well as Joscha Hoche and Matthias Wohlgemuth for their social and technical commitment;
- the Deutsche Forschungsgemeinschaft for funding;
- my family and friends for their support.